THE UNIVERSITY OF QUEENSLAND

AUSTRALIA

Nickel cobaltite-based anode materials for sodium-ion capacitors

Dongfang Yang

Master of Engineering

A thesis submitted for the degree of Doctor of Philosophy at

The University of Queensland in 2018

School of Chemical Engineering

Abstract

While lithium-ion energy storage has found wide applications, the use of lithium ions as charge carrier has a number of issues, such as safety concerns and resource scarcity. In comparison with lithium, sodium is naturally abundant and cheaper. Therefore, recent years have seen a great deal of research interest in using sodium ions as charge carrier to develop sodium-ion energy storage technologies, such as sodium-ion batteries (NIBs) and sodium-ion capacitors (NICs). NICs have emerged as a promising technology for large-scale energy storage applications because this energy storage system combines the advantages of batteries and electrochemical capacitors (ECs). A NIC cell is configured with a battery electrode as the anode, an EC electrode as the cathode and an electrolyte containing sodium ions.

However, finding a high-performance anode material has been one of the great challenges in developing this sustainable electrochemical energy storage technology. Transition-metal oxides (TMOs), such as TiO_2, Nb_2O_5, $NiCo_2O_4$, and Fe_3O_4, have been demonstrated to be promising anode materials for sodium-ion storage. Nickel cobaltite ($NiCo_2O_4$) is of particular importance because of its low cost, abundance in nature, and high theoretical specific capacity (890 mAh g^{-1}). However, this material suffers from critical problems, including sluggish sodium ion diffusion kinetics, low electrical conductivity, and large volume changes during charge/discharge, resulting in poor rate capability and cycling stability in NICs.

This PhD thesis project aims to improve the electrochemical properties of $NiCo_2O_4$ (NCO) with regard to a number of physical and electrochemical aspects, including morphology, structure, electrical conductivity, ion diffusivity, and cycling stability. The main innovations and key findings in this thesis work include:

- Spherical NCO particles have been synthesized by using a solvothermal method. It was found that subsequent thermal treatment temperature played an important role in determining the crystalline structure and particle size of the NCO. The NCO sample thermally treated at 350 ^{o}C showed an optimal and promise performance in NICs. Hollow NCO spheres with a chestnut shell morphology have also been synthesized using the solvothermal method.

- Mechanism study revealed that the NCO phase was converted to metallic nickel, cobalt and sodium oxide phases upon pre-sodiation. The pre-sodiation of NCO was found to significantly improve its energy density. A NIC assembled with the pre-sodiated NCO as the anode and an activated carbon (AC) as the cathode exhibited an energy density of 60 Wh kg^{-1} at a power density of 10,000 W kg^{-1}, much better performance than that reported in the literature.

- The physical and electrochemical properties of the NCO particles were improved by using nitrogen-doped reduced graphene oxide (N-rGO). A porous N-rGO framework was used to encapsulate NCO particles to form a NCO@N-rGO composite. In addition to enhance electronic conductivity and alleviated the volume changes of NCO during charge/discharge, the N-rGO network also contributed to charge storage via a capacitive mechanism. A NIC assembled with NCO@N-rGO as the anode and an AC as the cathode delivered an energy density of 48.8 Wh kg^{-1} at a power density of 9750 W kg^{-1} with a stable cycle life.

- A three-dimensional (3D) nitrogen-doped holey graphene (N-HG) was prepared and used to stabilize NCO particles, forming a NCO@N-HG composite. This composite exhibited good rate capabilities with a capacity of 403 mAh g^{-1} at a current density of 1 A g^{-1}, which was higher than the 358 mAh g^{-1} of NCO@N-rGO in a sodium half-cell. A NIC assembled with NCO@N-HG as the anode and an AC as the cathode also delivered a higher energy density of 52 Wh kg^{-1} at a power density of 10,000 W kg^{-1}. The physical and electrochemical properties of magnetite (Fe_3O_4) nanoparticles were also improved by using the 3D N-HG. The thin graphene sheets in the composites facilitate the electron transport and buffer the volume changes during charge/discharge, while the interconnected 3D macroporous network with a pore size in several micrometers range, combined with the nanopores in the N-HG provide pathways for rapid ion transport. The good electrochemical performance of the composites indicates that using N-HG to support TMOs particles is an effective and general approach towards developing high-performance anode materials for sodium-ion storage.

In summary, this PhD thesis work has significantly improved the physical and electrochemical properties of nickel cobaltite with regard to electrical conductivity, structural stability, and sodium ion diffusivity in the bulk electrode. The good electrochemical

performance indicates that NCO-based materials hold a great promise as anode for high-performance NICs with competing energy and power densities.

Declaration by author

This thesis is composed of my original work, and contains no material previously published or written by another person except where due reference has been made in the text. I have clearly stated the contribution by others to jointly-authored works that I have included in my thesis.

I have clearly stated the contribution of others to my thesis as a whole, including statistical assistance, survey design, data analysis, significant technical procedures, professional editorial advice, financial support and any other original research work used or reported in my thesis. The content of my thesis is the result of work I have carried out since the commencement of my higher degree by research candidature and does not include a substantial part of work that has been submitted to qualify for the award of any other degree or diploma in any university or other tertiary institution. I have clearly stated which parts of my thesis, if any, have been submitted to qualify for another award.

I acknowledge that an electronic copy of my thesis must be lodged with the University Library and, subject to the policy and procedures of The University of Queensland, the thesis be made available for research and study in accordance with the Copyright Act 1968 unless a period of embargo has been approved by the Dean of the Graduate School.

I acknowledge that copyright of all material contained in my thesis resides with the copyright holder(s) of that material. Where appropriate I have obtained copyright permission from the copyright holder to reproduce material in this thesis and have sought permission from co-authors for any jointly authored works included in the thesis.

Publications included in this thesis

1 **D. Yang,** X. Sun, K. Lim, R. Ranganathan Gaddam, N. Ashok Kumar, K. Kang and X. S. Zhao. Pre-sodiated nickel cobaltite for high-performance sodium-ion capacitors, *Journal of Power Sources*, 2017, **362**, 358–365.

—Incorporated as Chapter 5.

Contributor	Statement of contribution
Author Dongfang Yang (Candidate)	Designed experiments (90%) Wrote and edited paper (75%) Material characterization (90%)
Author Dr. Xiaoming Sun	Material characterization (10%)
Author Kyungmi Lim	Designed experiments (10%)
Author Rohit Ranganathan Gaddam	Helped to take HR-TEM images
Author Dr Nanjundan Ashok Kumar	Wrote and edited paper (5%)
Author Prof. K. Kang	Wrote and edited paper (5%)
Author Prof. X. S. Zhao	Wrote and edited paper (15%)

2 **D. Yang**, Q. Zhao, L. Huang, B. Xu, N. Ashok Kumar and X. S. Zhao. Encapsulation of $NiCo_2O_4$ in nitrogen-doped reduced graphene oxide for sodium ion capacitors, *Journal of Materials Chemistry A*, 2018, **6**, 14146-14154.

—Incorporated as Chapter 6.

Contributor	Statement of contribution
Author Dongfang Yang (Candidate)	Designed experiments (90%) Wrote and edited paper (85%) Material characterization (80%)
Author Qinglan Zhao	Material characterization (10%)
Author Liqing Huang	Material characterization (10%)
Author Dr. Binghui Xu	Designed experiments (10%)
Author Dr. Nanjundan Ashok Kumar	Wrote and edited paper (5%)
Author Prof. X. S. Zhao	Wrote and edited paper (15%)

3 **D. Yang,** B. Xu, Q. Zhao and X. S. Zhao. Three-dimensional nitrogen-doped holey graphene and transition-metal oxides composites for sodium-ion storage, *Journal of Materials Chemistry A*, 2019, **7**, 363-371.

—Incorporated as Chapter 7.

Contributor	Statement of contribution
Author Dongfang Yang (Candidate)	Designed experiments (90%) Wrote and edited paper (80%) Material characterization (90%)
Author Dr. Binghui Xu	Designed experiments (10%) Wrote and edited paper (10%)
Author Qinglan Zhao	Material characterization (10%)
Author Prof. X. S. Zhao	Wrote and edited paper (10%)

Submitted manuscripts included in this thesis

No manuscripts submitted for publication

Other publications during candidature

Journal papers:

1 Q. Zhao, **D. Yang,** A. K. Whittaker and X. S. Zhao. A hybrid sodium-ion capacitor with polyimide as anode and polyimide-derived carbon as cathode, *Journal of Power Sources*, 2018, **396**, 12–18.

2 Q. Zhao, R. R. Gaddam, **D. Yang,** E. Strounina, A. K. Whittaker and X. S. Zhao. Pyromellitic dianhydride-based polyimide anodes for sodium-ion batteries, *Electrochimica Acta*, 2018, **265**, 702–708.

3 N. Ashok Kumar, R. Ranganathan Gaddam, M. Suresh, S. Rao Varanasi, **D. Yang,** S. K. Bhatia and X. S. Zhao. Porphyrin–graphene oxide frameworks for long life sodium ion batteries, *Journal of Materials Chemistry A*, 2017, **5**, 13204–13211.

4 L. Zhang, L. Li, X. Sun, P. Liu, **D. Yang** and X. S. Zhao. ZnO-Layered Double Hydroxide@Graphitic Carbon Nitride Composite for Consecutive Adsorption and Photodegradation of Dyes under UV and Visible Lights, *Materials,* 2016, **9**, 927.

5 N. A. Kumar, R. R. Gaddam, S. R. Varanasi, **D. Yang,** S. K. Bhatia and X. S. Zhao. Sodium ion storage in reduced graphene oxide, *Electrochimica Acta*, 2016, **214**, 319–325.

6 R. R. Gaddam, **D. Yang,** R. Narayan, K. Raju, N. A. Kumar and X. S. Zhao. Biomass derived carbon nanoparticle as anodes for high performance sodium and lithium ion batteries, *Nano Energy*, 2016, **26**, 346–352.

Conference Proceedings:

1 **D. Yang**, N. Ashok Kumar, and X.S. Zhao, Synthesis of Spherical $NiCo_2O_4$ as Anode for Sodium-Ion Capacitors. Invited talk at Asia-Pacific Conference on Electrochemical Energy Storage & Conversion (APEnergy 2016), 4-8 September 2016, National Tsing Hua University, Hsinchu, Taiwan.

Contributions by others to the thesis

Prof. George Zhao was responsible for setting up this thesis project, providing research resources and advice, correcting thesis report and manuscripts.

Dr. Nanjundan Ashok Kumar was responsible for providing research advice and correcting the chapter 4 and 5 of this thesis.

Statement of parts of the thesis submitted to qualify for the award of another degree

No works submitted towards another degree have been included in this thesis.

Research Involving Human or Animal Subjects

No animal or human subjects were involved in this research

Acknowledgments

I would like to thank my principle supervisor Prof. George Zhao who gave me the precious opportunity to do this project on sodium-ion energy storage. He also gave me patient guidance, encouragement and kind support throughout my PhD research. I would also like to thank my co-supervisor Dr. Nanjundan Ashok Kumar for giving me kind support, valuable suggestions, and discussions.

Many thanks to my colleagues for their kind support and assistance, including Dr. Binghui Xu, Dr. Xiaoming Sun, Ms. Qinglan Zhao, Mr. Rohit Gaddam, Mr. Hao Lu, Ms.Xin Fan, Ms.Yilan Wu, and Mr. Yverick Rangom. Many thanks also go to Dr. Simon smart and Dr. Tom Rufford for being in my thesis committee, and for their important suggestions throughout my PhD candidature study.

A very special gratitude goes to Dr. Wei Wang for helping me edit this thesis. Many thanks also go to my parents and my brother for their support and encouragement which have inspired me all the time.

I would like to thank the China Scholarship Council, the Australian Research Council and the Vice-Chancellor's Research and Teaching Fellowship Program for financial support over the PhD study. I gratefully acknowledge the facilities and technical assistance of the Australian Microscopy and Microanalysis Research Facility at the UQ Centre for Microscopy and Microanalysis.

Financial support

This research was supported by the China Scholarship Council, the Australian Research Council and the Vice-Chancellor's Research and Teaching Fellowship Program.

Keywords

Sodium-ion capacitors, anode, nickel cobaltite, stabilization, graphene, electrochemical properties, sodium-ion storage mechanism

Australian and New Zealand Standard Research Classifications (ANZSRC)

ANZSRC code: 091205, Functional Materials, 50%

ANZSRC code: 090403, Chemical Engineering Design, 30%

ANZSRC code: 090406, Powder and Particle Technology, 20%

Fields of Research (FoR) Classification

FoR code: 0912, Materials Engineering, 50%

FoR code: 0904, Chemical Engineering, 50%

Table of Contents

Abstract I

Acknowledgments IX

Keywords IX

List of figures XV

List of schemes XXI

List of tables XXI

List of abbreviations XXI

Chapter 1 Introduction 1

1.1 Background 1

1.2 Development history of alkali metal-ion capacitors 4

1.3 The working principle of sodium-ion capacitors 5

1.4 Significance and research objectives 9

1.5 Thesis outline 12

Chapter 2 Literature review 14

2.1 Cathode materials 14

2.1.1 Activated carbon 14

2.1.2 Graphene 15

2.1.3 V_2CT_x MXene 15

2.1.4 $Na_2Fe_2(SO_4)_3$ 17

2.1.5 $Na_{0.44}MnO_2$ 18

2.2 Electrolytes 20

2.2.1 Sodium salts 20

2.2.2 Solvents 21

2.3 Anode materials 22

2.3.1 Carbonaceous materials 23

2.3.2 Insertion-type materials 29

2.3.3 Conversion-type materials 41

2.4 Summary and perspectives 42
Chapter 3 Research methodology 44
3.1 Chemical reagents and materials 44
3.2 Materials characterization 45
3.3 Electrochemical measurements 45
3.3.1 Galvanostatic charge and discharge 46
3.3.2 Cyclic voltammetry 46
3.3.3 Electrochemical impedance spectroscopy 46
3.3.4 Ragone plot 47
Chapter 4 Sodium-ion storage performance of thermally treated $NiCo_2O_4$ spheres 48
4.1 Introduction 48
4.2 Experimental section 49
4.2.1 Materials synthesis 49
4.2.2 Materials characterization 50
4.2.3 Electrochemical measurements 50
4.3 Results and discussion 51
4.3.1 Electrochemical performance in sodium half-cells 55
4.3.2 Electrochemical performance in a full sodium-ion capacitor cell 58
4.4 Conclusions 59
4.5 Supplement data 60
Chapter 5 Pre-sodiated $NiCo_2O_4$ for high-performance sodium-ion capacitors 63
5.1 Introduction 63
5.2 Experimental section 65
5.2.1 Materials synthesis 65
5.2.2 Materials characterization 65
5.2.3 Electrochemical measurements 66
5.3 Results and discussion 66
5.3.1 Electrochemical performance in a sodium half-cell 69

5.3.2 Electrochemical performance in a full sodium-ion capacitor cell 70
5.3.3 Sodium-ion storage mechanism 73
5.4 Conclusions 76
5.5 Supplementary data 77
Chapter 6 Encapsulation of $NiCo_2O_4$ in nitrogen-doped reduced graphene oxide sheets for sodium-ion capacitors 79
6.1 Introduction 79
6.2 Experimental section 80
6.2.1 Materials synthesis 80
6.2.2 Materials Characterization 82
6.2.3 Electrochemical measurements 82
6.3 Results and discussion 83
6.3.1 Electrochemical performance in sodium half-cells 86
6.3.2 Electrokinetics study 89
6.3.3 Electrochemical performance in a full sodium-ion capacitor cell 91
6.4 Conclusions 94
6.5 Supplementary data 94
Chapter 7 Three-dimensional nitrogen-doped holey graphene and transition-metal oxides composites for sodium-ion storage 98
7.1 Introduction 98
7.2 Experimental section 100
7.2.1 Materials synthesis 100
7.2.2 Materials characterization 102
7.2.3 Electrochemical measurements 102
7.3 Results and discussion 103
7.3.1 Structure and electrochemical performance in sodium half-cells 103
7.3.2 Electrochemical performance in full sodium-ion capacitor cells 111
7.4 Conclusions 112

7.5 Supplementary data 113
Chapter 8 Conclusions and recommendations 116
8.1 Conclusions 116
8.2 Recommendations 118
References 119

List of figures

Figure 1.1 Energy consumption in the United States from 1776 to 2040.[1] 1

Figure 1.2 An overview of renewable energy resources.[2] 2

Figure 1.3 Ragone plot shows the energy density and power density of different electrochemical energy storage devices.[5] 3

Figure 1.4 A representative scheme of (a) NIB, (b) EC and (c) NIC which adopts one electrode from a NIB and the other electrode from an EC. (I) copper current collector; (II) porous separator in the organic electrolyte; (III) aluminum current collector. 6

Figure 2.1 Schematic of the synthesis procedure and electrochemical performance of Mxene: (a) scheme of the synthesis of V_2CT_x and its sodium intercalation mechanism, (b) GCD profiles of V_2CT_x cathode and hard carbon anode, (c) cycling stability of V_2CT_x at different rates in sodium half-cells, (d) cycling stability of the NIC cell (hard carbon//V_2CT_x) at a high rate (20 C).[40] 16

Figure 2.2 The crystal structure and its electrochemical performance of $Na_2Fe_2(SO_4)_3$: (a) crystal structure of $Na_2Fe_2(SO_4)_3$ projected along the *c* axis and local environment of two independent Fe sites. Green octahedra, yellow tetrahedra, and blue spheres show FeO_6, SO_4 and Na, respectively. Fe ions occupy two kinds of crystallographic sites that show distinctive octahedral geometries. (b) GCD profiles of V_2CT_x anode and $Na_2Fe_2(SO_4)_3$ cathode. (c) GCD profiles of the NIC cell based on the weight of Ti_2CT_x.[74] 18

Figure 2.3 Crystal structure of $Na_{0.44}MnO_2$ (left): two sodium sites (referenced as Na1 and Na2) occupy large S-shaped tunnels, while another site (Na3) is located in the smaller tunnels. *In-situ* XRD patterns recorded at a C/250 rate (right).[86] 19

Figure 2.4 (a) Representation of model for sodium intercalates into HC. (b) Nyquist plots and (c) cycling stability of NICs and LICs.[109] 24

Figure 2.5 (a) Schematic of the NIC assembled with NTHC as the anode and activation/carbonization of APDC as the cathode. (b) SEM and (c) TEM images of NTHC, indicating a nanotube-like morphology. (d) CV curves of NTHC in a sodium half-cell. (e) Ragone plot of the NIC in this work, in comparison with other reported energy storage devices.[32] 25

Figure 2.6 (a) Scheme of the material synthesis process employed for PSNC cathode and PSOC anode. (b) SEM of PSNC. (c) SEM of PSOC. (d) CV curves of PSOC. (e) GCD profiles of the NIC. (f) Ragone plot of the NIC in this work, in comparison with other reported energy storage devices.[25] 26

Figure 2.7 A scheme of the synthesis process for chemically derived graphene.[118] 27

Figure 2.8 (a) Scheme of T_2CT_x preparation: the MAX phase Ti_2AlC was transformed to the MXene Ti_2CT_x nanosheets under the hydrofluoric (HF) acid treatment. (b) CV curves of Ti_2CT_x at 0.2 mV s^{-1} in a sodium half-cell and its corresponding *ex-situ* XRD patterns. Ti_2CT_x exhibited expansion of the interlayer distance after the first intercalation process, then reversibly accommodated sodium ions without significant interlayer distance change.[26] .. 30

Figure 2.9 Schematic of the synthesis approach for M-NTO or M-KTO nanoribbons. Ti_3C_2 MXene was firstly prepared *via* selectively etching Al of Ti_3AlC_2 MAX phase in HF. Then, Ti_3C_2 MXene was hydrothermally treated with NaOH or KOH solution in H_2O_2 to produce M-NTO or M-KTO nanoribbons.[123] 31

Figure 2.10 (a) Schematic illustration of structures of layered MoS_2 (left) and MoS_2–C (right), and the corresponding cycling performance in a sodium half-cell. (b) Schematic illustration of the reaction mechanism of MoS_2–C by electrochemical activation and Ragone plots of the NIC assembled using a MoS_2–C as the anode and a PDPC as the cathode.[33] 32

Figure 2.11 (a) Schematic illustration of the synthesis procedure for Nb_2O_5@C/rGO nanocomposites and a NIC assembled with this Nb_2O_5@C/rGO as the anode and an AC as the cathode. TEM images of (b) Nb_2O_5@C/rGO and (c) Nb_2O_5@C. (d) CV curves of Nb_2O_5@C/rGO-50 with separation between total current and surface capacitive current (shaded regions) at 0.1 mV s^{-1}. (e) GCD profiles of Nb_2O_5@C/rGO-50 at 0.025 A g^{-1} in a sodium half-cell. (f) Ragone plots of the NIC in this work, in comparison with the performance of other NICs.[28] 33

Figure 2.12 (a) Schematic illustration of the synthesis procedure for NTO/Carbon textiles. (b) SEM of NTO/Carbon textiles. (c) GCD profiles of NTO/Carbon textiles in a sodium half-cell at 100 mA g^{-1}. (d) Schematic illustration of the flexible NIC device assembled with the NTO/CT as the anode and GF as the cathode. (e) Ragone plot of the NIC in this work, in comparison with the performance of other flexible devices.[30] 35

Figure 2.13 SEM (a) and TEM (b, c) of MWTOG, and inset of b shows the SAED pattern of TiO_2. (d) Cycling stability of MWTOG electrode at 5 C and 10 C versus Na^+/Na. (e) Plot of capacity *versus* $v^{-1/2}$ to separate diffusion-controlled and capacitive-controlled contributions. and inset represented that the capacitive process has accounted for 73% of the stored charge at 3 mV s^{-1}. (f) Ragone plot of the NIC in this work, in comparison with the performance of other representative energy storage devices.[35] 37

Figure 2.14 (a) SEM image of V_2O_5/CNT. (b) Schematic of a nanocomposite consisting of interpenetrating networks of V_2O_5 nanowires and CNTs. (c)The CV curves at a scan rate of 10 mV s^{-1}. The shaded region represented the capacitive current contribution, which accounted for 82% of the total measured current. (d) Ragone plot of the NIC in this work, in comparison with the performance of other prototype supercapacitors.[19] 39

Figure 4.1 (a) XRD pattern and (b) TGA curve of the as-prepared intermediate product...51

Figure 4.2 XRD patterns of (a) NCO-250^{o}C, (b) NCO-350^{o}C and (c) NCO-450^{o}C. 52

Figure 4.3 FESEM images of (a,b) NCO-250^{o}C, (c,d) NCO-350^{o}C and (e,f) NCO-450^{o}C..53

Figure 4.4 TEM images of (a) NCO-250^{o}C, (b) NCO-350^{o}C and (c) NCO-450^{o}C.....54

Figure 4.5 CV curves of NCO samples for the 3rd cycle from 0.005 to 2.5 V versus Na^+/Na at a scan rate of 0.2 mV s^{-1}. 56

Figure 4.6 GCD curves between 0.005 V and 2.5 V versus Na^+/Na at a current rate of 100 mA g^{-1} for the 2nd, 50th, and 100th cycles of (a) NCO-250^{o}C, (b) NCO-350^{o}C, (c) NCO-450^{o}C. 57

Figure 4.7 (a) Cycling stability at a current rate of 100 mA g^{-1} and (b) rate capability of NCO-based electrodes. 58

Figure 4.8 (a) CV plots, (b) GCD curves, (c) Ragone plot of the NCO//AC NIC and (d) its cycling performance at a current rate of 3 A g^{-1}. 59

Figure.S4.1 (a) XRD pattern and (b) SEM image of NiO sample……..60

Figure S4.2 FESEM images of the intermediate product……...61

Figure S4.3 TEM images of (a) low and (b) high magnification of the intermediate product..61

Figure S4.4 Nitrogen adsorption/desorption isotherms of NCO samples……61

Figure S4.5 (a) Cyclic voltammetry curves, (b) GCD profiles for the 1st, 2nd, 50th, and 100th cycles and (c) cycling stability at a current rate of 100 mA g^{-1} of NiO sample……..……..…62

Figure 5.1 (a, b) SEM images, and (c, d) TEM images of the NCO sample before pre-sodiation. 67

Figure 5.2 XPS spectrum of (a) survey spectrum, (b) Ni 2p, (c) Co 2p and (d) O 1s for NCO. 68

Figure 5.3 Electrochemical performance of the NCO electrode before pre-sodiation in a sodium half-cell: (a) CV curves at a scan rate of 0.2 mV s^{-1}, (b) GCD profiles at current rates of 0.1 A g^{-1} and 1 A g^{-1}, (c) specific capacities at different current rates, and (d) cycling performance at a current rate of 1 A g^{-1}. 70

Figure 5.4 (a) GCD curves and (b) specific capacitance as a function of mass ratio between cathode and anode at 0.5 A g^{-1} of Na_nNCO//AC NIC. 71

Figure 5.5 CV plots of the Na_nNCO//AC (a) and the NCO//AC NICs (d), GCD curves of the Na_nNCO//AC NIC (b and c) and the NCO//AC NIC (e and f) at different current rates, (g) Ragone plot of the Na_nNCO//AC cell in comparison with other AC-based NIC cells, and (h) cycling performance of the Na_nNCO//AC NIC at 3 A g^{-1}.....73

Figure 5.6 (a) First charge/discharge curves of the NCO electrode at 0.1 A g^{-1} and (b) *ex-situ* XRD patterns of electrode samples before and after charge/discharge. 74

Figure 5.7 *Ex-situ* TEM SAED patterns of (a) pristine NCO, (b) D-0.7V, (c) D-0.005V, (d) C-1.2V, and (e) C-2.5V. 75

Figure S5.1 (a) XRD pattern and (b) Nitrogen adsorption-desorption isotherm with inserted corresponding pore size distribution of NCO……..77

Figure S5.2 Electrochemical properties of the symmetric AC//AC supercapacitor: (a) CV plots, (b and c) GCD curves, (d) Ragone plot……77

Figure S5.3 *Ex-situ* TEM images of NCO before (a) and after discharge to 0.005 V (b) and charge to 2.5 V (c)……78

Figure 6.1 The morphology and microstructure characterization of NCO@N-rGO: (a-c) SEM images at different magnifications, (d) TEM image, (e) HAADF-STEM image and elemental mapping results. 84

Figure 6.2 (a) XRD patterns of NCO@N-rGO and the standard NCO (JCPDS card no. 73-1702). (b) XPS survey of NCO@N-rGO. (c, d and e) High-resolution XPS spectrum of Ni 2p, Co 2p and N 1s for NCO@N-rGO, respectively. (f) High-resolution XPS spectrum of C 1s for NCO@N-rGO and GO. 86

Figure 6.3 (a) GCD profiles of NCO@N-rGO at various current densities from 0.05 to 5.0 A g^{-1}. (b) Rate performance of NCO and NCO@N-rGO electrodes. (c) Cycling performance combined with coulombic efficiency of NCO@N-rGO, NCO and N-rGO electrodes at 0.1 A g^{-1}. (d) Cycling performance combined with coulombic efficiency of NCO@N-rGO at 1 A g^{-1}. (e) A schematic illustration of the NCO@N-rGO electrode reacting with sodium ions upon charge/discharge, showing the function of graphene sheets for stabilizing NCO crystals and improving the electronic conductivity. (f) Nyquist plots of NCO and NCO@N-rGO electrodes. 89

Figure 6.4 Kinetics analysis of the electrochemical behavior towards sodium ions for NCO@N-rGO electrode. (a) CV curves at various sweep rates from 0.2 to 1.2 mV s^{-1}. (b) Peak current dependence on the scan rate, used to determine the capacitive and intercalation contributions to energy storage. (c) Quantitative contributions of surface capacitive and diffusion-controlled faradic reactions to sodium-ion storage. (d) CV curve of NCO@N-rGO with separation between total current (solid line) and surface capacitive current (shaded regions) at 1 mV s^{-1}.....91

Figure 6.5 (a) CV curves of NCO@N-rGO and AC in half cells (top) and full cell of NIC (bottom) at 5 mV s^{-1}, indicating the voltage window of the full cell from 0.1 to 3.8 V. (b) GCD profiles at 0.2-5 A g^{-1}. (c) The long-term cycle life of NIC at 2 A g^{-1}, with inset of rate capability of the NIC at various current densities from 0.2 to 5 A g^{-1}. (d) Ragone plots in comparison with representative graphene-based NICs in literature. 93

Figure S6.1 Zeta potential profiles of PDDA-modified NCO and GO in the pH range between 2 and 10.....94

Figure S6.2 SEM images of NCO particles.....95

Figure S6.3 XRD patterns of GO, N-rGO and NCO.....95

Figure S6.4 TGA of NCO@N-rGO.....96

Figure S6.5 (a) b-values plotted as a function of potential for anodic and cathodic sweeps. (b) The electrochemical reactions were divided into four regions (A1*, A2*, C1*, and C2*)…….. 97

Figure 7.1 (a) TEM images of N-HG sheets with etched pores. (b-c) SEM images of NCO@N-HG at different magnifications. (d and e) TEM and HRTEM images, (f) SAED pattern, and (g) HAADF-STEM image and elemental mapping results of NCO@N-HG..105

Figure 7.2 (a) XRD pattern of NCO@N-HG and the standard NCO JCPDS card (no. 73-1702). (b) XPS survey of NCO@N-HG. (c, d and e) High-resolution XPS spectrum of Ni 2p, Co 2p and N 1s for NCO@N-HG, respectively. (f) High-resolution XPS spectrum of C 1s for NCO@N-HG (bottom) and GO (top). 106

Figure 7.3 (a) CV curves at a scan rate of 0.2 mV s^{-1}, (b) GCD profiles at various current densities from 0.1 to 2.0 A g^{-1}, and (c) cycling performance at 1 A g^{-1} of NCO@N-HG. (d) Rate performance from current densities from 0.05 to 5.0 A g^{-1}, (e) cycling performance at 0.1 A g^{-1} and (f) Nyquist plots of NCO@N-HG, NCO@G and NCO electrodes. 108

Figure 7.4 (a, b) SEM images, (c-d) TEM images, (e) SAED pattern and (f) HAADF-STEM image with elemental mapping results of the Fe_3O_4@N-HG.....109

Figure 7.5 (a) CV curves at a sweep rate of 0.2 mV s^{-1} and (b) GCD profiles at various current densities from 0.1 to 2.0 A g^{-1} of Fe_3O_4@N-HG. (c) Rate performance from current densities from 0.05 to 5.0 A g^{-1} and (d) cycling performance of Fe_3O_4@N-HG, Fe_3O_4@G, and Fe_3O_4 electrodes at 0.1 A g^{-1}.....111

Figure 7.6 GCD curves of (a) NCO@N-HG//AC and (b) Fe_3O_4@N-HG//AC. (c) Ragone plot of the NICs. (d) Cycling performance of NICs at 3 A g^{-1}.....112

Figure S7.1 SEM images of (a) NCO@G (the inset shows its TEM image), (b) NCO, (c) Fe_3O_4@G and (d) Fe_3O_4.....113

Figure S7.2 (a) Argon adsorption/desorption isotherms and (b) DFT pore size distributions of NCO@N-HG.....114

Figure S7.3 XRD patterns of GO (top) and N-HG (bottom)……114

Figure S7.4 TGA curves of NCO@N-HG and Fe_3O_4@N-HG.....115

Figure S7.5 (a) Argon adsorption/desorption isotherms, (b) DFT pore size distributions of Fe_3O_4@N-HG. (c) XRD patterns for Fe_3O_4@N-HG and the standard Fe_3O_4 (JCPDS card no. 75-0033)……..…...115

List of schemes

Scheme 6.1 Schematic and photograph illustration of the preparation of NCO@N-rGO: (1) formation of NCO@GO via electrostatic attraction, (2) dispersing NCO@GO in a urea-dissolved GO suspension for hydrothermal treatment to obtain NCO@N-rGO.....83

Scheme 7.1 The overall synthetic procedure of TMO@N-HG: (1) preparation of HGO by etching GO sheets with H_2O_2, (2) preparation of TMO@G using a hydrothermal method, (3) dispersing TMO@G in a urea-dissolved HGO suspension for hydrothermal treatment to obtain TMO@N-HG.....103

List of tables

Table 1.1 Landmarks in the history of the NIC research…….....4

Table 3.1 Chemicals and reagents used to prepare electrode materials…….....44

Table S6.1 Fitting results of the EIS spectra in Figure 6.3f using the inserted equivalent circuit…….96

Table S6.2 Quantitative contributions of capacitive sodium ions storage for different electrochemical regions in Figure S6.5b……..97

List of abbreviations

AC	Activated carbon
AR	Analytical reagent
BET	Brunauer-Emmett-Teller
BJH	Barrett-Joyner-Halenda
CV	Cyclic voltammetry

CVD	Chemical vapour deposition
CNT	Carbon nanotube
CFC	Carbon fiber cloth
CoHCF	Cobalt hexacyanoferrate
CMC	Sodium carboxymethyl cellulose
DI	Deionized
DFT	Density functional theory
EES	Electrical energy storage
ESW	Electrochemical stability window
EIS	Electrochemical impedance spectroscopy
EC	Electrochemical capacitors
EDLC	Electric double layer capacitance
FESEM	Field-emission scanning electron microscope
GO	Graphene oxide
GCD	Galvanostatic charge and discharge
G	Graphene
HEV	Hybrid electric vehicle
HF	Hydrogen fluoride
HC	Hard carbon
HRTEM	High resolution transmission electron microscopy
HAADF-STEM	High-angle annular dark-field scanning TEM
HG	Holey graphene
HGO	Holey graphene oxide
LIB	Lithium-ion battery
LIC	Lithium-ion capacitor
MG	Macroporous graphene
MCMB	Mesocarbon microbeads

NIB	Sodium-ion battery
NIC	Sodium-ion capacitor
NCO	Nickel cobaltite ($NiCo_2O_4$)
N-rGO	Nitrogen doped reduced graphene oxides
N-HG	Nitrogen-doped holey graphene
NTHC	Nanotube-like hard carbon
NPs	Nanoparticles
PSDC	Peanut shells derived carbon
PDPC	Polyaniline derived porous carbon
PANI	Polyaniline
PSNC	Peanut shell nanosheets carbon
rGO	Reduced graphene oxide
SEI	Solid electrolyte interphase
SEM	Scanning electron microscopy
SAED	Selected area electron diffraction
TEM	Transmission electron microscopy
TGA	Thermal gravimetric analysis
TMO	Transition-metal oxides
US	United States
2D	Two-dimensional
3D	Three-dimensional
XPS	X-ray photoelectron spectroscopy
XRD	X-ray diffraction

Chapter 1 Introduction

This chapter gives an overall introduction of research, including background, development history, the working principle of sodium-ion capacitors, research objectives, and thesis outline.

1.1 Background

The fossil fuels, such as petroleum, natural gas, and coal have aroused ever-increasing concerns on environmental pollution, global warming, and resource limitation. Shifting to clean and renewable energy such as nuclear, solar wind, wave and hydropower is occurring worldwide. According to United States (US) Energy Information Administration (EIA), fossil fuels consumption in the US has accounted for more than 80% of total energy consumption for more than 100 years (1900-2015), but this is predicted to decline to 76.6% by 2040 (Figure 1.1).[1] Future growth in energy consumption will primarily emerge in natural gas and renewable energy. Particularly, renewable energy can help people to achieve the goals of reducing greenhouse gas emission, limiting future climate change risks and ensuring reliable and sustainable energy supply.

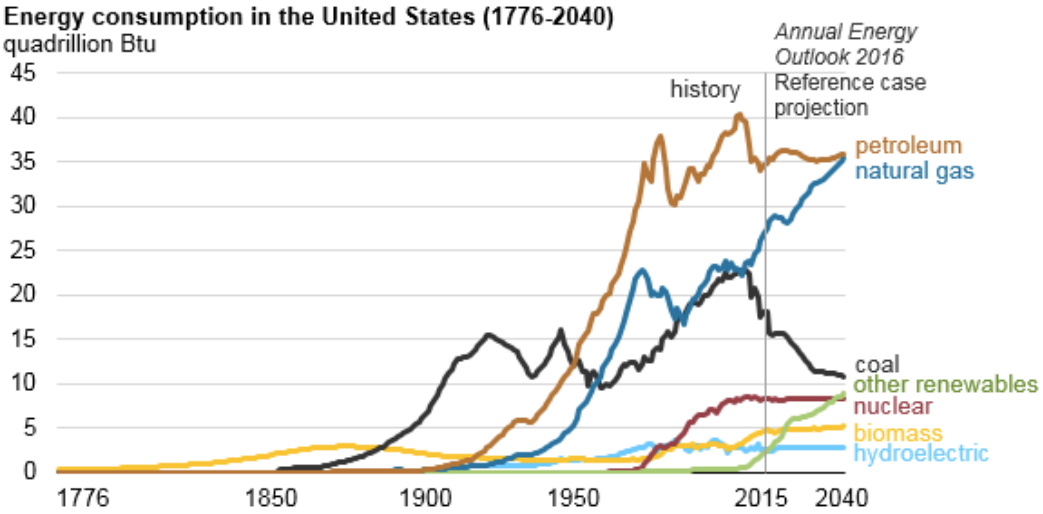

Figure 1.1 Energy consumption in the United States from 1776 to 2040.[1]

Figure 1.2 shows an overview of various renewable energy sources.[2] Most of these energy sources are derived from natural sources such as wind, marine, solar and geothermal. However, the renewable energy does not generate in regular patterns because it primarily depends on specific weather such as sunlight exposure for solar generation, which cannot satisfy the modulate patterns of demand. Therefore, using an electrical energy storage (EES) technology to store the generated energy during low-demand periods and deliver it during peak-periods is very important.

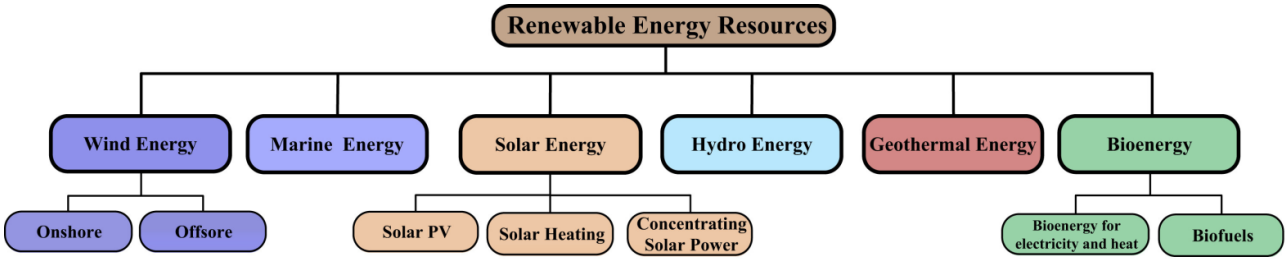

Figure 1.2 An overview of renewable energy resources.[2]

The most prevalent EES technologies are pump hydro and compressed air, which dominate the total capacity today.[3] As batteries and capacitors storage systems are well suited for portable electronics and electric vehicles (EVs), they are also important EES technologies which are developing fast with lower cost and improved performance.[4] Figure 1.3 compares the batteries, capacitors and fuel cells storage systems regarding power rating and energy densities.[5] In general, these electrochemical energy storage technologies possess the features including flexibility, environmental-friendly, high energy conversion efficiency, and simple maintenance to meet different grid functions.[6] Several battery technologies including lead acid, sodium sulfate, and rechargeable batteries have been developed for commercial application. Among them, the rechargeable batteries are the most promising and commercialized electrochemical energy storage.[7]

Lithium-ion batteries (LIBs), as a typical rechargeable battery, have become the dominant power source for portable electronic devices such as cell phones and laptops. However, their commercialization has resulted in a large amount of lithium consumption, which has accounted for one-quarter of the world's production of lithium mine, resulting in a rapid rise in the price of lithium in the latest decade.[8] Driven by this situation, research interests in

sodium-ion system have been aroused. As sodium is a naturally abundant alkali element and it shares similar chemistry with lithium, sodium-ion batteries (NIBs) have been considered as a promising alternative to LIBs, especially in large-scale grid energy storage.[9] However, as shown in Figure 1.3, the rechargeable batteries including LIBs and NIBs generally show low power density (<1000 W kg^{-1}) which cannot satisfy the situations when requiring high power energy. Electrochemical capacitors (ECs) store energy using either ion adsorption (electrical double-layer capacitors, EDLCs) or surface redox reactions (pseudocapacitors) or both of them with prominent properties, such as high power density, and long cycle life. However, the energy density of ECs is usually low (<10 Wh kg^{-1}). Thus, special energy storage devices are highly desired with a high energy density close to that of rechargeable batteries, and a high power density similar to that of ECs.

Lithium-ion capacitors (LICs) and sodium-ion capacitors (NICs) are typical examples of such special energy storage systems, which integrate the electrode component of ECs and rechargeable LIBs/NIBs.[10,11] This integration enables the LICs/NICs to exhibit a higher energy output than ECs and a higher power output than LIBs/NIBs. The hybrid LICs were reported earlier than NICs, but NICs have aroused more research interests than LICs because sodium is a naturally abundant alkali element and shares similar chemistry with lithium.

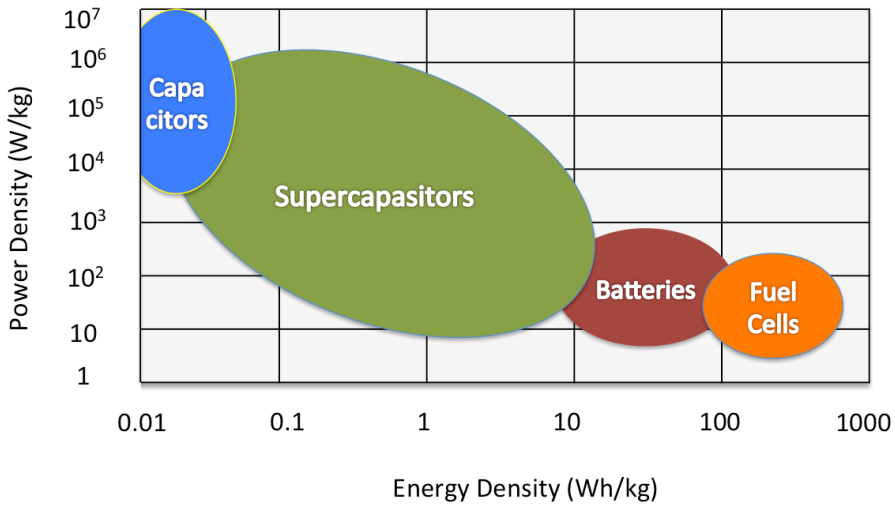

Figure 1.3 Ragone plot shows the energy density and power density of different electrochemical energy storage devices.[5]

1.2 Development history of alkali metal-ion capacitors

Amatucci and co-workers were the first to demonstrate a LIC cell with an activated carbon (AC) as the cathode and a nanostructured $Li_4Ti_5O_{12}$ as the anode, which delivered an energy density up to 20 W h kg^{-1}, about three times higher than that of carbon-based ECs.[12] This discovery was followed later by constructing LICs of TiO_2//CNT[13], $LiTi_2(PO_4)_3$//AC,[14] V_2O_5//CNT,[15] TiO_2//graphene[16] and so on. The most inspiring breakthrough in LICs technology happened when JSR Micro Inc. introduced a pre-lithiated carbon-based LIC manufactured by its owned subsidiary JM Energy to the commercial market in 2008, and it achieved four times higher energy density than conventional ECs.[17] After that, in 2016, Maxwell Technologies have confirmed the commercialization of LICs to recoup regenerative energy in China's railway system.[18]

NICs have attracted significant attention as an alternative for LICs because sodium is an abundant element in nature. In 2012, Chen *et al*.[19] fabricated a NIC using a V_2O_5/CNT composite as the anode and an AC as the cathode, which delivered comparable energy density and power density to LICs. After that, Research on NICs has grown rapidly. A number of electrode materials (*e,g.,* hard carbon, peanut carbon, TiC, Nb_2O_5, $Na_2Ti_3O_7$, TiO_2, $NiCo_2O_4$, *etc*.) were studied for NICs. Table 1.1 lists the landmarks in the history of NIC research. The research paper of NIC was firstly published in 2012, and it has grown rapidly since 2015. The growing trend indicates that researchers have strong interests to explore NICs. The anode and cathode electrodes of NICs listed in Table 1.1 are discussed in details in Chapter 2.

Table 1.1 Landmarks in the history of NIC research.

NIC (Anode electrode//cathode electrode)	Reported year
V_2O_5/CNT//AC[19]	2012
sodium pre-doped hard carbon//AC[20]	2012
$Na_2Ti_3O_7$ nanotubes//AC[21]	2012
Spinel $NiCo_2O_4$//AC[22]	2013

MoS_2/G//MoS_2/G[23]	2014
Mesocarbon microbead//AC[24]	2014
Peanut shells derived carbon (PSDC)//PSDC[25]	2015
MXene Ti_2CT_x//$Na_2Fe_2(SO_4)_3$[26]	2015
$Na_2Ti_3O_7$@CNT//PSDC[27]	2015
Nb_2O_5@C/rGO//AC[28]	2016
Nb_2O_5 Nanosheets//PSDC[29]	2016
$Na_2Ti_3O_7$ nanosheets onto carbon textiles//rGO[30]	2016
Nitrogen-doped anatase TiO_2 nanospheres//AC[31]	2016
Nanotube-like hard carbon//activation/carbonization of polyaniline nanotubes[32]	2017
MoS_2–C//homemade polyaniline derived porous carbon[33]	2017
$Na_2Ti_2O_4(OH)_2$//chemically activated rice husk derived porous carbon[34]	2017
Mesoporous single-crystal-like TiO_2@G//AC[35]	2017
V_2O_5 @rGO//honey derived AC[36]	2017
$NaTi_2(PO_4)_3$/rGO//(AC)[37]	2017
B_2X_3/CFC//CFC (carbon fiber cloth)[38]	2017
Quasi-cubic mesoporous $NaTi_2(PO_4)_3$ nanocages//AC[39]	2018
Hard carbon//V_2CT_x[40]	2018

1.3 The working principle of sodium-ion capacitors

NICs generally adopt one electrode from NIBs and the other one from ECs, utilizing both faradaic and non-faradaic mechanisms to store charges to achieve a higher energy density than that of EDLCs and a higher power density than that of NIBs. A typical NIB includes a sodium-intercalated anode and a sodium-deintercalated cathode, as shown in Figure 1.4a. During charge and discharge process, sodium ions shuttle between the anode and cathode electrodes.[41] Figure 1.4b shows the mechanism of an EC. It stores energy using either

anion/cation adsorption (electrical double-layer capacitors, EDLCs) or surface redox reactions (pseudocapacitors) during charge. During discharge, the anion/cations are released from the electrodes.[42] A NIC integrates the characteristics of NIBs and ECs by using the anode and cathode from each of them, and its mechanism scheme is shown in Figure 1.4c. During charge, sodium ions from electrolyte intercalate into the anode, to keep the electrolyte neutrality, the anion ions would transport to the cathode using either adsorption or surface redox reactions. While during discharge, the sodium ions de-intercalate from the anode and the anion ions released from the cathode would transport back to the electrolyte, in the meantime, the current flows from the cathode electrode through the outer electric circuit to the anode electrode.[21]

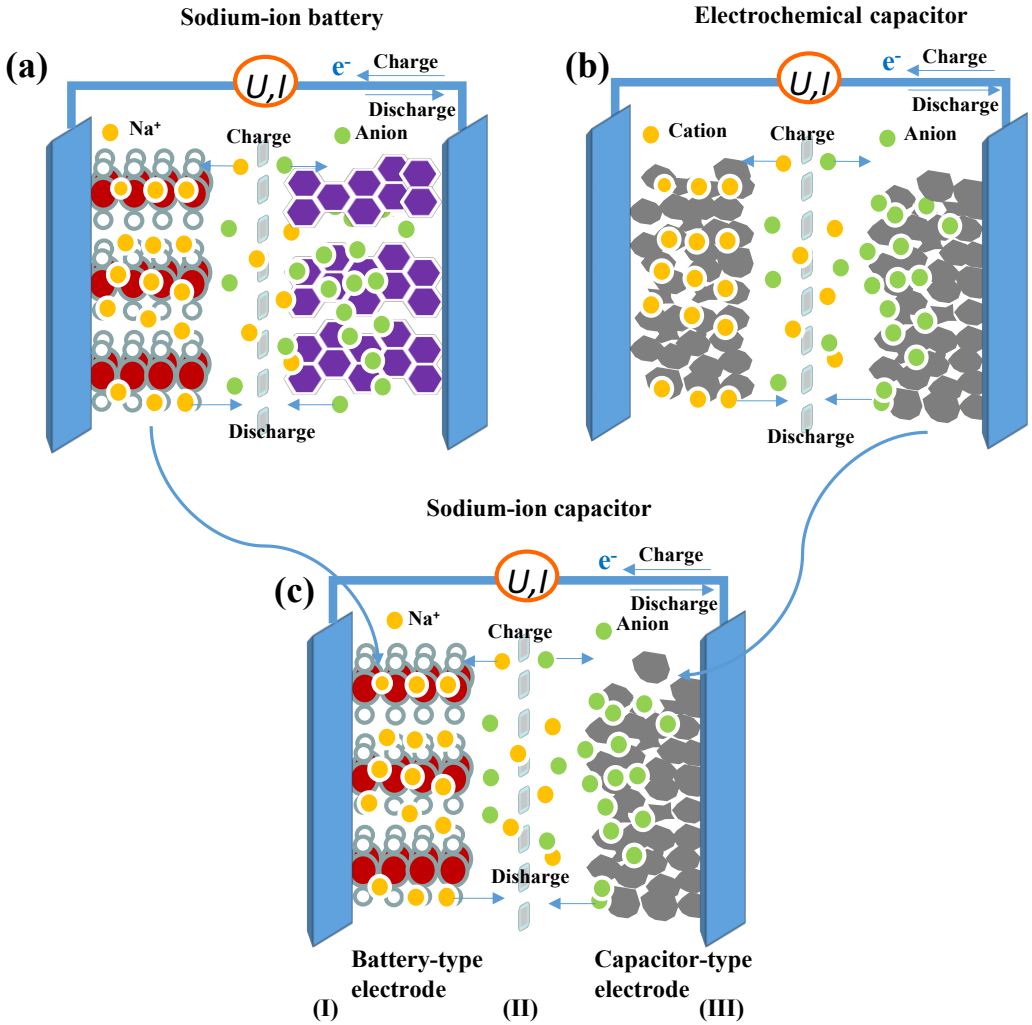

Figure 1.4 A representative scheme of (a) NIB, (b) EC and (c) NIC which adopts one electrode from a NIB and the other electrode from an EC. (I) copper current collector; (II) porous separator in the organic electrolyte; (III) aluminum current collector.

The NIC capacitance (C in F g^{-1}) is defined as the amount of charge that can be stored under an applied potential, which is given by:

$$C=\frac{d\Delta q}{dV} \quad (1\text{-}1)$$

where Δq is the electrochemical equivalence, representing the charge change ratio under a potential, V is the range of applied potential (in V). The actual capacitance (C in F g^{-1}) of a NIC can be calculated based on a typical galvanostatic charge and discharge (GCD) test, using the equations below:

$$C=\frac{i}{mdV/dt} \quad (1\text{-}2)$$

where i is the discharge current (in A), m is the total mass of the electrodes (in g), dV/dt is the slope of the discharge curve. The dV/dt can be calculated by:

$$dV/dt=(V_t-V_f)/(t_2-t_1) \quad (1\text{-}3)$$

where V_t is the potential after IR-drop (in V), V_f is the final potential to be discharged (in V), t_2-t_1 is the discharge time (in s).

In addition, in order to couple both high capability of the anode and the cathode in NIC, the charge between the anode and the cathode should be balanced according to an equation ($Q_{anode}=Q_{cathode}$). The stored charge is calculated by the specific capacity (C), the mass (m) and the potential range (V) in the charge and discharge process of the electrode by $Q= m\times C\times V$. Therefore, the mass ratio between the anode and the cathode can be optimized by:

$$\frac{m_{anode}}{m_{cathode}}=\frac{C_{anode}\times V_{anode}}{C_{cathode}\times V_{cathode}} \quad (1\text{-}4)$$

The mass loading of the anode (m_{anode}, in mg cm^{-2}) can be calculated by：

$$m_{anode}=w\times\frac{m_t-m_c}{s} \quad (1\text{-}5)$$

where *w* (in %) is the content of the active material in electrode slurry, m_t (in mg) is the total mass of the anode electrode, m_c (in mg) is the mass of the bare copper foil, *S* (in cm^2) is the area of the copper substrate. The mass loading of the cathode can be similarly calculated.

To determine the electrochemical properties of one electrode in NIC, researchers usually use a sodium ion half-cell to test its specific capacity, cycling, and rate performance. Taking a metal-oxide anode electrode as an example, a typical half-cell can be represented below:

(+) MO_x| 1M sodium-based organic electrolyte| Na (-) (1-6)

where M stands for Ni, Co, Sn, Fe, *etc.*, the electrochemical reaction occurs as the following:

$$MO_x + yNa^+ + ye^- \underset{discharge}{\overset{charge}{\rightleftharpoons}} M + Na_yO_x \quad (1\text{-}7)$$

The theoretical capacity of the electrode material is generally given:[43]

$$C_o = 26.8\, n\, \frac{m_o}{M} \quad (1\text{-}8)$$

where C_o stands for the theoretical capacity (in Ah), m_o is the mass of the active electrode material involving in the electrochemical reaction (in g), *M* is the molar weight (in g mol^{-1}), and *n* is the number of electrons participating in the reaction.

For example, the theoretical capacity of nickel cobaltite ($NiCo_2O_4$) anode in sodium half-cell is calculated as below:

$NiCo_2O_4 + 8Na^+ + 8e^- \xrightarrow{Charge} Ni + 2Co + 4Na_2O$

$C_o(NiCo_2O_4) = 26.9 \times 8 \times \frac{1}{241} \times 1000 = 892$ (mAh g^{-1})

The actual capacity C_a (in mAh g^{-1}) of the electrode at a current rate based on a sodium half-cell is:

$$C_a = \int_{t_1}^{t_2} I(t)dt \quad (1\text{-}9)$$

where I is the discharge current (in mA g^{-1}), t is the discharge time (in h), t_1 and t_2 are the start time and end time of discharge process, respectively.

1.4 Significance and research objectives

A NIC cell is generally configured with a battery electrode as the anode, an EC electrode as the cathode and an electrolyte containing sodium ions. It has achieved both high energy density and power density to bridge between a NIB and an EC, holding a great promise for large-scale energy storage applications for the grid and electric hybrid vehicles (HVs). The key requirement for NICs is to find suitable electrode materials as they greatly affect the electrochemical performance such as the specific capacity, rate capability, and energy density. The cathodes are mainly carbonaceous-based materials including AC and graphene. Another type of cathode involving in sodium ions intercalation/de-intercalation has also been developed, which are large tunnel-structured materials including MXenes and $Na_2Fe_2(SO_4)_3$.

For battery-type anode materials in NICs, the choice is more restricted. As sodium ions are larger than lithium ions (0.106 nm versus 0.076 nm), sodium-ion energy storage devices generally deliver less energy with a lower power density due to their limited capacity, large volume change and slow kinetics of electrode materials.[9] On the other hand, graphite, as a common anode for lithium-ion energy storage devices, generally shows no staged intercalation with sodium ions when used as an anode in sodium-ion system.[44] This indicates that the main research attempts in NICs should toward the development of high-performance anode materials. The previous studies of anode materials are focused on the insertion-type materials inheriting large sodium ions diffusion tunnels, such as TiO_2,[35,45] Nb_2O_5,[28,46] $Na_2Ti_3O_7$,[30] MXenes,[26] V_2O_5,[19] and the conversion-type materials such as SnS_2,[47] and $NiCo_2O_4$[22,48]. Amongst, nickel cobaltite ($NiCo_2O_4$) with rich electroactive sites are promising anode materials for sodium-ion storage.[49]

$NiCo_2O_4$ (NCO) is a typical transition metal oxide (TMO) which possesses better electrical conductivity and electrochemical activity at least two orders of magnitude higher than pure Co_3O_4 and NiO. Also, its multiple oxidation states and various nanostructures can enable rich redox reactions for NCO to store more charge, which exhibits a high theoretical specific capacity (~890 mAh g^{-1}) in sodium-ion energy storage. In addition, Ni and Co are abundant on earth; thus, it seems to be a promising opportunity for NCO to be widely used and industrialized as an electrode material.[50,51] However, NCO suffers from low electronic/ionic conductivity and large volume changes during repeated cycles, resulting in poor rate capability, inferior power density, and poor cycling stability.[52]

Strategies have been demonstrated to improve the electrochemical performance of NCO. First is fabricating nano-constructed electrodes with preferable morphologies such as nanoneedles,[53] urchin-like microspheres,[54] and nanobox,[55] to shorten the electronic transport, alleviate volume change and facilitate ionic diffusion. Second is introducing highly-conductive coatings or additives like graphene[56,57] and carbon nanotubes[58] to make NCO-based composite electrode materials to increase the electrical conductivity and withstand the large volume change.

Graphene with a monolayer of SP^2 carbon atoms located in 2D honeycomb network, is a very promising carbon material to improve the performance of NCO because it is electrically conductive and suitable for wrapping/encapsulating/supporting NCO particles to alleviate the volume changes.[59–63] Apart from stabilizing TMOs, graphene itself can reversibly store sodium ions the surfaces, edges and covalent sites of graphene sheets,[64] and thereby, beneficial for energy storage. Moreover, doping nitrogen (N) and creating pores in graphene can improve the wettability between graphene and an organic electrolyte,[65] to facilitate the transport of sodium ions and electrons. Therefore, in this thesis work, sustained efforts have been paid to design a unique porous and conductive nitrogen doped reduced graphene oxides (N-rGO) framework to stabilize the NCO in sodium-ion energy storage.

While graphene is an excellent carbon material, graphene sheets tend to stack or agglomerate during electrochemical reactions, leading to blockage of some ion transport pathways.[66,67] Using three-dimensional (3D) porous graphene aerogels with 3D ion diffusion channels to support NCO has been shown to be an effective approach to fabricating NCO-graphene composite electrode materials.[60] However, ion transport across the basal plane

of individual two-dimensional (2D) graphene sheets is still a great challenge to overcome.[68] One strategy to solve this problem is to introduce nanoholes in graphene sheets.[69,70] Therefore, it can be expected that constructing a 3D porous architecture consisting of nitrogen-doped holey graphene (N-HG) and the NCO could significantly facilitate electron and sodium ion transport throughout the entire architecture.

The objectives of this PhD project were to significantly improve the electrochemical properties of NCO in NICs by using a number of strategies and methods as outlined below:

(1) Develop a facile, cost-efficient, and green synthesis way to prepare NCO materials.
(2) Crystal structure control of NCO by a thermal treatment to achieve an optimal electrochemical performance in NICs.
(3) Mechanism study of sodium-ion storage to understand the charge storage behavior in NCO so as to improve its performance.
(4) Use the designed N-rGO architecture to encapsulate NCO particles to improve the physical and electrochemical properties of NCO in NICs.
(5) Use the designed 3D N-HG framework to alleviate the large volume changes of NCO during charge/discharge, prohibit particle aggregation, and facilitate the electron and ions transport. Extend this approach to modify magnetite (Fe_3O_4) nanoparticles for sodium-ion storage.

1.5 Thesis outline

This thesis includes eight chapters as outlined below:

Chapter 1 gives an overall introduction of this thesis research work, including research background and significance, the working principle of NIC, and objectives of this project.

Chapter 2 provides a comprehensive literature review on the development of NICs, electrode materials and electrolytes.

Chapter 3 describes the chemicals, the experimental methods and technical measurements used in this thesis project.

Chapter 4 presents the synthesis and electrochemical properties of spherical NCO thermally treated at different temperatures. It was found that the NCO sample thermally treated at 350 ^{o}C showed an optimal and promise performance in NICs.

Chapter 5 studies the sodium-ion storage mechanism in NCO, and demonstrates that pre-sodiation of NCO can significantly improve its energy density. A NIC assembled with the pre-sodiated NCO as the anode and an AC as the cathode exhibited a high energy density and a high power density.

Chapter 6 describes an approach to improve the physical and electrochemical properties of NCO by encapsulating NCO particles in the designed porous N-rGO framework. The N-rGO guarantees a good electronic conductivity and serves as a buffer to alleviate the volume change in the NCO. As expected, better cycling performance and rate capability of sodium-ion storage were achieved.

Chapter 7 describes an approach to improve the electrochemical properties of NCO and Fe_3O_4 by introducing N-HG to respectively support $NiCo_2O_4$ and Fe_3O_4 nanoparticles via a hydrothermal assembly, forming 3D NCO@N-HG and Fe_3O_4@N-HG composites. The thin graphene sheets in the above composites facilitate the electron transport and buffer the volume changes, while the interconnected 3D macroporous network with a pore size in

several micrometers range, combined with the nanopores in the N-HG provide pathways for rapid ion transport. As anode materials, both composites showed inspiring sodium-ion storage capability. The good electrochemical performance of the composites indicates that using N-HG to support TMOs particles is an effective and general approach towards developing high-performance anode materials for sodium-ion storage.

Chapter 8 summarizes the highlights of this thesis and gives recommendations for future research.

Chapter 2 Literature review

This chapter gives a brief introduction of different components, and summarizes the latest research papers and achievements for sodium-ion capacitors (NICs). A NIC is assembled with a cathode, an electrolyte, a separator and an anode. The cathode materials are generally carbonaceous materials which serve as a capacitor-type electrode participating in the cations adsorption/de-adsorption or surface redox reactions (activated carbon, graphene, *etc.*) or large tunnel-structured materials (MXenes, $Na_2Fe_2(SO_4)_3$ *,etc.*) involving in sodium ions intercalation/de-intercalation. The electrolytes are used as a good ionic conductor and electronic insulator, which can be classified into three types including organic electrolytes, solid electrolytes, and aqueous electrolytes. The separator is used to prevent a short circuit but enable ions transportation between the two electrodes. The anode materials include carbonaceous materials (graphite, hard carbon, biomass-derived carbon, and graphene-based materials), insertion-type materials (Ti_2C, MoS_2, Nb_2O_5, TiO_2, V_2O_5, *etc.*) and conversion-type materials ($NiCo_2O_4$, Sb_2O_3*, etc.*).

2.1 Cathode materials

Cathode materials store energy using ions adsorption, surface redox reactions or ions intercalation. Compared to the anode materials, much fewer efforts have been paid to the research of cathode materials. Activated carbon (AC) has been widely used as cathode electrode for NICs. In addition, graphene, V_2C MXene and $Na_2Fe_2(SO_4)_3$ also have been reported as NIC cathodes.

2.1.1 **Activated carbon**

AC tends to possess abundant nanopores (2-5 nm), high surface area (up to 3000 $m^2 g^{-1}$), good electric conductivity (~60 S m^{-1}) and high stability. These features enable it be widely commercialized in the fields of energy storage,[71] air/water purification,[72] and medical uses.[73] It also has emerged as a dominating cathode material in the NIC research.[20,21,28,35,46]

As a NIC cathode, AC participating ions adsorption/de-sorption inherits a working potential of 1-4.3 V in $NaClO_4$[20,74] and $NaPF_6$[21,27] dissolved organic electrolytes versus Na^+/Na. Concluding the present research, AC cathode typically exhibits a specific capacity of about 50 mAh g^{-1} in rechargeable batteries, which is relatively low compared to that of anode materials. An AC with an improved capacity of about 60-70 mAh g^{-1} can be developed by activating the AC by strong alkali (KOH) during/after the synthesis process under high temperature. This way can create more functional groups on the surface to generate more pseudocapacitance.[75] To develop high-performance NICs, synthesizing such an AC as the cathode for NICs is expected.

2.1.2 **Graphene**

Graphene is a potential candidate for applications in energy storage field because it displays unique properties such as high electrical conductivity, flexible mechanical property, and high surface area.[76] Wang *et al.*[77] demonstrated that a three-dimensional macroporous graphene (3D MG) is a promising candidate as cathode electrode in NICs. The 3D MG was synthesized by microwave-assisted electrochemical exfoliation with a hard template method. Using this material as the cathode, disordered carbon as the anode, with a gel polymer electrolyte to assemble a quasi-solid-state NIC. As a NIC cathode, 3D MG cathode exhibited 183 F. g^{-1} at 0.4 A g^{-1} with a voltage window of 2-4.2 V. The full NIC cell achieved an energy density of 168 W h kg^{-1} at a power density of 501 W kg^{-1} with a working voltage window of 0-4.2 V, and it showed a capacity retention of 85% after 1200 cycles. This 3D MG with open structure (submicrometer sized macroporous) could obstruct dense stack and increase the electrochemical interface, thus providing more ions and electrons transport pathways to generate more pseudocapacitance.

2.1.3 **V_2CT_x MXene**

Yury Gogotsi's group reported a large family of two-dimensional (2D) materials that named "MXenes".[78,79] MXenes are chemically derived from layered $M_{n+1}AX_n$ or MAX phases, where M is an early transition-metal, A is an A-group element and X is C and/or N. MXenes exhibit good electrical conductivities (metallic conductivity) with hydrophilic surfaces (hydroxyl- or oxygen-terminated surfaces), which can accommodate a number of metal cations such as Li^+, Na^+, K^+, Ca^{2+}.[80] The MXenes generally inherit a working potential of 1-3.5 V in $NaClO_4$

and $NaPF_6$ dissolved organic electrolytes versus Na^+/Na, so they are able to be applied as both cathode and anode electrode.

Experimentally, Yohan *et al.*[40] assembled a NIC using V_2CT_x as the cathode and hard carbon as the anode, as shown in Figure 2.1. The V_2CT_x was synthesized using hydrogen fluoride (HF) to produce fluorinated and oxygenated surface functional groups, such as -OH, -O, -F and their presence were named by adding "T_x" to the chemical formula. The V_2CT_x electrode exhibited a specific capacity of 50-100 mAh g^{-1} with a working potential of 1-3.5 V, which was higher than that of AC electrode (normally ~50 mAh g^{-1}). The full NIC exhibited a capacitance of about 100 F g^{-1} with a working potential of 3.5 V. However, the cycling stability was limited to 300 cycles at 20 C, which was inferior to that of AC electrodes. The poor cycling stability was due to its ions intercalation/de-intercalation process in the V_2C accompanied by the volume changes which deteriorated the structure of the material, as shown in Figure 2.1a. Therefore, possible solutions will be required to stabilize this material when used as a cathode in NICs.

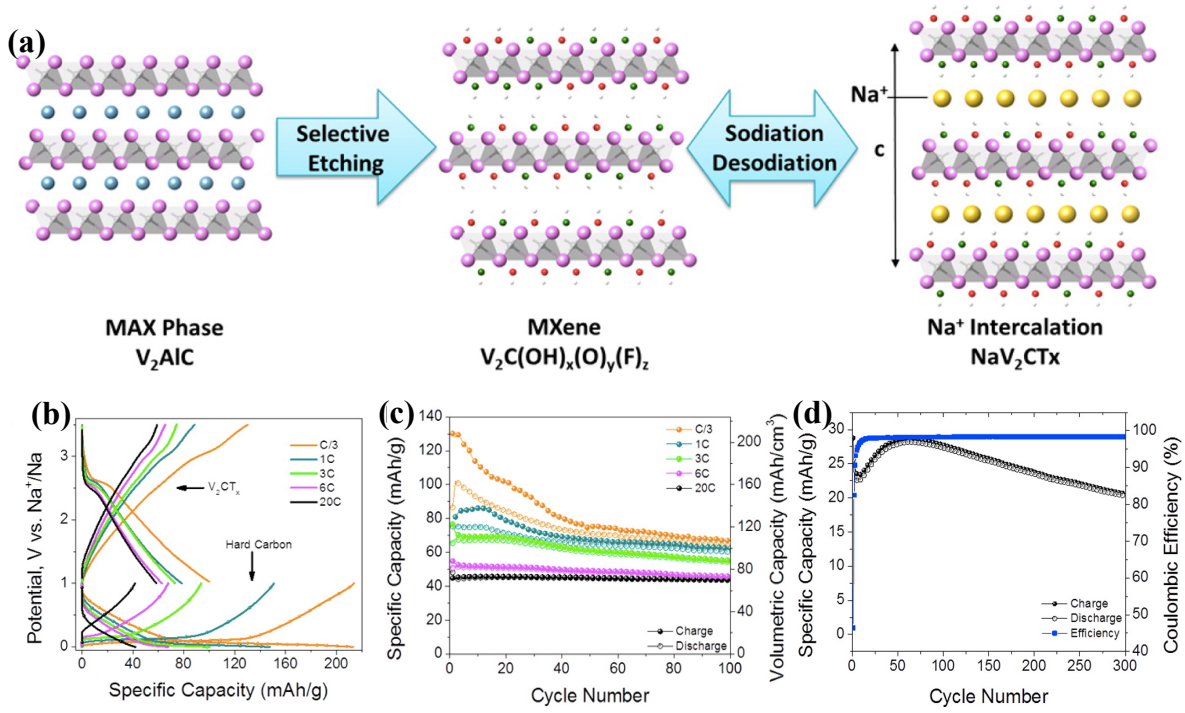

Figure 2.1 Schematic of the synthesis procedure and electrochemical performance of Mxene: (a) scheme of the synthesis of V_2CT_x and its sodium intercalation mechanism, (b) GCD profiles of V_2CT_x cathode and hard carbon anode, (c) cycling stability of V_2CT_x at

different rates in sodium half-cells, (d) cycling stability of the NIC cell (hard carbon//V_2CT_x) at a high rate (20 C).[40]

2.1.4 $Na_2Fe_2(SO_4)_3$

An iron-based sulfate, alluaudite-type $Na_2Fe_2(SO_4)_3$, is a very interesting earth-abundant sodium-ion energy storage cathode electrode, and it possesses a high operating potential of 3.8 V versus Na^+/Na in $NaClO_4$ or $NaPF_6$ dissolved carbonate-based electrolytes.[81,82] Wong *et al.*[83] demonstrated that fast sodium-ion transport kinetics occurred in the $Na_2Fe_2(SO_4)_3$ framework by density functional theory (DFT) simulations.

A NIC was assembled by $Na_2Fe_2(SO_4)_3$ as the cathode and MXene Ti_2CT_x as the anode, as shown in Figure 2.2.[74] The $Na_2Fe_2(SO_4)_3$ electrode achieved a capacity of about100 mAh g^{-1} at 1/20 C for in a sodium half-cell. The full cell NIC exhibited a capacity of 90 mAh g^{-1} (based on the weight of Ti_2CT_x) at 1.0 A g^{-1} with a voltage of 2.4 V. Other alluaudite-type compounds of $Na_{2-x}M_2(SO_4)_3$ (M = Mg, Ti, Mn, Co, Ni, and V) are promising candidates for NIC cathodes as well. Recently, Dwibedi *et al.*[84] introduced a new Mn-homologue of $Na_{2+2x}Mn_{2-x}(SO_4)_3$ which is in the alluaudite family as a sodium-ion cathode electrode. As per the DFT study, it can facilitate efficient sodium ions intercalation involving $Mn^{3+/}Mn^{2+}$ redox activity centered at 4.4 V versus. Na^+/Na. In a NIC, such a high working potential of a cathode electrode is expected to achieve high energy density, and further investigations on this alluaudite material are desired.

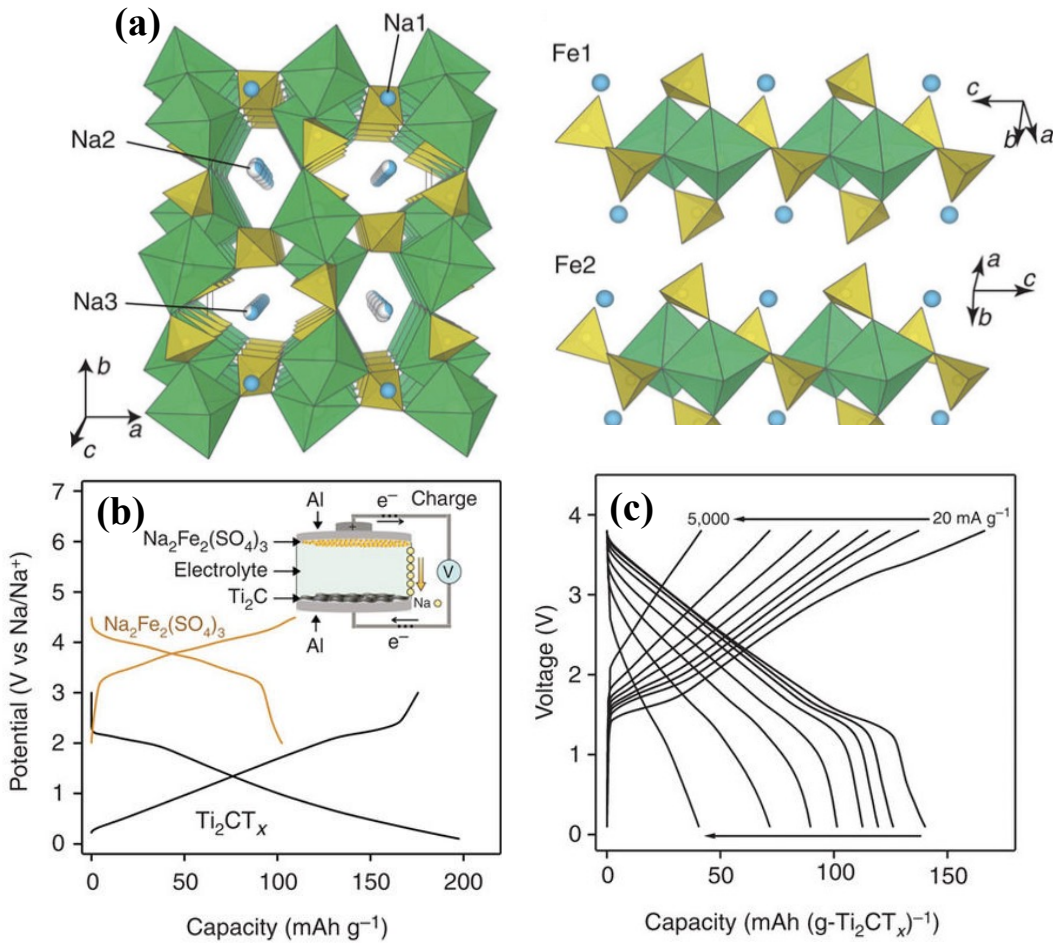

Figure 2.2 The crystal structure and its electrochemical performance of $Na_2Fe_2(SO_4)_3$: (a) crystal structure of $Na_2Fe_2(SO_4)_3$ projected along the *c* axis and local environment of two independent Fe sites. Green octahedra, yellow tetrahedra, and blue spheres show FeO_6, SO_4 and Na, respectively. Fe ions occupy two kinds of crystallographic sites that show distinctive octahedral geometries. (b) GCD profiles of V_2CT_x anode and $Na_2Fe_2(SO_4)_3$ cathode. (c) GCD profiles of the NIC cell based on the weight of Ti_2CT_x.[74]

2.1.5 $Na_{0.44}MnO_2$

$Na_{0.44}MnO_2$ is a large-sized tunnel structured orthorhombic material which can tolerate the stress from sodium intercalation/de-intercalation. It exhibited a capacity of 100-130 mAh g^{-1} with a working potential of 2-4 V in a sodium half-cell.[85] The structure of $Na_{0.44}MnO_2$ and its XRD patterns evolution at different electrochemical states are shown in Figure 2.3.[86] Clear shifts of a few diffraction lines captured in the numerous diffractograms indicated that the phases formed during biphasic transitions upon intercalation/de-intercalation into $Na_{0.44}MnO_2$ were structurally very close.

Recently, several studies demonstrated that $Na_{0.44}MnO_2$ with different morphologies such as nanofibers,[87] nanowire,[85] and rod-shaped[88] exhibited promising performance as cathode electrodes in sodium half-cells. Also, a NIC was assembled with the $Na_{0.44}MnO_2$ as the cathode and a MXene as the anode (here is $Ti_3C_2T_x$).[89] This NIC achieved a volumetric capacity of 286 mAh cm^{-3} based on the volume of $Ti_3C_2T_x$ electrode. However, the capacity decreased slightly among 60 cycles. It is expected to stabilize the structure to achieve a better cycling stability.

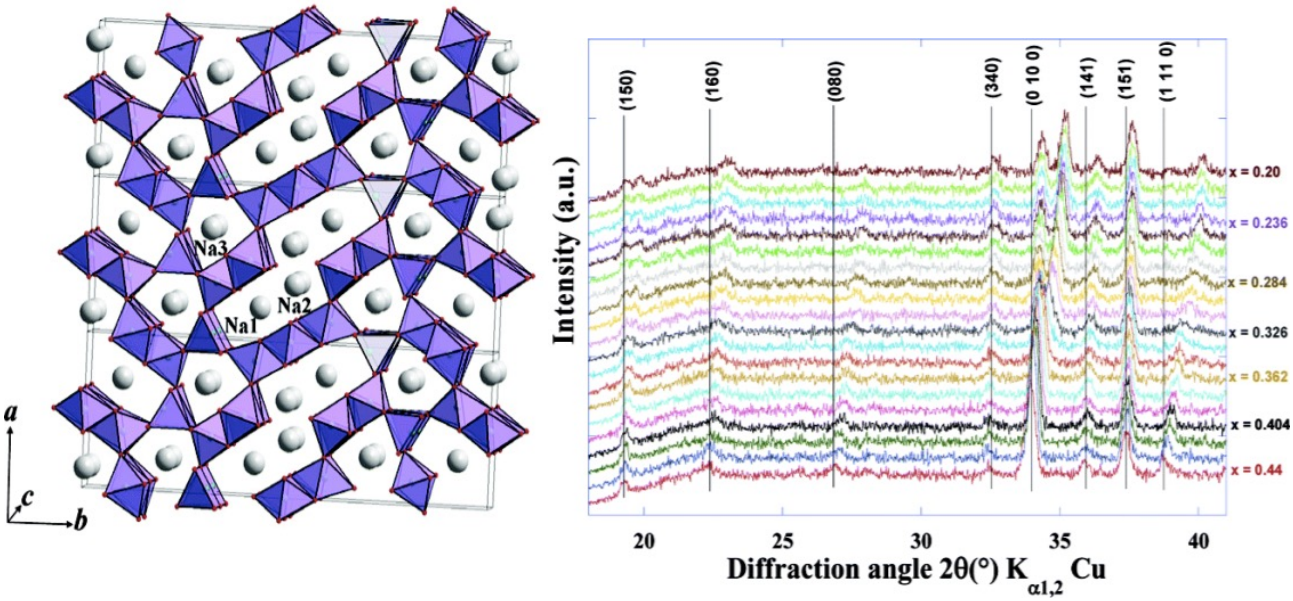

Figure 2.3 Crystal structure of $Na_{0.44}MnO_2$ (left): two sodium sites (referenced as Na1 and Na2) occupy large S-shaped tunnels, while another site (Na3) is located in the smaller tunnels. *In-situ* XRD patterns recorded at a C/250 rate (right).[86]

The study in NIC cathode materials is still in a preliminary stage. AC has been widely used as the cathode material, but its intrinsic capacity is low which effect the electrocapacitive of NICs. On the other hand, the large-tunnel cathodes including MXene, $Na_2Fe_2(SO_4)_3$ and $Na_{0.44}MnO_2$ have been explored, but the long-term cycling stability remains a concern. With the fast development of the energy storage technology, more candidates of NIC cathodes will be explored in the foreseeable future.

2.2 Electrolytes

The electrolytes for NICs have typically gained much less attention than the electrodes materials because the latter determined the energy density and power density of the system. However, the role of the electrolytes should not be neglected because they are in large percent responsible for the life time and realistically performance including practically capacity, rate capability, and safety aspects. In general, the NIC electrolytes should be chemically, electrochemically, and thermally stable with no chemical reactions or changes during the cell operation. In addition to these basic requirements, the NIC electrolytes should meet the practical criterias such as high ionically conductive, low toxicity, and low cost.[90] Electrolytes for NICs consist of sodium salts, electrolyte solvents, and additives.

2.2.1 **Sodium salts**

The choice of sodium salts should consider: (1) good solubility in the solvents to create an electrolyte with enough charge carriers; (2) good stability versus reduction as well as oxidation which possibly determine the limits of the electrochemical stability window.[90]

Comparative studies across different sodium salts in NICs are rare. For sodium-ion system electrolytes, researchers have found the same prospective anions since they have been applied in the field of lithium-ion system for many years. In NIC studies, the most popular salt is $NaClO_4$.[28–30,35,37,45,48] However, ClO_4^- is a strong oxidant and therefore has some concerns for practical applications. In addition, it is difficult to dry $NaClO_4$. Even after drying the powder at 80 °C under vacuum overnight, $NaClO_4$ usually exhibit higher water contents (>40 ppm) as compared to that of $NaPF_6$ (<10 ppm).[91] The water containing will deteriorate the electrochemical performance. $NaPF_6$ is the second most popular salt, and this salt enables the performance to compete with that of many lithium-ion systems.[19,40,74] Several salts such as $NaBF_4$, $NaCF_3SO_3$, and $Na[N(CF_3SO_2)_2]$ may emerge as strong sodium-salts in NICs, and they require more exploration in the foreseeable future.[92]

2.2.2 **Solvents**

An electrolyte solvent for NICs should meet the following standards: high dielectric constant, low viscosity for facile ion transport, dissolve sufficient sodium salts, inert to all cell components, stable, non-toxic and inexpensive.[92] Sometimes these requirements can hardly be met by an individual solvent so that it is common to use solvent mixtures. Electrolyte solvents can be classified into organic solvents, ionic liquids, polymers, and aqueous solutions.

The organic solvents applied in sodium-ion system are much the same as those used in lithium-ion system. The organic carbonates-based solvents including propylene carbonate (PC), ethylene carbonate (EC) and dimethyl-carbonate (DMC) are most popular solvents used in NICs.[35,45,75] Recently, ether-based solvents have also shown many interests. For example, Kang *et al.*[93,94] observed that graphite can reversibility store sodium ions by a combination of co-intercalation and pseudocapacitive mechanism when using ether-based solvents including diethyleneglycol dimethylether (DEGDME), tetraethylene glycol dimethyl ether (TEGDME) and dimethoxyethane (DME). Ether-based solvents could suppress electrolyte decomposition by forming a negligible solid electrolyte interface (SEI) film on the graphite surface. In contrast, thick SEI films were formed on the graphite surface in the carbonate-based solvents which block sodium ions transport. The good electrochemical performance of the graphite in ether-based electrolytes develops new avenues for the development of sodium-ion energy storage. It is foreseen that ether-based solvents will emerge as a strong candidate in the near future.

The usage of ionic liquids (ILs) as sodium solvents is at a very early stage. ILs, in general, exhibit several advantages such as a large liquidus range, thermal and electrochemical stability, and non-flammable.[95,96] A few research on ILs electrolyte were reported in the field of NIBs,[97,98,99] but very few reports were found in NICs.

Polymers exhibiting dimensional, thermal, chemical stability and flexibility, are promising solvent candidates for NICs. Polymers also show high viscosities and low dielectric constants. Therefore, separators can be exempted in the polymer-based cells. On the other hand, utilization of solid polymer solvents in sodium-ion systems can reduce safety risks without the risk of dendrite formation. The gel-polymer electrolytes, taking advantages of the

high ionic conductivity of the liquid electrolytes and the polymer flexibility, employ a variety of polymers as the scaffold to immobilize the liquid electrolytes,[100] such as poly(vinylidene fluoride) (PVDF), polyacrylonitrile (PAN), and poly(vinylidene fluoride-hexafluoropropylene) (PVDF-HFP).[101] The first gel-polymer solvent using in NIC was reported in 2015 when Wang *et al.*[77] reported a NIC consisted of a nanoporous disordered carbon as the anode and a macroporous graphene as the cathode. This NIC achieved an energy density of over 160 Wh kg^{-1} at a power density of 501 W kg^{-1} with a good cycling stability. Shortly after this report, Li *et al.*[102] introduced a quasi-solid-state NIC which was assembled with an urchin-like $Na_2Ti_3O_7$ as the anode and a peanut shell derived carbon (PSDC) as the cathode with a sodium ion conducting gel polymer as electrolyte, achieving energy densities of 111.2 Wh kg^{-1} and 33.2 Wh kg^{-1} at power densities of 800 W kg^{-1} and 11200 W kg^{-1}, respectively. The good performance indicates that the polymers-based solvents are very competitive and hold a great promise in sodium-ion energy storage.

Aqueous electrolytes exhibit outstanding characteristics such as high ionic conductivity, improved safety, low cost and environmentally benign. Zhao *et al.*[103] fabricated a NIC using a $Na_3V_2(PO_4)_3$/C as the cathode and an AC as the anode with 0.5 M Na_2SO_4 aqueous electrolyte, delivering an energy density of 10 Wh kg^{-1} at a power density of 300W kg^{-1}. Another typical aqueous-based NIC was assembled by carbon micro-spheres as the anode and a cobalt hexacyanoferrate as the cathode with 0.5 M Na_2SO_4 as an electrolyte.[104] This NIC showed an extended operating voltage window (2 V), excellent capacitance behavior, and a high energy density of 54.4 Wh kg^{-1} at a power density of 800 W kg^{-1} with a good cycling stability. The major disadvantage of water as an electrolyte solvent for NICs is its intrinsically narrow electrochemical stability window (normally below 2 V) limiting maximum cell voltage and consequently limiting the NIC's energy density.[105]

2.3 Anode materials

Anode electrodes are typically battery-type electrodes in NICs which mainly associate in ions insertion/extraction or redox reactions. According to the electrochemical mechanisms, anodes in NICs can be classified into three types: (1) carbonaceous materials such as graphite, hard carbon, biomass-derived carbon, and graphene-based materials, (2)

insertion-type materials such as Mnexe, MoS_2, Nb_2O_5, $Na_2Ti_3O_7$, TiO_2, *etc.,* (3) conversion-type materials such as $NiCo_2O_4$ and Sb_2X_3 (X=O, S).

2.3.1 **Carbonaceous materials**

Carbonaceous materials exhibit different properties in conductivity, crystallinity, chemical state and morphologies which are largely determined by their synthesis, processing, precursor and chemical treatments.[106]

2.3.1.1 Graphite

Graphite has been commercialized in lithium-ion energy storage, but it could hardly accommodate sodium ions when using carbonate-based electrolyte due to their unfavorable kinetics and larger size of sodium ions. Fortunately, Philipp *et al.*[107] reported that this problem can be solved by using co-intercalation phenomena in a diglyme-based electrolyte. Soon Kang *et al.*[93,94] revealed that graphite exhibited a reversible intercalation of sodium ions via forming a ternary graphite intercalation compounds in a diglyme-based electrolyte. Inspired by these work, Han *et al.*[108] constructed a NIC with a commercial graphitic mesocarbon microbead anode and a commercial AC as the cathode with a diglyme-based electrolyte This NIC exhibited an energy density of 86.5 Wh kg^{-1} at a power density of 2832 W kg^{-1}, and a 98% capacity retention after 3000 cycles with a voltage window of 1-4 V. The good electrochemical performance of the graphite-based carbon develops new avenues for the development of sodium-ion energy storage.

2.3.1.2 Hard carbon

Hard carbon (HC) exhibits disordered structure which is generally synthesized at high temperatures (~1000 ^oC, inert atmosphere). Acting as the same role as graphite in lithium-ion systems, these HC materials can accommodate sodium which are considered as the "first-generation" anode for sodium-ion systems.[32] Stevens *et al.*[109] proposed a simple sodium insertion model of the HC structure, as shown in Figure 2.4a. The HC exhibits random alignment of small-dimensional graphene layers with significant porosity, enabling it accommodate a number of sodium ions. Kentaro *et al.*[20] assembled a NIC using a sodium pre-doped HC as the anode and an AC as the cathode. The pre-doping process sacrificed some sodium metals to overcome the irreversible capacity during the first discharge process. In addition, it can adjust the redox potential of the HC to a value that can work properly as

an anode electrode. Figure 2.4b and c compared the electrochemical properties of the NIC with LICs in which anode electrodes were Li pre-doped HC and mesocarbon microbeads (MCMB). The lithium pre-doped HC showed better performance than that of MCMB in LICs. Moreover, the capacitance of HC-based NIC and LIC decreased by 9% and 3% respectively after 1000 cycles, suggesting that there is a room for further improvement for the applications of HC in NICs.

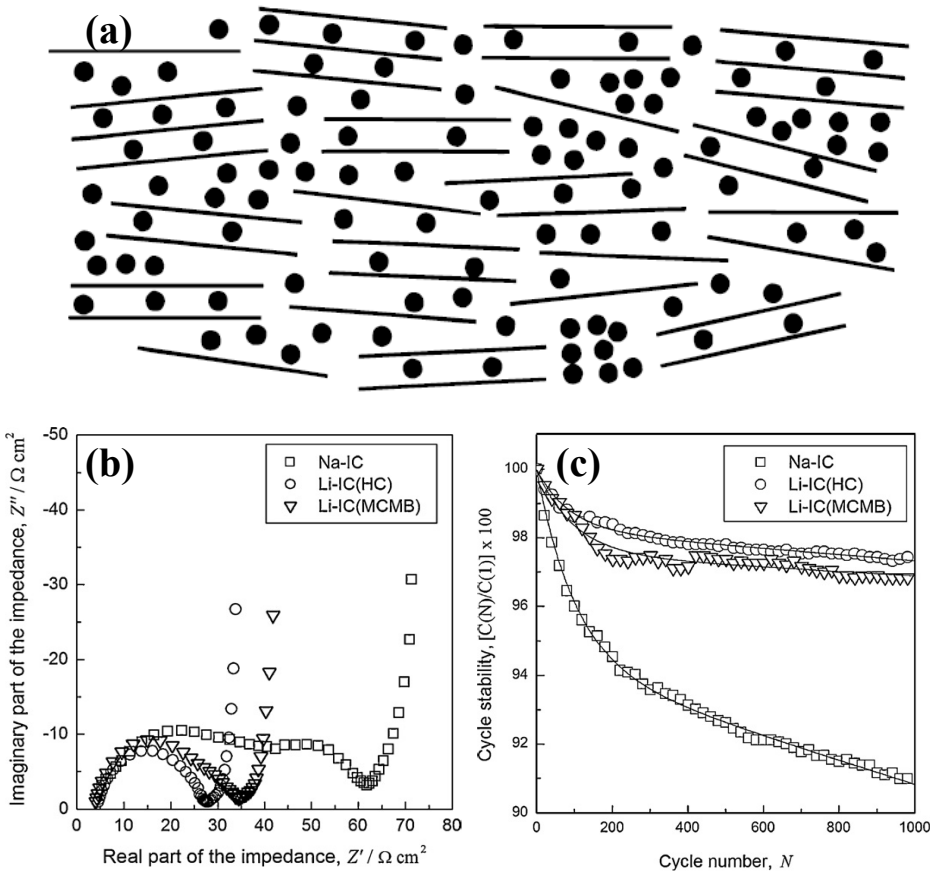

Figure 2.4 (a) Representation of model for sodium intercalates into HC. (b) Nyquist plots and (c) cycling stability of NICs and LICs.[109]

Very recently, Ding *et al.*[32] assembled a NIC with nanotube-like HC (NTHC) as the anode and activation/carbonization of polyaniline (PANI) nanotubes (APDC) as the cathode, as shown in Figure 2.5. The NTHC electrode showed a capacity of 419.5 mAh g^{-1} at 0.05 A g^{-1} in a sodium half-cell. The NIC exhibited an energy density of 133.0 Wh kg^{-1} at 2850 W kg^{-1} and remained 100.9 Wh kg^{-1} at 14,250 W kg^{-1}. In comparison with other reported energy storage devices, this NIC showed a very competitive performance.[32] Considering the

characteristics of abundant, low cost, environmental friendliness and simple manufacturing, this NTHC is a promising candidate in commercial applications.

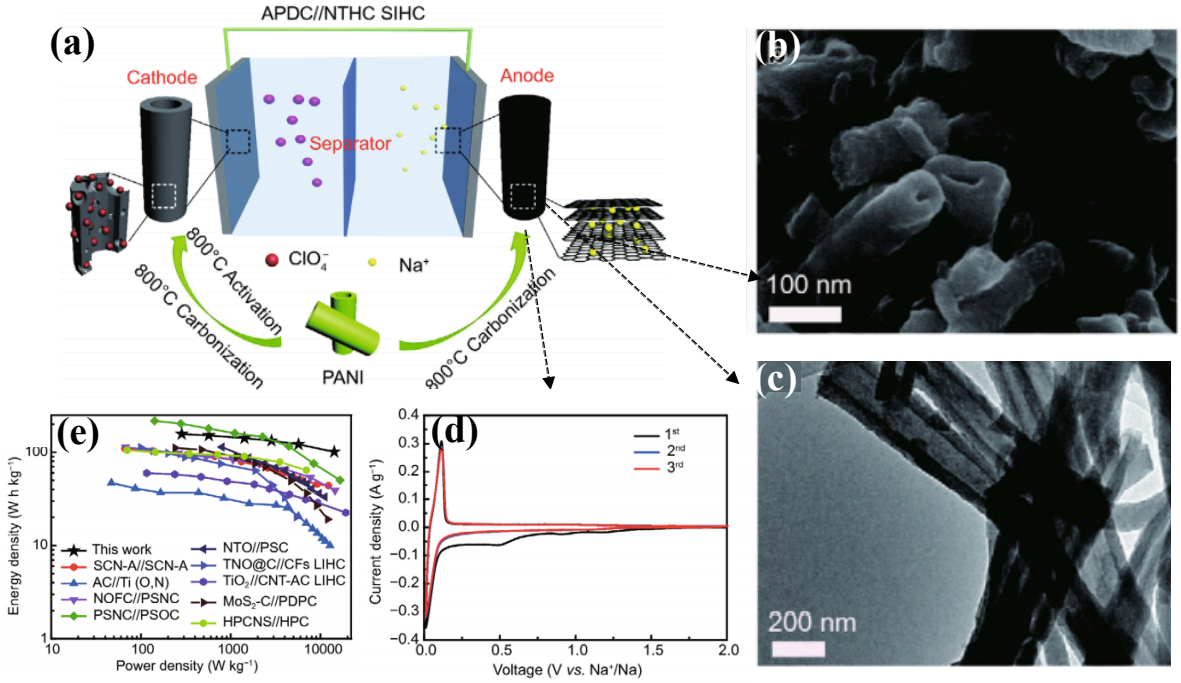

Figure 2.5 (a) Schematic of the NIC assembled with NTHC as the anode and activation/carbonization of APDC as the cathode. (b) SEM and (c) TEM images of NTHC, indicating a nanotube-like morphology. (d) CV curves of NTHC in a sodium half-cell. (e) Ragone plot of the NIC in this work, in comparison with other reported energy storage devices.[32]

2.3.1.3 Biomass-derived carbon

Biomass is a renewable energy source because it is truly green and being derived from organic waste products.[110] Peanuts have drawn interests in NICs particularly because of sufficient carbonaceous composites in their shells and skins.

Mitlin *et al.*[25] fabricated a NIC with the anode and the cathode both being derived from peanut shells, as shown in Figure 2.6. The cathode derived from peanut shell nanosheets carbon (PSNC) displayed a hierarchically porous architecture with a sheet-like morphology (Figure 2.6b), a surface area of 2396 m^2 g^{-1} and 13.51 wt.% of oxygen, while the ion intercalation anode derived from peanut shell ordered carbon (PSOC) showed a low surface

area (Figure 2.6c) with a capacity of 315 mA h g^{-1} at 3.2 A g^{-1}. The assembled NIC exhibited an energy density of 50 W h kg^{-1} at a power density of 16.5 kW kg^{-1}, and a capacity retention of 72% after 10,000 cycles with a voltage window of 1.5-3.5 V. Performance of this NIC can compete with the other energy storage devices (Figure 2.6f).

After this report, a NIC was created by the anode and the cathode both being derived from peanut skin carbons.[111] The carbons displayed a nano-scale sheet-like morphology, and a high surface area with hierarchically porous structure. In a sodium half-cell, the carbons showed a reversible capacity of 461 mA h g^{-1} at 100 mA g^{-1}. The NIC displayed energy densities of 112 and 45 Wh kg^{-1} at power densities of 67 and 12 000 W kg^{-1}, respectively. The capacitance retention of the NIC was 85% after 3000 cycles.

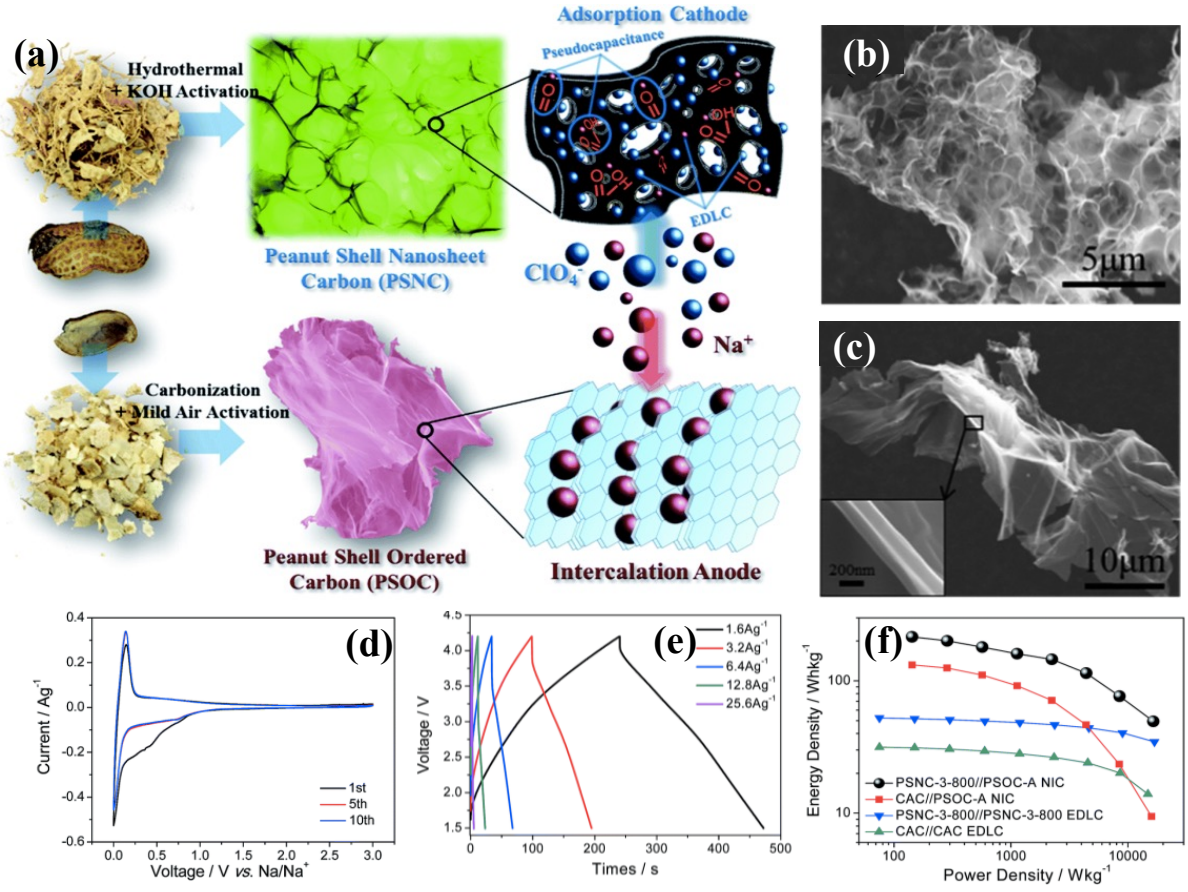

Figure 2.6 (a) Scheme of the material synthesis process employed for PSNC cathode and PSOC anode. (b) SEM of PSNC. (c) SEM of PSOC. (d) CV curves of PSOC. (e) GCD profiles of the NIC. (f) Ragone plot of the NIC in this work, in comparison with other reported energy storage devices.[25]

2.3.1.4 Graphene-based materials

The individual graphene sheets can store ions on their surfaces, edges and covalent sites,[64] has been reported as cathode electrode for NICs as briefly reviewed in the section 2.1.2. For anode application, the most popular route is to harnessing these extraordinary properties of graphene to incorporate composite materials.

Several approaches have been used to synthesize graphene, including: (1) chemical vapour deposition (CVD) growth of graphene on substrates surfaces.[112–114] (2) Mechanical exfoliation of graphite such as using adhesive tape and atomic force microscopy cantilevers.[115,116] (3) Arc-discharge synthesis of multi-layered graphene.[117] (4) Chemical exfoliation of graphite by either the Brodie, Staudenmaier, or Hummers methods to prepare graphene oxide (GO), and then reducing the GO to prepare graphene, as shown in Figure 2.7.[118] GO is a single monomolecular layer of graphite with oxygen-containing functionalities such as carbonyl, carboxyl and hydroxyl groups.[114] These groups provide active sites to form chemical bonds between cations such as (Ti^{4+}, Ni^{2+} or Fe^{3+}) to form a composite. However, the defects are generally not favorable for the electric conductivity which require to be reduced in the follow-up experiment.

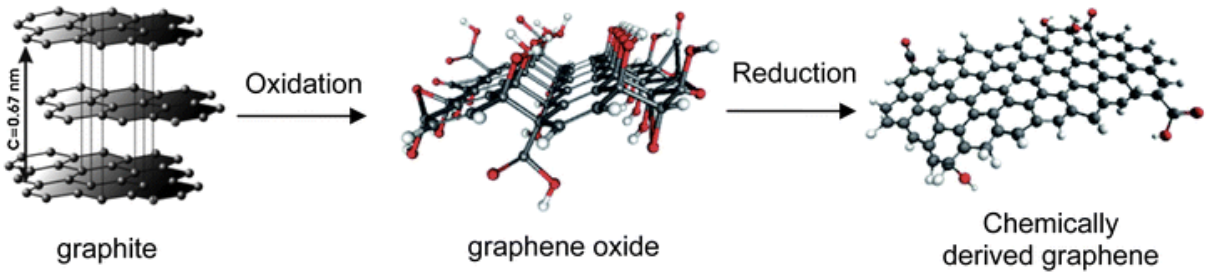

Figure 2.7 A scheme of the synthesis process for chemically derived graphene.[118]

Oxidative exfoliation of natural graphite followed by a chemical reduction has been considered as an efficient method for production of graphene for NICs. For example, Kiruthiga *et al.*[36] used a Hummers method to prepare GO, then used sodium borohydride ($NaBH_4$) to reduce it to reduced-GO (rGO). This rGO was mixed with V_2O_5 nanorods to prepare V_2O_5@rGO composite. As a result, an enhanced mass transport, electronic conductivity, and cycle stability were obtained, which is discussed in section 2.3.2.6. Shortly

after this report, the author used the similar method to prepare MoO_2@rGO and used it as an anode electrode for NIC, which showed an enhanced performance as well.[119]

Thermal reduction is also a popular method to reduce GO. For example, Lim *et al.*[28] adopted a modified Hummers method to prepare GO. Then uniformly dispersed NbO_x nanoparticles (NPs) on GO by controlling the pH values which determine the zeta potentials. The GO and NbO_x NPs attracted to form a hydrogel of NbO_x@GO through an electrostatic attraction. Finally, for the crystallization of NbO_x NPs and reduction of GO, the NbO_x@GO was heat-treated under an Argon gas at 600 ^oC to obtain a composite of Nb_2O_5@C/rGO. A NIC was assembled using this composite as the anode and an AC as the cathode, which is discussed in the section 2.3.2.3.

Hydrothermal/solvothermal reaction is another widely used method to reduce GO. For example, Lu *et al.*[120] prepared GO by a modified Hummers method. The GO was added to a mixture of $FeCl_3 \cdot 6H_2O$, dodecylamine and 2 mmol NaOH, then transferred into an autoclave and solvothermally treated in an air-flow electric oven at 200 °C for 4 days. In this process, Fe^{3+} was transformed to Fe_3O_4 and simultaneously GO was reduced to rGO. The slurry-like final product was collected and washed to obtain Fe_3O_4/rGO nanocomposites. A NIC was assembled using the synthesized Fe_3O_4/rGO nanocomposite as the anode and MnHCF as the cathode, with an aqueous electrolyte. The NIC provided an extended voltage of 1.8 V, an energy density of 27.9 Wh kg^{-1}, and a power density of 2183.5 W kg^{-1}. The good performance is because such a configuration with a graphene conductive matrix and nanoscale Fe_3O_4 particles can shorten the ion diffusion path and enable rapid electron transport through the composite material.

To summary, using graphene to incorporate composite materials as high-performance anode materials for NICs is a hot research topic, because graphene provides the merits: (1) guarantees a good electronic contact, (2) offers a large surface area to contact with the electrolyte and provides more active sites for electrochemical reaction, (3) accommodates the volume change during sodium redox reaction or intercalation/de-intercalation. Practically, however, efforts are still required to produce low-cost and high-quality graphene for the development of large-scale energy storage applications.[118]

Carbonaceous materials are popular anode materials for NICs because of their advantages of low cost, high conductivity, and long service life.[121] However, they generally suffer from low energy density because of their low volumetric mass density. Anode materials with higher specific capacities are highly desired for advancing the performance of NICs.

2.3.2 **Insertion-type materials**

Insertion-type anode materials involve the insertion process of sodium ions into the interstitial space of the host lattice during the discharging process, while the electrochemical reaction was reversed during the charging process. Several insertion-type anode materials including T_2C MXene, MoS_2, Nb_2O_5, $Na_2Ti_3O_7$, *etc.* have been proposed to construct NICs.

2.3.2.1 Ti_2C MXene

MXene material has been briefly reviewed in the section 2.1.3. Yamada *et al.*[122] demonstrated a MXene of T_2CT_x (T_x stands for surface functional groups such as –OH, -F, -O) allows sodium ions intercalation/de-intercalation into the interlayer of MXene sheets as well as capacitive storage, which may emerge as a promising anode material for sodium-ion storage. After this research, a NIC assembled with a $Na_2Fe_2(SO_4)_3$ as the cathode and a MXene Ti_2CT_x as the anode was reported.[26] The MXene Ti_2CT_x nanosheets exhibited an expansion of the interlayer distance after the first sodium ions intercalation process, then experienced invisible structural changes during subsequent cycles (as shown in Figure 2.8), enabling the full NIC deliver an energy density of 260 W h kg^{-1} at a power density of 1400 W kg^{-1} (based on the weight of Ti_2CT_x). Though the capacity retention between the 2^{nd} to 100^{th} cycles was rather high, the long cycling stability remained a concern because of its layer-restacking problem.

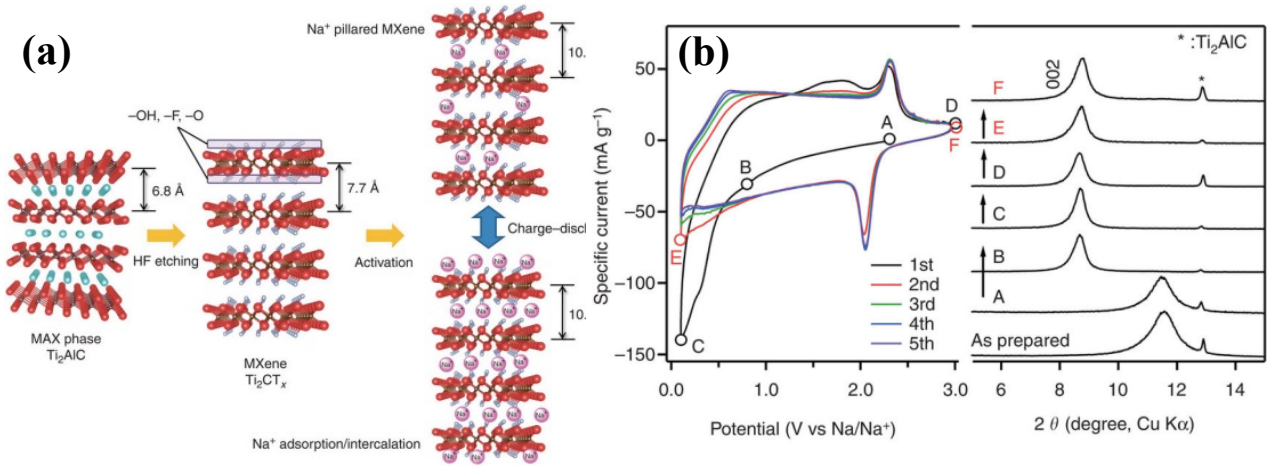

Figure 2.8 (a) Scheme of T_2CT_x preparation: the MAX phase Ti_2AlC was transformed to the MXene Ti_2CT_x nanosheets under the hydrofluoric (HF) acid treatment. (b) CV curves of Ti_2CT_x at 0.2 mV s^{-1} in a sodium half-cell and its corresponding *ex-situ* XRD patterns. Ti_2CT_x exhibited expansion of the interlayer distance after the first intercalation process, then reversibly accommodated sodium ions without significant interlayer distance change.[26]

To prevent aggregation and restacking of MXene sheets via van der Waals interactions and hydrogen bonds, in the follow-up research, Yury Gogotsi *et al.*[89] fabricated porous $Ti_3C_2T_x$ with carbon nanotubes (CNTs) films by an electrostatic attraction method. The restacking of $Ti_3C_2T_x$ nanosheets was effectively inhibited by CNTs as spacers. The composite exhibited a much higher surface area (~180 m^2 g^{-1}) than that of $Ti_3C_2T_x$ (~18 m^2 g^{-1}), which provides more active sites to contact with the electrolyte. Very recently, Dong *et al.*[123] reported the transformation of accordion-like Ti_3C_2 MXene into nanoribbons of sodium titanate ($NaTi_{1.5}O_{8.3}$, M-NTO) and potassium titanate ($K_2Ti_4O_9$, M-KTO) through an oxidation and alkalization process (as shown in Figure 2.9). The resulting M-NTO exhibited enhanced ion kinetics with a large capacity of 191 mAh g^{-1} at 200 mA g^{-1} in sodium-ion storage, higher than that of pristine Ti_3C_2 (178 mAh g^{-1}) and commercial TiC derivatives (86 mAh g^{-1}). Notably, M-KTO displayed a capacity of 151 mAh g^{-1} at 50 mA g^{-1} and long-term stable cyclability over 900 times. The good performance is due to their suitable interlayer spacing, narrow widths of nanoribbons and open macroporous structures. The synthesis approach is flexible. Even though these MXene-derived materials have not been tested in NICs, the good performance in sodium half-cells indicates that they hold a great promising as potential candidates as anodes in NICs, which deserve further exploration in future.

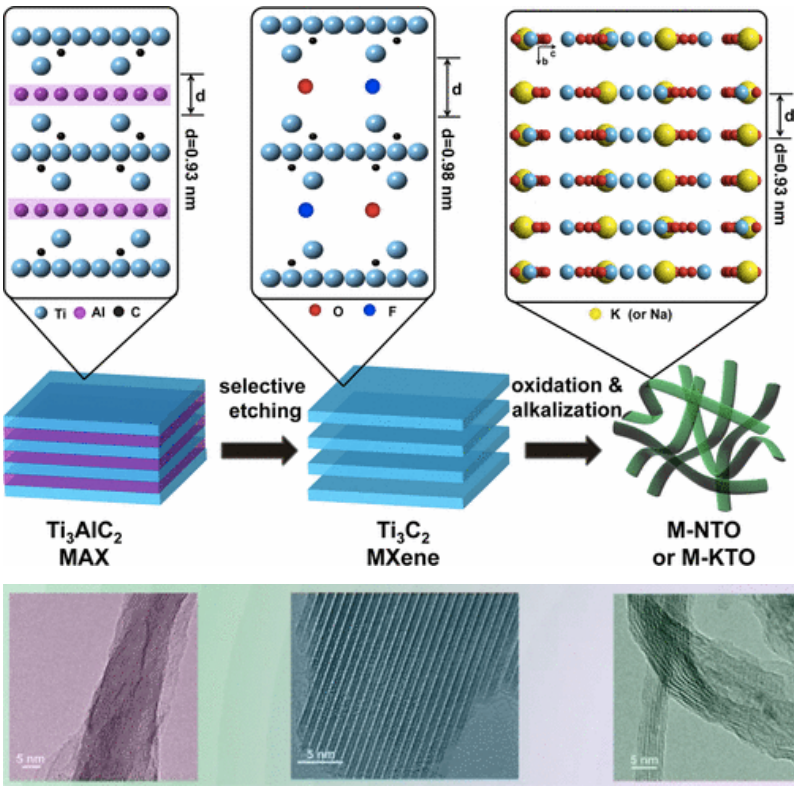

Figure 2.9 Schematic of the synthesis approach for M-NTO or M-KTO nanoribbons. Ti_3C_2 MXene was firstly prepared *via* selectively etching Al of Ti_3AlC_2 MAX phase in HF. Then, Ti_3C_2 MXene was hydrothermally treated with NaOH or KOH solution in H_2O_2 to produce M-NTO or M-KTO nanoribbons.[123]

2.3.2.2 Molybdenum disulfide

Molybdenum disulfide (MoS_2) is a typical layered structure with 2D atomic that has emerged as an electrode material for sodium-ion energy storage. Its 2D layered structure provides slit-shaped channels to accommodate ion intercalation/de-intercalation.[124] However, the easily-crack structure, the unstable SEI layer and the poor conductivity of MoS_2 hinder its practical application in sodium-ion storage. Thus, Wang *et al.*[23] have turned to compose graphene (G) sheets with MoS_2 to fabricate three-dimensional (3D) architectures. The addition of graphene contributed to an expanded d-spacing between MoS_2, fast electrons and ions transport. As expected, this MoS_2/G composite exhibited a capacity of about 350 mAh g^{-1} after 200 cycles at 0.25 C in a sodium half-cell. A NIC was assembled using this MoS_2/G composite as both anode and cathode. This NIC displayed a capacitance of 50 F g^{-1} after 2000 cycles at 1.5 C with a voltage window of 0.1–2.5 V.

Very recently, Wang *et al.*[33] synthesized a MoS_2–carbon (MoS_2–C) monolayer with an interoverlapped structure *via* an interface-modification route. This structure was demonstrated to have a wide voltage range of 0.4–3.0 V versus Na^+/Na, exhibiting an improved cyclability, as shown in Figure 2.10. A NIC was assembled using MoS_2–C as the anode and a homemade polyaniline derived porous carbon (PDPC) as the cathode. This NIC exhibited a high energy density of 111.4 Wh kg^{-1} and a high power density exceeding 12 000 W kg^{-1} with a voltage window up to 3.8 V.

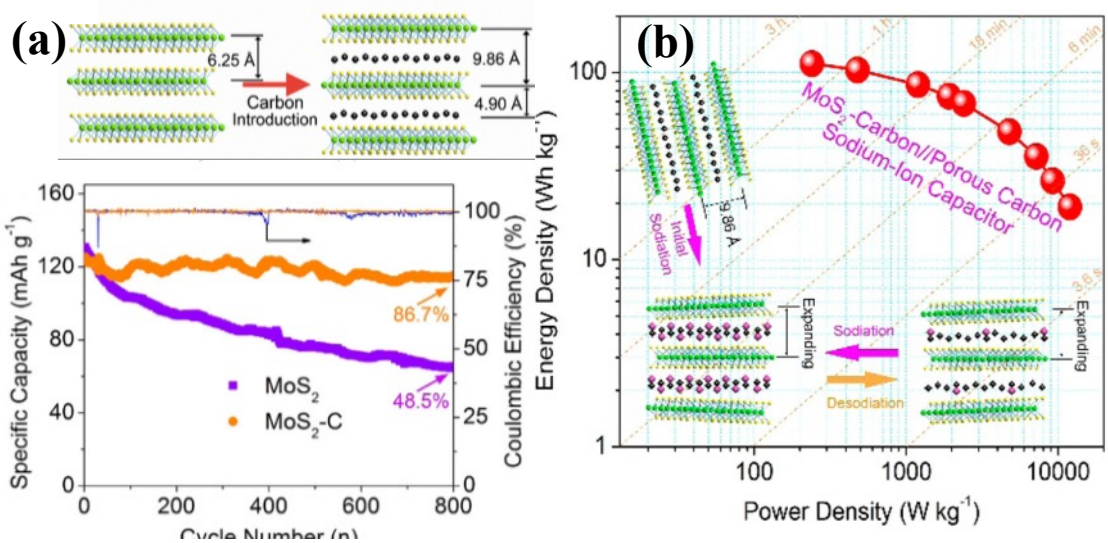

Figure 2.10 (a) Schematic illustration of structures of layered MoS_2 (left) and MoS_2–C (right), and the corresponding cycling performance in a sodium half-cell. (b) Schematic illustration of the reaction mechanism of MoS_2–C by electrochemical activation and Ragone plots of the NIC assembled using a MoS_2–C as the anode and a PDPC as the cathode.[33]

2.3.2.3 Niobium pentoxide

Niobium pentoxide (Nb_2O_5) shows the characteristics of low cost, environmentally benign and stable in a wide range of temperature, which is a promising electrode material in sodium-ion energy storage. Kong *et al.*[125] revealed that T-Nb_2O_5 exhibited fast insertion kinetics for lithium ions via pseudocapacitive reaction combined with an intercalation reaction as well. However, Nb_2O_5 generally exhibits a low electrical conductivity (≈3×10^{-6} S cm^{-1}) which hinders its application in sodium-ion energy storage. To improve the conductivity, Kang *et al.*[126] fabricated an ordered-mesoporous Nb_2O_5 with carbon composite (Nb_2O_5@C). In a sodium half-cell, the composite exhibited a capacity of 175 mAh g^{-1} at 0.5 A g^{-1}. Shortly after

this study, the same group[28] fabricated a Nb_2O_5@C/rGO to further enhance its capacity and rate performance, as shown in Figure 2.11. This composite exhibited an improved capacity (285 mAh g^{-1} at 0.025 A g^{-1}), a good rate performance (110 mAh g^{-1} at 3 A g^{-1}) and a capacitive charge contribution of 46% in a sodium half-cell. A NIC was fabricated using Nb_2O_5@C/rGO as the anode and a commercial AC as the cathode, exhibiting both high energy density (76 W h kg^{-1}) and high power density (20 800 W kg^{-1}) with a superior cycling performance at 1 A g^{-1} among 3000 cycles. In comparison with other reported NICs, this NIC showed a very competitive performance.

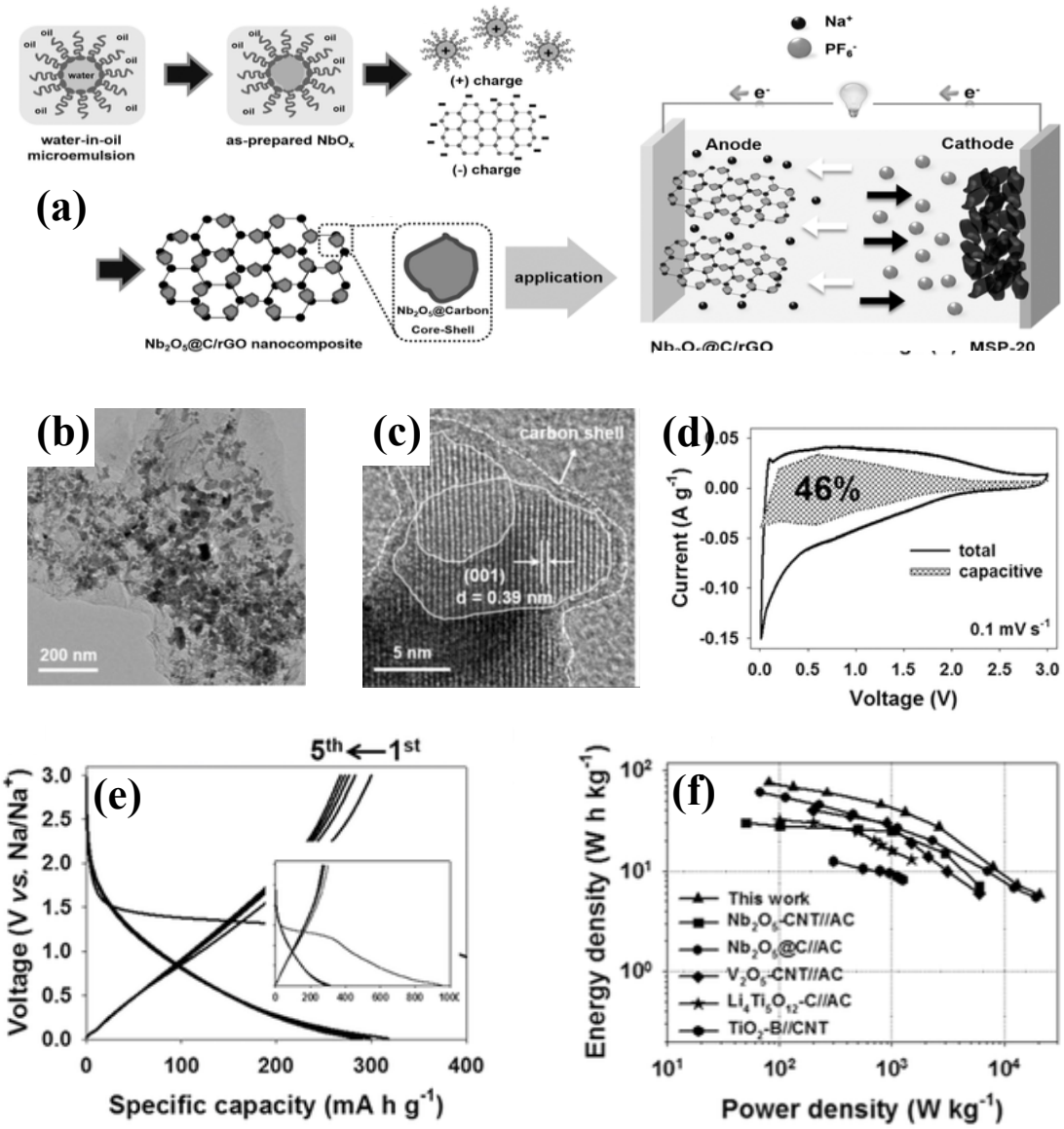

Figure 2.11 (a) Schematic illustration of the synthesis procedure for Nb_2O_5@C/rGO nanocomposites and a NIC assembled with this Nb_2O_5@C/rGO as the anode and an AC as

the cathode. TEM images of (b) Nb_2O_5@C/rGO and (c) Nb_2O_5@C. (d) CV curves of Nb_2O_5@C/rGO-50 with separation between total current and surface capacitive current (shaded regions) at 0.1 mV s^{-1}. (e) GCD profiles of Nb_2O_5@C/rGO-50 at 0.025 A g^{-1} in a sodium half-cell. (f) Ragone plots of the NIC in this work, in comparison with the performance of other NICs.[28]

Followed these research, Hongsen Li *et al.*[29] constructed a NIC using self-assembled Nb_2O_5 nanosheets as the anode and a peanut shell derived carbon as the cathode. A capacitive charge contribution of about 77% was achieved in this Nb_2O_5 anode. The resulting NIC delivered an energy density of 43.2 Wh kg^{-1} and a high power density of 5760 W kg^{-1} with a capacity retention of 80% at 1280 mA g^{-1} after 3000 cycles. Because of the pseudocapacitive nature, the Nb_2O_5-based NICs exhibited high power density and long cycling stability, holding a great promising for large-scale energy storage applications.

2.3.2.4 Sodium titanate and its derivative

Alkali titanates with the general formula of $A_2Ti_nO_{2n+1}$ (A= alkali metals; $2 \leq n \leq 9$), generally exhibit high ionic exchange ability and high sodium ions conductivity.[127] A typical alkali titanate of layered sodium titanate ($Na_2Ti_3O_7$) is capable of reversibly accommodate two sodiums per $Na_2Ti_3O_7$ with a low voltage of about 0.3 V, appearing as an appealing anode electrode in a NIC.[128] Yin *et al.*[21] prepared $Na_2Ti_3O_7$ nanotubes and used them as the anode, coupled with an AC as the cathode to assemble a NIC. This NIC exhibited an energy density of 34 Wh kg^{-1} at a power density of 889 W kg^{-1}. However, its cycling retention was only about 55% among 1000 cycles. To enhance the kinetics of sodium intercalation and de-intercalation of $Na_2Ti_3O_7$, Dong *et al.*[27] developed an approach to in-situ grow $Na_2Ti_3O_7$ on 1D CNTs. Due to the unique nanostructure with high electrical conductivity and distinct pseudocapacitive behaviors, the $Na_2Ti_3O_7$@CNT electrode exhibited an enhanced rate performance and cycle stability. A NIC was assembled using this $Na_2Ti_3O_7$@CNT as the anode and a carbon derived from peanut shell as the cathode. This NIC exhibited a higher energy and power densities (58.8 Wh kg^{-1} and 3000 W kg^{-1}, respectively) and a higher capacity retention of 75% at 0.4 A g^{-1} among 4000 cycles.

Shortly after this study, Dong *et al.*[30] used a simple hydrothermal process followed by an annealing treatment to grow flexible $Na_2Ti_3O_7$ (NTO) nanosheets onto carbon textiles with

robust adhesion, as shown in Figure 2.12. Using this flexible electrode as the anode combined with graphene film (GF) as the cathode, they fabricated a NIC that achieved an energy density of 55 Wh kg^{-1}, a power density of 3000 W kg^{-1}, and a capacity retention of 80.3% at 0.5 A g^{-1} among 2500 cycles. Particularly, the flexible NIC exhibited a stable electrochemical performance with about 100% capacitance retention under harsh mechanical deformation.

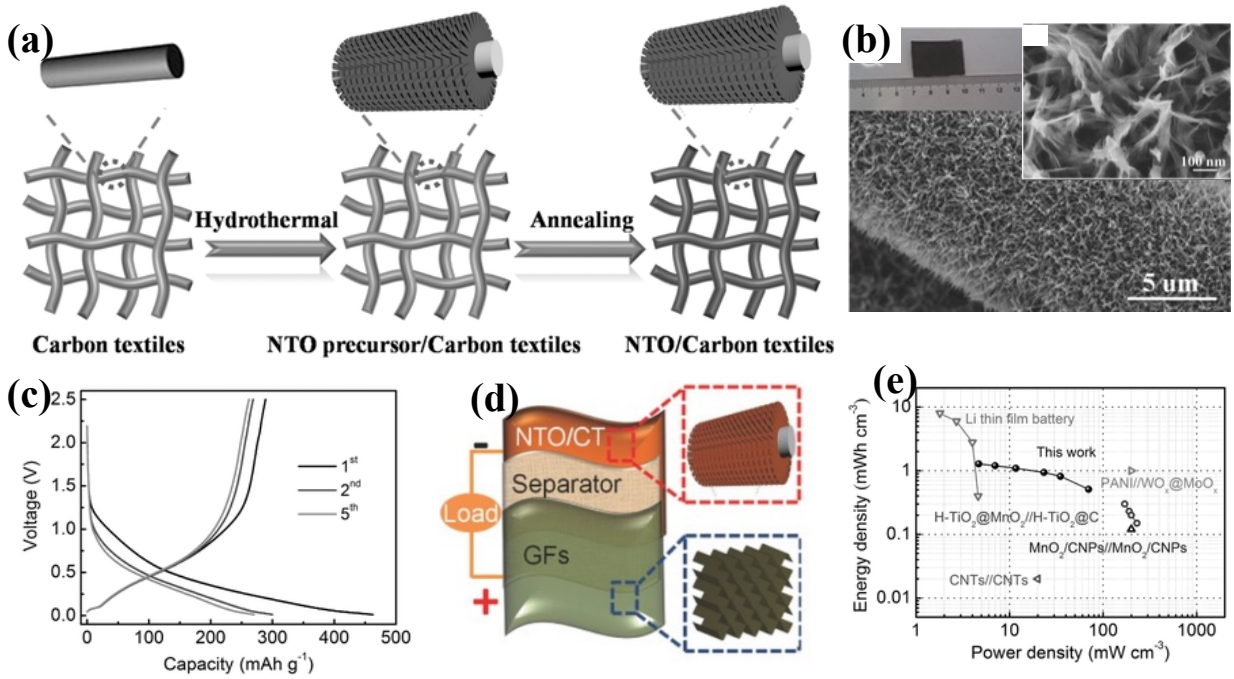

Figure 2.12 (a) Schematic illustration of the synthesis procedure for NTO/Carbon textiles. (b) SEM of NTO/Carbon textiles. (c) GCD profiles of NTO/Carbon textiles in a sodium half-cell at 100 mA g^{-1}. (d) Schematic illustration of the flexible NIC device assembled with the NTO/CT as the anode and GF as the cathode. (e) Ragone plot of the NIC in this work, in comparison with the performance of other flexible devices.[30]

$Na_2Ti_2O_4(OH)_2$, being one of the $Na_2Ti_3O_7$ derivatives, exhibits the distorted TiO_6 octahedral layers with each Ti^{4+} surrounded by an octahedron of six O_2^- ions separated by sodium ions layers.[129] A NIC was fabricated with a $Na_2Ti_2O_4(OH)_2$ as the anode and a chemically activated rice husk derived porous carbon as the cathode. This NIC exhibited a stable electrochemical performance with an energy density of about 65 Wh kg^{-1} at a power density of 500 W kg^{-1} with a working voltage of 0-4 V.

2.3.2.5 Titanium dioxide

Titanium dioxide (TiO_2) is a promising insertion-type pseudocapacitance anode for NIBs due to its excellent intrinsic safety, low volume variations (less than 4%), and low working potential of about 0.7 V versus Na/Na^+.[130] However, the anatase TiO_2 exhibits poor electron mobility (~10^{-12} S cm^{-1}) and low wettability which restrict its electrochemical properties.[131] To overcome these deficiencies, Liu *et al.*[31] fabricated a nitrogen-doped anatase TiO_2 nanospheres (~100 nm) (N-TiO_2) as the anode, using an AC as the cathode to assemble a NIC. This N-TiO_2 showed a remarkable rate capacity (162 mAh g^{-1} and 136 mAh g^{-1} at 1 A g^{-1} and 20 A g^{-1}, respectively), and long-term cycling stability. The NIC displayed high energy density and power density (~80.3 Wh kg^{-1} and ~12500 W kg^{-1}, respectively) and a good cycling stability after 6500 cycles.

Apart from the heteroatom doping, introducing highly conductive carbons such as graphene[35] and carbon nanotubes (CNTs)[132] is an efficient way to improve the electrochemical properties. Le *et al*.[35] reported a composite of mesoporous single-crystal-like TiO_2 particles anchoring on graphene sheets (MWTOG) as an anode material for NICs, as shown in Figure 2.13. The MWTOG exhibited good pseudocapacitive charge storage performance with high reversibility, fast kinetics, and negligible degradation to the micro/nanostructure. As a result, it delivered a capacity of 268 mAh g^{-1} at 0.2 C and remained 126 mAh g^{-1} at 10 C after 18 000 cycles. A NIC was assembled with this MWTOG as the anode and a commercial AC as the cathode, exhibiting energy densities of 64.2 Wh kg^{-1} and 25.8 Wh kg^{-1} at power densities of 56.3 W kg^{-1} and 1357 W kg^{-1}, respectively. Remarkably, a high capacity retention of 90% was achieved after 10 000 cycles.

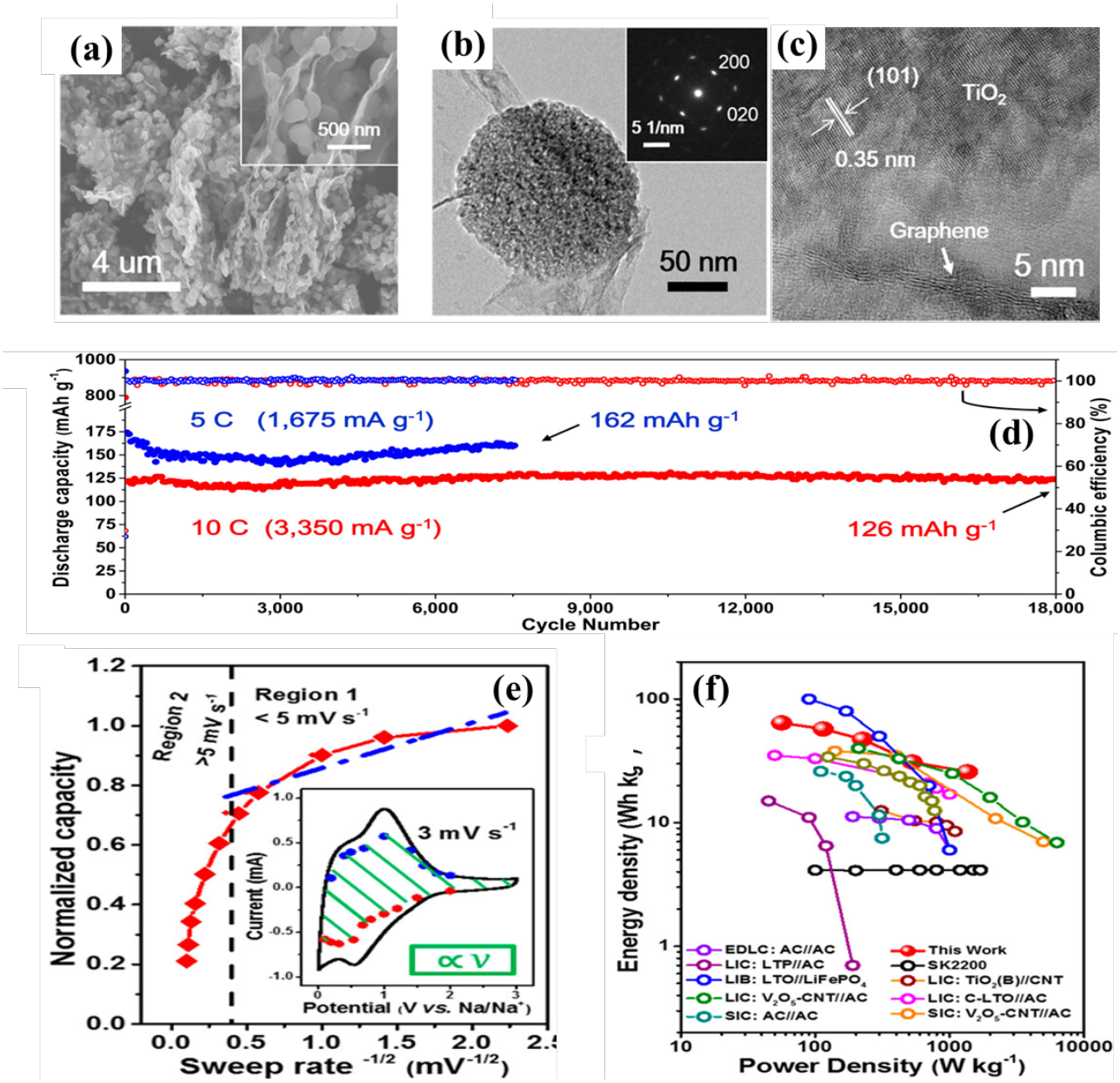

Figure 2.13 SEM (a) and TEM (b, c) of MWTOG, and inset of b shows the SAED pattern of TiO_2. (d) Cycling stability of MWTOG electrode at 5 C and 10 C versus Na^+/Na. (e) Plot of capacity *versus* $v^{-1/2}$ to separate diffusion-controlled and capacitive-controlled contributions. and inset represented that the capacitive process has accounted for 73% of the stored charge at 3 mV s^{-1}. (f) Ragone plot of the NIC in this work, in comparison with the performance of other representative energy storage devices.[35]

Very recently, Zhu *et al.*[45] prepared TiO_2@CNT@C nanorods through a signal-nozzle electrospinning technique followed by a heat treatment. The ion and electron transport kinetics of TiO_2@CNT@C could be improved due to the addition of multi-walled CNT. As a

result, TiO_2@CNT@C exhibited excellent cyclic stability and outstanding rate capability in sodium half-cell. A NIC was assembled using TiO_2@CNT@C nanorods as the anode and biomass-derived carbon with high surface area as the cathode, delivering a high energy density of 81.2 Wh kg^{-1} and a high power density of 12 400 W kg^{-1} within 1.0–4.0 V. Meanwhile, the capacity retention was 85.3% after 5000 cycles tested at 1 A g^{-1}.

2.3.2.6 Vanadium pentoxide

Vanadium pentoxide (V_2O_5) exhibits a layered crystalline structure with open channels for facile sodium ions intercalation and de-intercalation by adjusting its layer spacing.[133] However, its poor electronic conductivity and slow ion diffusion restrict its development. To enhance the electronic conductivity and wettability, Chen *et al.*[19] synthesized interpenetrating porous networks consisting of layer-structured V_2O_5 nanowires and CNTs, which was denoted as V_2O_5/CNT, as shown in Figure 2.14. The interconnected pore channels ensured facile ions transport and the conductive CNT network facilitated electrons transport. As expected, this V_2O_5/CNT exhibited a fast pseudocapacitive charge storage process, which seemingly avoided phase transformations during ion insertion/extraction, contributing to an enhanced service life time. A NIC was fabricated using the V_2O_5/CNTs nanocomposite as the anode and a commercial AC as the cathode, delivering an energy density of 38 Wh kg^{-1} at a power density of 140 W kg^{-1}, which was comparable to that of other prototype supercapacitors.

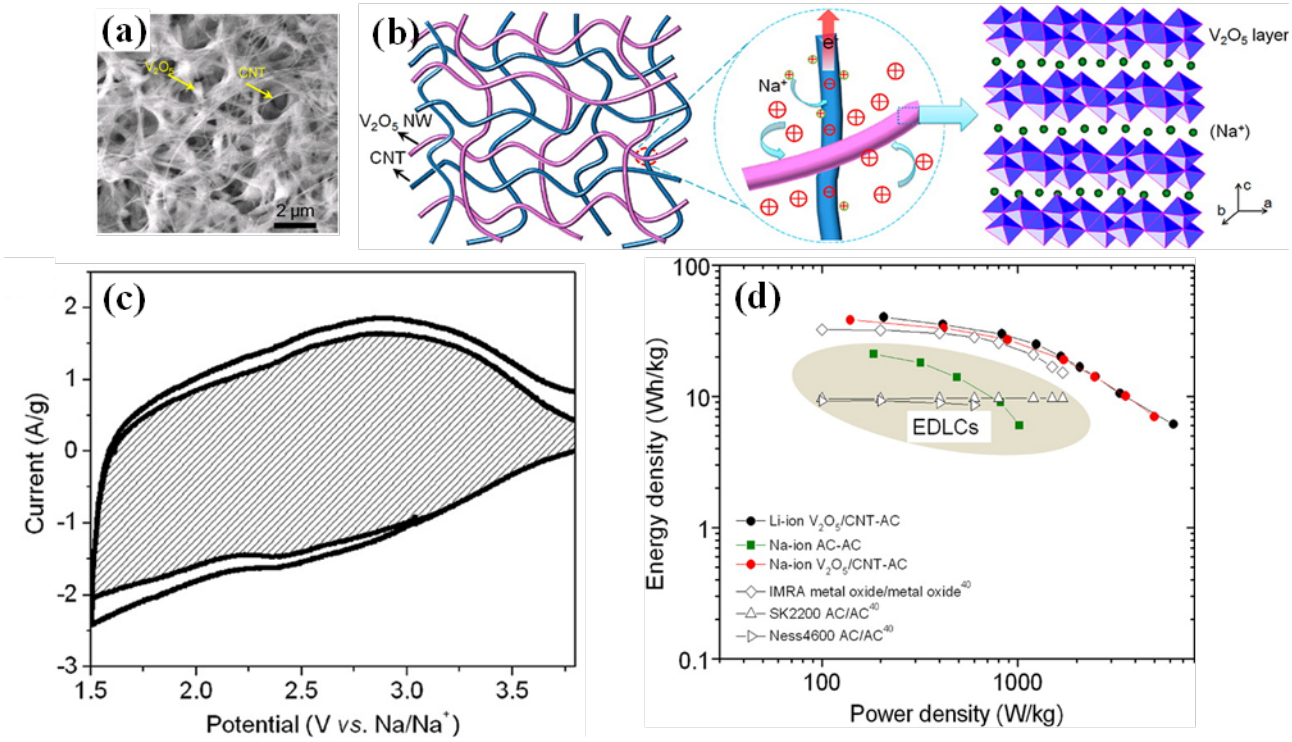

Figure 2.14 (a) SEM image of V_2O_5/CNT. (b) Schematic of a nanocomposite consisting of interpenetrating networks of V_2O_5 nanowires and CNTs. (c)The CV curves at a scan rate of 10 mV s^{-1}. The shaded region represented the capacitive current contribution, which accounted for 82% of the total measured current. (d) Ragone plot of the NIC in this work, in comparison with the performance of other prototype supercapacitors.[19]

Very recently, Kiruthiga *et al.*[36] anchored V_2O_5 nanorods onto rGO (V_2O_5@rGO). The rGO inside served as a backbone to combine V_2O_5 and enhanced its electrical conductivity and chemical stability. A fast faradic charge-storage process exhibited during the insertion and extraction of sodium ions in V_2O_5@rGO. A NIC was assembled using this V_2O_5@rGO as the anode and a honey derived AC as the cathode, delivering an energy density of about 65 Wh kg^{-1} at a power density of about 72 W kg^{-1}. The capacity retention was 85% after 1000 cycles at 0.01 A g^{-1}.

2.3.2.7 $NaTi_2(PO_4)_3$

Sodium super ionic conductor of $NaTi_2(PO_4)_3$ (NTP) exhibits a 3D framework consisting of the corner and edge-connected [PO_4] tetrahedral and [TiO_6] octahedral, and it inherits a theoretical capacity of 133 mAh g^{-1} in sodium-ion energy storage.[134] However, the

application of NTP is hindered by the low capacity release and the poor cycle stability owing to its low electronic conductivity.[135] To overcome this problem, Roh *et al.*[37] designed a NTP/rGO microsphere composite as an anode material for sodium-ion energy storage. This composite showed a superior rate capability of 93 mAh g^{-1} at 50 C and a capacity retention of 98% after 200 cycles at 10 C. A NIC constructed with a NTP/rGO microsphere composite as the anode and an AC as the cathode delivered energy densities of 53 Wh kg^{-1} and 31 Wh kg^{-1} at power densities of 330 W kg^{-1} and 6700 kW kg^{-1} respectively in the voltage window of 0 V-2.7 V.

Simultaneously, Wei *et al.*[136] described a solvothermal method to prepare quasi-cubic mesoporous NTP nanocages which are consisted of many nanocrystals with a mutual growth orientation, forming a uniform cube-like structure filling with 3D quasi-cubic nanopores. The tiny nanostructures and abundant pores provided sufficient active sites and shortened the ion transport path to ensure fast ions transport kinetics. As a result, the as-obtained NTP nanocages showed a reversible capacity of 120 mAh g^{-1} at 0.2 C in sodium half-cell, with a capacity retention of 74% after 10 000 cycles at 5 C, and high rate capability of 97 mAh g^{-1} at 10 C. A NIC was assembled with the NTP nanocages as the anode and an AC as the cathode. Such a NIC achieved a capacity of 42.8 mAh g^{-1} with a maximum energy density of 56 Wh kg^{-1} in the voltage window of 0-2.5 V. However, as an anode material for NICs, the NTP inherited a relatively high voltage of 2.0 V versus Na^+/Na, restricting the working potential of the full NIC. The narrow working potential window may cause a practical low energy density which hinders the practical application.

2.3.2.8 Other insertion-type materials

The insertion-type materials including Na_2CoSiO_4, Na_2MnSiO_4, P2-$Na_{0.67}Al_xCo_{1-x}O_2$ ($0.0 \leq x \leq 0.5$) and cobalt hexacyanoferrate (CoHCF) were also reported for anode electrodes in NICs using aqueous-based electrolytes. For example, a NIC was fabricated using a Na_2CoSiO_4 as the anode, an AC as the cathode, and an aqueous electrolyte, exhibiting a capacitance of 42 F g^{-1} and an energy density of 12.4 Wh kg^{-1} at a power density of 782.7 W kg^{-1}. The capacitance retention was 84% after 1500 cycles.[137] Similarly, Na_2MnSiO_4 showed satisfying performance as an anode electrode in aqueous-based NICs.[138]

P2-$Na_{0.67}Al_xCo_{1-x}O_2$ ($0.0 \leq x \leq 0.5$) is a material that substituted Al^{3+} entered into the Co^{3+} and showed a layered P2 structure with space group $P6_3/mmc$.[139] The sodium ions

de/intercalation occurred in P2-$Na_{0.67}Al_xCo_{1-x}O_2$ accompanied by Co^{3+}/Co^{4+} transformation. The electrodes exhibited typical pseudo-capacitance behaviors in an aqueous electrolyte. The specific capacitance of $Na_{0.67}Al_{0.3}Co_{0.7}O_2$ was 260 F g^{-1} at 1 A g^{-1} with a capacitance retention of 80.1% after 5000 cycles, demonstrating to be a promising electrode material for NICs.

CoHCF, known as Prussian blue analogues with a general chemical formula of $A_xPR(CN)_6$, possesses a host framework with large interstitial space.[104] Lu *et al*.[104] used a CoHCF as the anode to assemble a NIC by pairing it with a carbon micro-spheres cathode with an aqueous electrolyte, showing an extended operating voltage window (2 V) with an energy density of 54.4 Wh kg^{-1} at a power density of 800 W kg^{-1}.

2.3.3 **Conversion-type materials**

Conversion-type materials generally experience a solid-state redox reaction during sodiation/de-sodiation, in which the crystalline structure experience a change, accompanied by the breaking and recombining chemical bonds.[140] Two types of conversion-type materials including $NiCo_2O_4$ and Sb_2X_3 (X=O, S) have been proposed to construct NICs.

2.3.3.1 Nickel cobaltite

Nickel cobaltite ($NiCo_2O_4$), a ternary metal oxide with two different metal cations, tends to exhibit better electrical conductivity and higher electrochemical activity than nickel oxides or cobalt oxides.[141] Additionally, the low cost, abundance and environmentally benign nature of $NiCo_2O_4$ (NCO) makes it a promising electrode material in energy storage.[141–146] In 2002, the first report on NCO used in NIBs suggested that this material can induce conversion reactions and achieve a capacity close to 200 mAh g^{-1} at 0.1 C rate, much lower than its theoretical capacity can reach to 890 mAh g^{-1}.[51] Later, a 3D hierarchical porous nanostructure with carbon fiber cloth-supported NCO nanowire arrays was designed.[145] The introduction of carbon fabric cloth significantly improved the capacity retention of $NiCo_2O_4$ nanowire arrays from 16.7% to 82% after 50 cycles. In 2013, spinel NCO was investigated as the anode for NIBs and NICs.[22] This NCO electrode delivered a capacity of 236 mAh g^{-1} at the 2nd cycle, and it faded to 57 mAh g^{-1} at the 30th cycle at a current density of 100 mA g^{-1}. A NIC was fabricated using this NCO as the anode and an AC as the cathode. An energy density of 13.8 Wh kg^{-1} at a power density of 308 W kg^{-1} was obtained. To further increase

the electrochemical properties including energy density and power density, improvements in the design of NCO are highly desired.

2.3.3.2 Antimony-based materials

Recently, antimony-based materials such as Sb_2O_3,[147] Sb_2O_4,[148] Sb_2S_3,[149] and Sb alloy[150] have aroused interests as the anode electrodes in sodium-ion energy storage because of their high theoretical capacities. For examples, Sb_2O_3 and Sb_2S_3 possess high theoretical capacities of 1109 and 946 mAh g^{-1}, respectively.[38] However, antimony-based materials often suffer from poor electric conductivity and large volume change during repeated cycles, leading to an inferior rate performance and poor cycling stability. To solve these problems, Liu *et al.*[38] fabricated Sb_2X_3 (X=O, S) onto a carbon fiber cloth (CFC) substrate, which was denoted as Sb_2X_3/CFC. The CFC not only provided rapid transport of electrons but also supported Sb_2X_3 with strong synergistic effect with excellent mechanical performance. The electrokinetics study indicated that the sodium-ion storage mechanism in Sb_2X_3/CFC involved in a combination of surface capacitive contribution and diffusion-controlled insertion process. As a result, a NIC was fabricated using Sb_2S_3/CFC and Sb_2O_3/CFC as the anodes and flexible carbon fibers as the cathode, respectively delivering energy densities of 124 Wh kg^{-1} and 117 Wh kg^{-1} at a power density of 580 W kg^{-1}. The capacity retention was about 90% after 4000 cycles in the voltage window of 1.5 V- 4.3 V.

2.4 Summary and perspectives

Although the development of NICs is still in the initial stages, the NICs indeed hold a great potential in the field of energy storage because of their characteristics of low cost, competitive electrochemical performance, and environmentally friendly. Several attempts have focused on searching for high-performance cathodes and anodes materials. Here, the following aspects are proposed regarding the development of NICs:

1 AC has been widely used as the cathode material because of its high surface area, good electric conductivity and high stability. The large-tunnel cathodes including MXene, $Na_2Fe_2(SO_4)_3$ and $Na_{0.44}MnO_2$ have been also explored as cathode materials in NICs, but their long-term cycling stability remains a concern.

2 The role of electrolytes is important because they largely determine the life time and realistically performance in terms of practical capacity, rate capability and safety aspects. Solid electrolytes are currently under the spotlight as the solution to the safety issue of NICs.

3 The conversion-type anodes such as $NiCo_2O_4$ and Sb_2X_3 (X=O, S) with rich electroactive sites stand out for their low cost, abundance in nature, and high theoretical specific capacities. They are emerging and developing as high-performance anodes materials in sodium-ion energy storage.

4 Integrating the electrode materials with conductive substances such as carbon, graphene and conductive polymer is an effective approach to improve the electric and ionic conductivities for high electrochemical properties.

Chapter 3 Research methodology

This chapter describes the chemicals, the experimental methods and technical measurements used in this thesis project. Specifically, materials characterization including X-ray diffraction analysis, scanning electron microscope, transmission electron microscope, nitrogen and argon adsorption/desorption isotherms, X-ray photoelectron spectroscopy spectra, thermal gravimetric analysis are described. Electrochemical measurement techniques such as galvanostatic charge and discharge test, cyclic voltammetry curves and the electrochemical impedance spectroscopy tests are described.

3.1 Chemical reagents and materials

Table 3.1 lists the chemicals and reagents for the synthesis of electrode materials. All chemicals were used without further purification.

Table 3.1 Chemicals and reagents used to prepare electrode materials.

Name	Company	Purity or grade
Graphite flakes	Sigma-Aldrich	AR
Sodium nitrate ($NaNO_3$)	Merck	AR
Potassium permanganate ($KMnO_4$)	Merck	AR
Hydroxide peroxide (H_2O_2)	Merck	30%
Hydrochloric acid (HCl)	Merck	37%
Sulphuric acid (H_2SO_4)	Merck	98%
Cobalt nitrate hexahydrate ($Co(NO_3)_2{\cdot}6H_2O$)	Sigma-Aldrich	98%
Nickel nitrate hexahydrate ($Ni(NO_3)_2{\cdot}6H_2O$)	Sigma-Aldrich	99.9%
Urea (CH_4N_2O)	Chem-supply	AR
Glycerol ($C_3H_8O_3$)	Chem-supply	AR

Isopropanol (C_3H_8O)	Sigma-Aldrich	99.5%
Ethylenediamine ($C_2H_8N_2$)	Alfa Aesar	99%
Sodium hydroxide (NaOH)	Sigma-Aldrich	97%
Poly(diallyldimethylammonium chloride ($(C_8H1_6ClN)_n$)	Sigma-Aldrich	20%
Hydrochloric acid (HCl)	Merck	37%
Ammonia solution ($NH_3 \cdot H_2O$)	Emsure	28-30%
Nickel (II) sulfate hexahydrate ($NiSO_4 \cdot 6H_2O$)	Sigma-Aldrich	98%
Hexamethylenetetramine ($C_6H_{12}N_4$)	Sigma-Aldrich	99%
Iron (II) sulfate heptahydrate ($FeSO_4 \cdot 7H_2O$)	Sigma-Aldrich	99%

Anode materials synthesis are described in the following chapters for details.

3.2 Materials characterization

X-ray diffraction (XRD) analysis was performed to measure various structures of materials such as phases composition and grain size. Electron microscopes including field-emission scanning electron microscope (FESEM) and transmission electron microscope (TEM) were used for morphology characterization. Nitrogen and argon adsorption/desorption isotherms were applied to characterize surface area and pore structures of materials. X-ray photoelectron spectroscopy (XPS) spectra were used to measure the elemental composition, chemical state, empirical formula, and electronic state of the elements in a material. Thermal gravimetric analysis (TGA) was performed to measure the mass of a sample/ component as the temperature changes. The equipment and measurements details are described in the following chapters.

3.3 Electrochemical measurements

The electrolyte preparation, the coin cell assemblies and disassembles are described in the following chapters. The galvanostatic charge and discharge (GCD) tests of the sodium half-

cells were performed on a Neware battery tester (CT3008). The cyclic voltammetry (CV) curves and the electrochemical impedance spectroscopy (EIS) tests were recorded with an electrochemical work station (CHI-600D). The capacitive performance of the NIC cells was characterized using the CV and GCD techniques on an Autolab PGSTAT302N workstation.

3.3.1 **Galvanostatic charge and discharge**

GCD is a standard technique to test the performance of capacitors. The potential was recorded by applying a constant current between the cells. The specific capacitance of the cell can be deduced from the discharge curve of GCD, as has been given in the equations (1-1) to (1-3) in Chapter 1.

3.3.2 **Cyclic voltammetry**

CV is a commonly used method for studying dynamic electrochemistry. By applying a potential difference between the cells, the electrode is scanned at a given rate potential while the current is recorded. The average specific capacitance (*C*, in F g^{-1}) for this cell can be calculated integrated from a CV curve, which is:

$$C = \frac{q}{2mV} = \frac{1}{2mV}\int_{V_-}^{V_+} i(v)dV \qquad (3\text{-}1)$$

where *q* (in C) is the total charge, integrating the positive and the negative sweeps in a CV curve, *m* is the mass of the electrode (in g), *V* is the scan rate (in V s^{-1}), and V_+-V_- is the potential window (in V).

3.3.3 **Electrochemical impedance spectroscopy**

EIS is a non-destructive method to distinguish the contribution of each component in an electrochemical cell. The EIS is usually employed at a sine wave with a defined frequency (0.01-10 000 Hz) and small amplitude (5-10 mV). A curve of EIS data is to plot *Z′* against -*Z″* to obtain a Nyquist plot. Impedance *Z* is a complex number, which can be calculated by:

$$Z(w)=Z'(w)+jZ''(w) \qquad (3\text{-}2)$$

where $w=2\pi f$, f is the frequency (in Hz), Z' and Z'' are the real and imaginary parts of impedance, respectively.

3.3.4 **Ragone plot**

Ragone plot provides the values of specific energy versus specific power. The plot was named after David V. Ragone[151] Energy density and power density are the amount of energy and power stored in the energy storage device per volume or mass, respectively. Based on the overall specific capacitance (C, in F g^{-1}) of a two-electrode device, the maximum energy density (E_{max}, in J g^{-1} stored) and power (P_{max}, in W g^{-1}) density delivered for the storage energy device are calculated by:

$$E_{max} = \frac{1}{2}\mathrm{CV}^2 \quad (3\text{-}3)$$

$$P_{max} = \frac{\mathrm{V}^2}{4R_s} \quad (3\text{-}4)$$

where V is the operating voltage (in V), which is determined by the thermodynamic stability of the electrolyte and the electrodes. R_s is the equivalent serious resistance (in ohm). According to the equations of (3-3) and (3-4), a large capacitance, a wide operating voltage, and a minimum resistance are preferred to achieve high energy and power density.

The below equations (3-5 and 3-6) were usually used to calculate the practical energy density (E, in Wh kg^{-1}) and power density (P, in W kg^{-1}):

$$E = \frac{0.5\ CV^2}{3.6} \quad (3\text{-}5)$$

$$P = \frac{3600\ E}{t} \quad (3\text{-}6)$$

where C is the specific capacitance (in F g^{-1}), V is the operating voltage (in V), and t is the discharge time (in s).

Chapter 4 Sodium-ion storage performance of thermally treated $NiCo_2O_4$ spheres

Nickel cobaltites (**$NiCo_2O_4$**) spheres were synthesized using a solvothermal method followed by a thermal treatment at three different temperatures, namely 250, 350 and 450 ^oC. The as-prepared $NiCo_2O_4$ spheres were comprised of interconnected nanoparticles whose crystal structure and electrochemical properties were greatly influenced by the thermal treatment temperature. The $NiCo_2O_4$ sample treated at 350 ^oC showed an optimal performance as the anode in sodium-ion batteries and sodium-ion capacitors.

4.1 Introduction

Lithium-ion storage including lithium-ion batteries (LIBs) and lithium-ion capacitors (LICs) have achieved great success in the past decade as an efficient energy storage system, and are still being pursued for powering portable electronics and electric vehicles.[18,65,152] However, the geographical location and limitation of lithium resources will raise the cost of lithium in the near future. Therefore, energy storage based on sustainable and economically feasible resources is desired. In this regard, sodium-ion storage including sodium-ion batteries (NIBs) and sodium-ion capacitors (NICs) are considered as appealing alternatives because of sodium's abundance in the earth's crust and low cost of sodium precursors.[153,154] However, graphite, the anode material that has been used in lithium-ion storage is generally not suitable for sodium-ion storage because of the large atomic radius and high ionization energy of sodium.[8,155] Therefore, alternative anode materials for reversibly storing sodium ions must be developed. A number of anode materials such as oxides,[51,156–158] sulfides,[159–162] alloy,[163–166] carbons[110,167,168] and organic compounds,[169,170] have been investigated as candidates for sodium-ion storage. Oxides materials, especially transition-metal oxides,[171] seem to be the most promising anodes. In this regard, nickel cobaltite ($NiCo_2O_4$), a ternary

metal oxide with two different metal cations, has been shown to display a better electrochemical activity than that of nickel oxides or cobalt oxides,[141] and subsequent studies[141–146] have indeed confirmed $NiCo_2O_4$ (NCO) is a very promising electrode material for energy storage.

According to Alcántara *et al.*[51] the theoretical specific capacity of NCO could reach 890 mAh g^{-1}. However, previous experimental results showed that the practical capacity and cycling stability of NCO were low. For examples, Lee *et al.*[53] synthesized NCO nanoneedle array electrode for NIBs. This material delivered a specific capacity of 236 mAh g^{-1} at the 2nd cycle, which shows a capacity of 215 mAh g^{-1} after 50 cycles at the current rate of 50 mA g^{-1}. Ding *et al.*[22] prepared a spinel NCO as an anode, exhibiting a specific capacity of 57 mAh g^{-1} at the 30th cycle in NIB owing to the severe volume change upon cycling. A NIC assembled with this spinel NCO as the anode and a commercial activated carbon (AC) as the cathode exhibited a poor electrochemical performance with an energy density of 13.8 Wh kg^{-1} at a power density of 308 W kg^{-1}.

In this chapter, NCO spheres were synthesized using a solvothermal method followed by a thermal treatment. It was found that the thermal treatment temperature played an important role in determining the crystal structure and particle size of the NCO. The sample thermally treated at 350 ^{o}C exhibited an optimal cycling stability and rate capability in NIBs, which is due to perfect crystallization and optimal particle size. A NIC assembled using this sample as the anode and a commercial AC as the cathode delivered an energy density of 33.75 Wh kg^{-1} at a power density of 900 W kg^{-1}, with a cycling retention of 70.3 % at 3 A g^{-1} after 1000 cycles.

4.2 Experimental section

4.2.1 **Materials synthesis**

A spherical NCO was prepared *via* a solvothermal route and a subsequent thermal treatment under different temperatures in air. In a typical synthesis, 6 mmol of $Co(NO_3)_2.6H_2O$ and 3 mmol of $Ni(NO_3)_2.6H_2O$ were dissolved in 45 mL of isopropanol and 9 mL of glycerol. After stirring for 20 min, the mixture was transferred to a Teflon-lined stainless steel autoclave and heated at 180 ^{o}C for 6 h. After the reaction mixture cooling to room temperature, the

solid product was collected by centrifugation and washed with distilled water and ethanol several times and dried in an oven at 80 ^{o}C. The intermediate solid was subsequently thermally treated at 250 ^{o}C, 350 ^{o}C, and 450 ^{o}C in air for 2 h, respectively, with a heating rate of 2 ^{o}C min^{-1}. Samples thus obtained were labeled as NCO-250^{o}C, NCO-350^{o}C and NCO-450^{o}C, respectively.

4.2.2 **Materials characterization**

XRD patterns were collected on a Bruker D8 X-ray diffractometer with Ni-filtered Cu Kα radiation (λ = 1.54056 Å, 40 kV, 30 mA) at a scan rate of 2º min^{-1}. FESEM (JEOL 7100) and TEM (F20Tecnai 20) were used to characterize the morphology of samples. Nitrogen adsorption/desorption isotherms were measured on a Tristar II 3020 (Quantachrome) at the liquid nitrogen temperature. The specific surface areas of the samples were calculated using the Brunauer-Emmett-Teller (BET) method from the nitrogen adsorption isotherms. TGA was conducted in air from room temperature up to 550 ^{o}C at a heating rate of 5 ^{o}C min^{-1} using a Perkin-Elmer STA 6000.

4.2.3 **Electrochemical measurements**

The electrodes were prepared by mixing 70 wt.% of active materials, 20 wt.% of an electrical conductor (carbon black), and 10 wt.% of a binder (carboxymethyl cellulose, CMC) in de-ionized water to form a slurry, which were subsequently coated on a copper current collector for NCO slurry and an aluminium foil current collector for the AC (a specific surface area of 1200 m^2 g^{-1} provided by AC Technologies Pty Ltd, Australia) slurry. After the electrodes were dried at 60 ^{o}C overnight in a vacuum oven, they were punched into circular discs and assembled in a 2032-type coin cell with GF/C glass fibre (Whatman, USA) as the separator and 1 M $NaClO_4$ dissolved in a mixture of propylene carbonate (PC) and ethylene carbonate (EC) (volume ratio: 1:1) plus 2 vol. % fluorinated ethylene carbonate (FEC, provided by HSC Corporation) as the electrolyte. The electrolyte preparation, the coin cell assemblies and disassembles were performed in an Argon filled glovebox.

Sodium half-cells were assembled by using the above-prepared electrodes with sodium metal plates as the reference electrodes. A full NIC cell was fabricated with the NCO electrode as the anode and a commercial AC (a specific area of 1200 m^2 g^{-1} from AC

Technologies Pty Ltd, Australia) as the cathode. Before assembling the full cell, The NCO electrode was pre-cycled 3 times at 0.1 A g^{-1} in a sodium half-cell and then sodiated to 0.005 V versus Na^+/Na. The mass ratio of the cathode over the anode was 3.0.

4.3 Results and discussion

Figure 4.1a shows the XRD pattern of the as-prepared intermediate product. According to the literature,[141,172] the XRD pattern shows a characteristic of metal alkoxides. To assess the follow-up thermal treatment process of the as-prepared intermediate product, a TGA measurement was performed. Figure 4.1b shows the TGA curve of the as-prepared intermediate product. Two obvious weight-loss events were observed. The first weight loss event below 230 ^oC with about 23% weight loss can be attributed to the removal of physically adsorbed water and gases. The second region from 230 ^oC to 250 ^oC showed a significant weight loss of about 29%, which is due to the decomposition of the intermediate product to form NCO. To explore an optimal thermal treatment temperature for maximizing electrochemical performance, the intermediate product was then thermally treated at 250 ^oC, 350 ^oC, and 450 ^oC in air for 2 h.

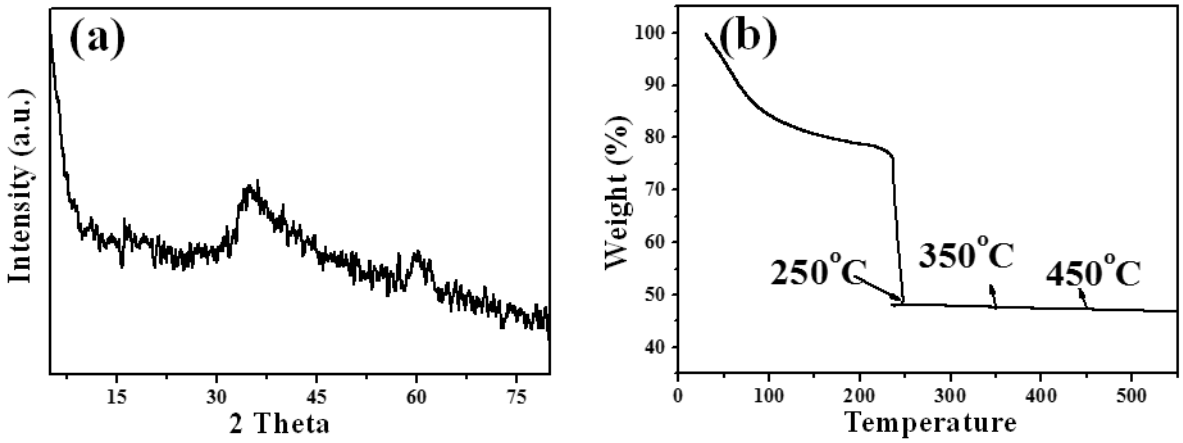

Figure 4.1 (a) XRD pattern and (b) TGA curve of the as-prepared intermediate product.

Figure 4.2 shows the XRD patterns of the NCO samples synthesized by thermally treating the intermediate product at 250 ^oC, 350 ^oC, and 450 ^oC. In NCO-250^oC sample, the peaks of (311), (400), and (440) can be indexed to the cubic spinel structure, NCO (JCPDS 73-

1702). However, the absence of (111), (511) and (220) peaks indicated that the intermediate product has not completely transformed into NCO at 250 ^{o}C. The samples treated at 350 ^{o}C and 450 ^{o}C presented a series of characteristic peaks which match well with the NCO spinel phase. While rising the treatment temperature from 350 ^{o}C to 450 ^{o}C, the diffraction peaks of NCO gradually sharpened, which indicates an increase of crystallinity. By using the Scherrer's formula based on the (311) peak, the grain size of NCO was calculated to be 9.4 nm, 11.2 nm, 14.8 nm for 250 ^{o}C, 350 ^{o}C, and 450 ^{o}C, respectively. Notably, at the thermal treatment temperature above 250 ^{o}C, an impurity phase, namely cubic NiO appeared as evidenced by the presence of the two peaks at 43.1^{o} and 64.0^{o} two theta, which can be indexed to NiO (JCPDS 78-0643). According to previous studies,[142,173,174] the formation of NiO is due to partial decomposition of spinel NCO. The presence of NiO phase may influence the performance of the NCO electrode. To verify its influence, a spherical NiO sample was synthesized and tested as an anode for NIBs (the experimental details and characterizations are provided in the supplement data 4.5). Figure S4.1 shows the XRD pattern and SEM image of the NiO sample. All diffraction peaks in Figure S4.1a can be indexed to a crystal phase of NiO (JCPDS 78-0643).

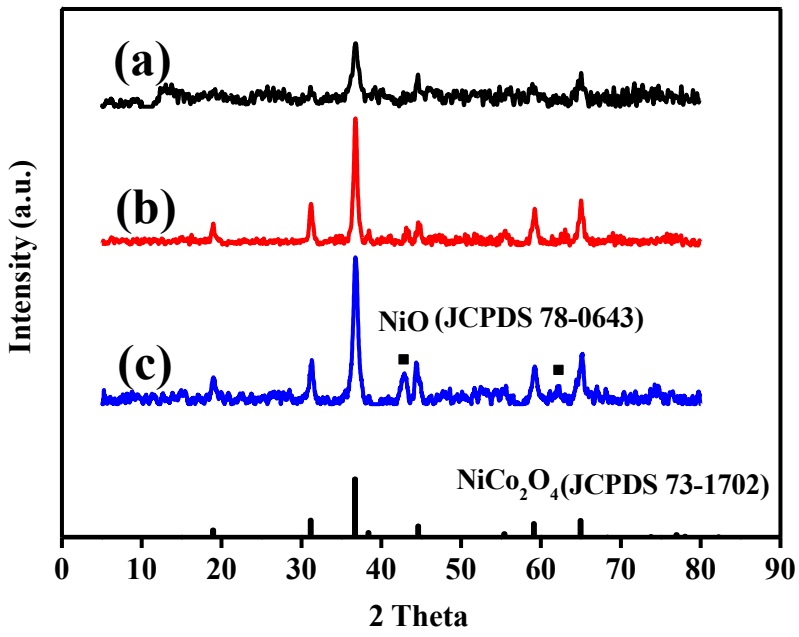

Figure 4.2 XRD patterns of (a) NCO-250^{o}C, (b) NCO-350^{o}C and (c) NCO-450^{o}C.

Figure S4.2 shows the FESEM images of the intermediate product. From Figure S4.2a, this sample shows spherical morphology with diameter varied from 0.2 to 1.8 um. Upon higher

resolution magnifications (Figure S4.2b), the sphere was assembled by many layered flakes. Figure 4.3 shows the FESEM images of the NCO samples obtained at different temperatures. After thermal treatment, the overall morphology of the particles has been well preserved as spheres, as can be seen in Figures 4.3a, c, and e. However, differences in the morphology can be clearly observed from the high-magnification images (Figures 4.3b, d and f). Treating at 250 ^{o}C did not lead to a complete crystallization of the intermediate product, therefore producing spheres which were assembled by many irregularly shaped particles. The samples treated at 350 ^{o}C and 450 ^{o}C comprised well-defined nanoparticles with clear edges because of good crystallization. With the increase in treatment temperature from 350 to 450 ^{o}C, the grain size of nanoparticles increased (Figures 4.3d and f), due to further crystallization, which is consistent with the XRD analysis above.

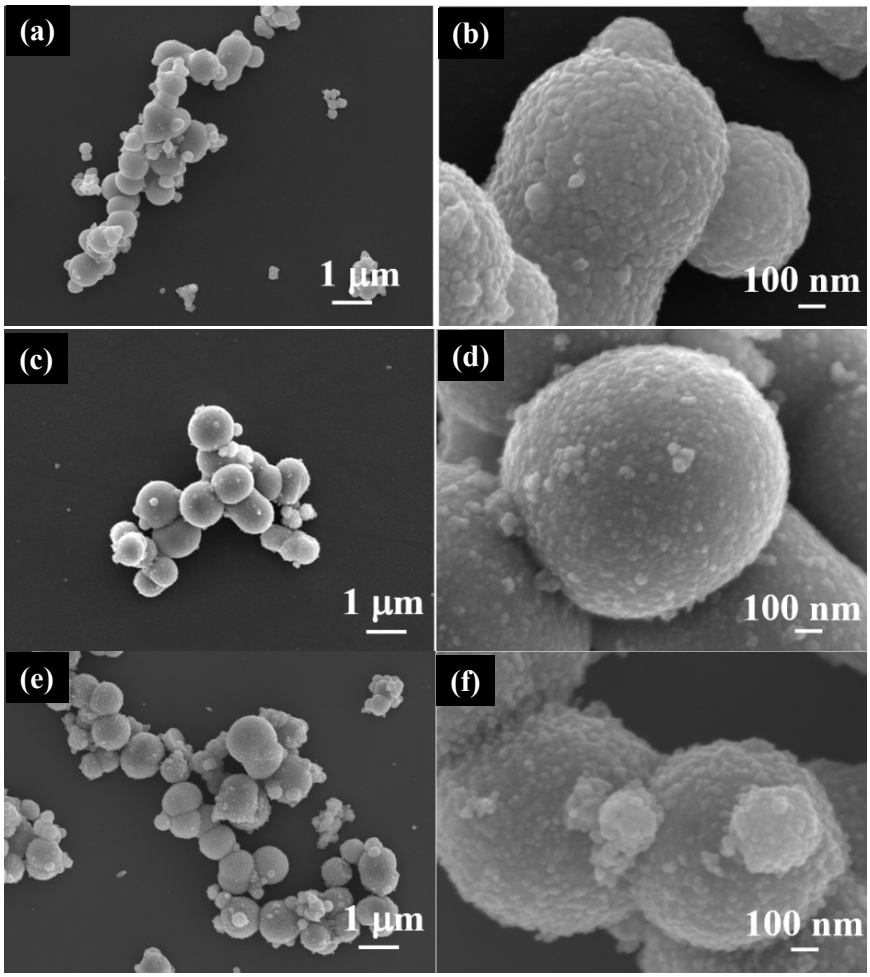

Figure 4.3 FESEM images of (a,b) NCO-250^{o}C, (c,d) NCO-350^{o}C and (e,f) NCO-450^{o}C.

Figure S4.3 shows TEM images of the intermediate product. TEM images further confirmed that the intermediate product was assembled by many flakes. Figure 4.4a, b and c show TEM images of the NCO samples obtained at 250 ^{o}C, 350 ^{o}C and 450 ^{o}C, respectively. The inserted smaller images showed that all thermally treated samples were spherical in nature. Figure 4.4a, b and c reveal that the spheres were comprised of interconnected nanoparticles, which is consistent with that observed in FESEM. Treating the sample at 250 ^{o}C, produced spheres which were assembled by many particles without clear domains, indicating they are poorly crystallized. Treating at 350 ^{o}C produced nanoparticles with clear edges, and the particle size is in the range of 8-12 nm. Moreover, the NCO-450 ^{o}C sample exhibited 12-18 nm nanoparticles with sharp edges due to improved crystallization. These results corroborate with the XRD and FESEM analysis.

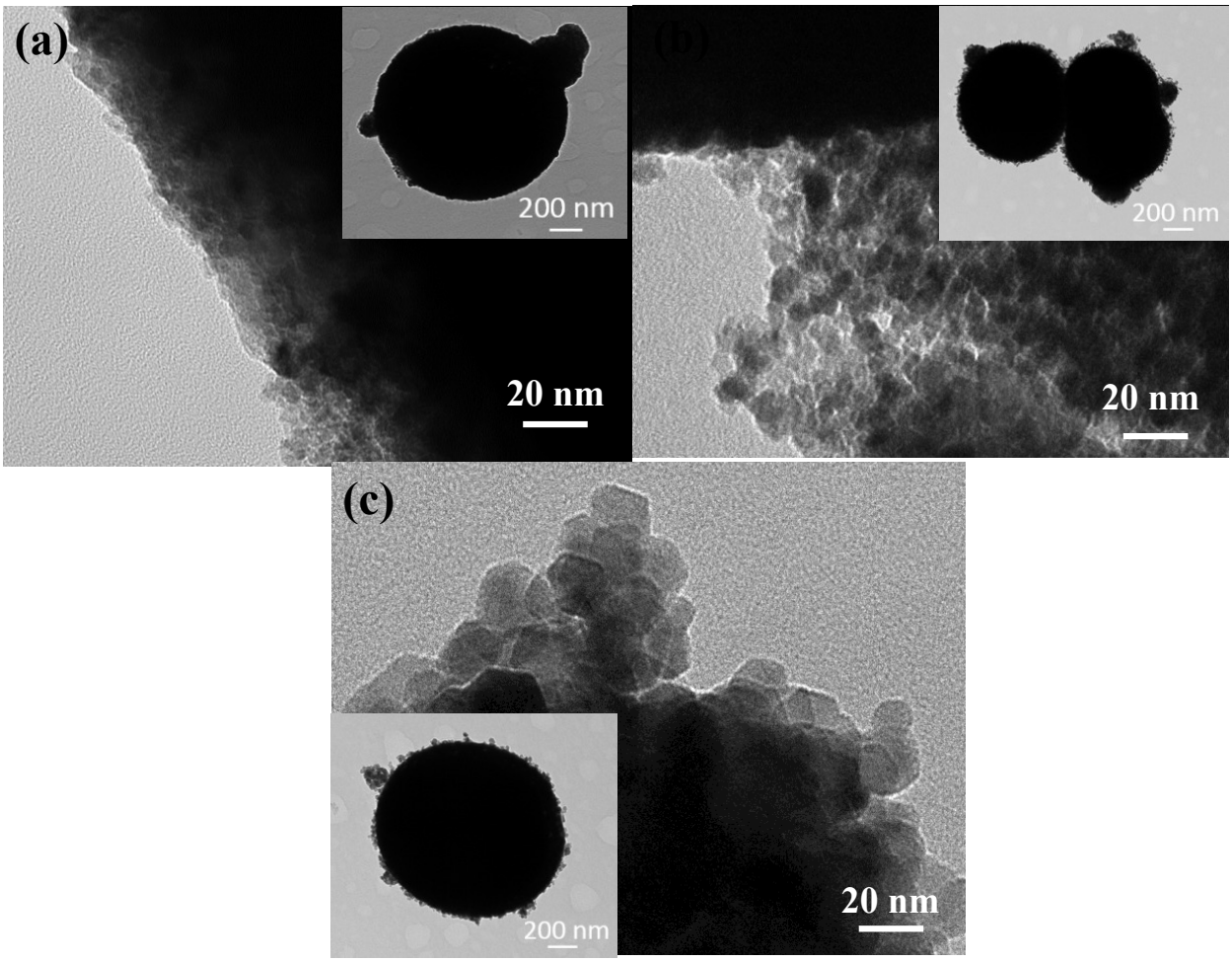

Figure 4.4 TEM images of (a) NCO-250^{o}C, (b) NCO-350^{o}C and (c) NCO-450^{o}C.

The nitrogen adsorption-desorption isotherms of the NCO thermally treated at different temperatures are shown in Figure S4.4. The NCO-250^{o}C sample exhibited a specific surface area of 31 m^2 g^{-1}. The specific surface area decreased to 21 and 8 m^2 g^{-1} for NCO-350^{o}C and NCO-450^{o}C samples respectively. This could be because the majority of the surface area is contributed by the inter-spacing between the agglomerated nanoparticles, which would be decreased by the particle growth at higher temperatures.

4.3.1 **Electrochemical performance in sodium half-cells**

The electrochemical behavior of the NCO samples obtained at different temperatures was investigated by using CV curves in the potential range of 0.005-2.50 V (versus Na^+/Na) with a sweep rate of 0.2 mV s^{-1}. Figure 4.5 shows the 3rd cycle of CV curves for the thermally treated samples. For comparison, Figure S4.5a shows the 3rd cycle of CV curve of the NiO sample. The location of the main peaks in the CV curves of the calcined samples was similar and essentially reflected the redox reaction involved the insertion and extraction of Na^+ in metallic Ni and Co. The reduction products of metallic Ni and Co are from NCO during the first discharge process.[51] Among the three thermally treated samples, the NCO-250^{o}C sample exhibited the greatest broadening of the redox peaks while the NCO-450^{o}C sample showed the narrowest redox peaks. The narrow redox peaks can be associated with the high lattice order due to the high crystallinity.[175] For the NCO-450^{o}C sample, the sharp peak at about 0 V observed from the CV curve was due to the severe polarization of the cell, which is probably related to the large size of the nanoparticles.[176] The anodic scans of thermally treated samples exhibited three obvious peaks at around 0.88 V, 1.20 V, and 1.70 V, respectively. The two peaks at 0.88 V and 1.20 V are mainly attributed to the oxidation of Ni to NiO and Co to CoO.[177,178] The last peak at 1.70 V might be due to the oxidation of CoO to Co_2O_3.[179] However, further investigation is needed to understand the redox reactions of NCO in NIBs.

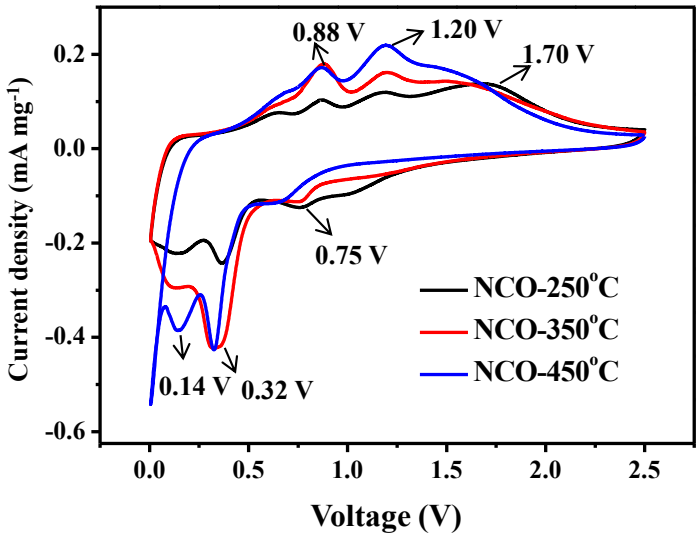

Figure 4.5 CV curves of NCO samples for the 3rd cycle from 0.005 to 2.5 V versus Na^+/Na at a scan rate of 0.2 mV s^{-1}.

Figure 4.6 shows the capacity-voltage profiles between 0.005 V and 2.5 V at a current rate of 100 mA g^{-1} for the 2nd, 50th, and 100th cycles of the NCO samples obtained after thermal treatment. The main discharge voltage plateau for the electrodes was around 0.4 V, which is in good agreement with the CV results. The sample treated at 250 °C showed a sloping profile with a small plateau region at around 0.4 V. By increasing the temperature further to 350 °C, a longer plateau near 0.4 V can be observed. The longer plateau can be associated with the high lattice order due to the high crystallinity of NCO-350°C sample. Further increasing the temperature to 450 °C led to the growth of nanoparticles, which enhances the diffusion length of sodium ions and causes severe polarization of the cell with a smaller plateau. The long discharge plateau enabled a constant power output, which is very important for the commercial use of secondary batteries.[8]

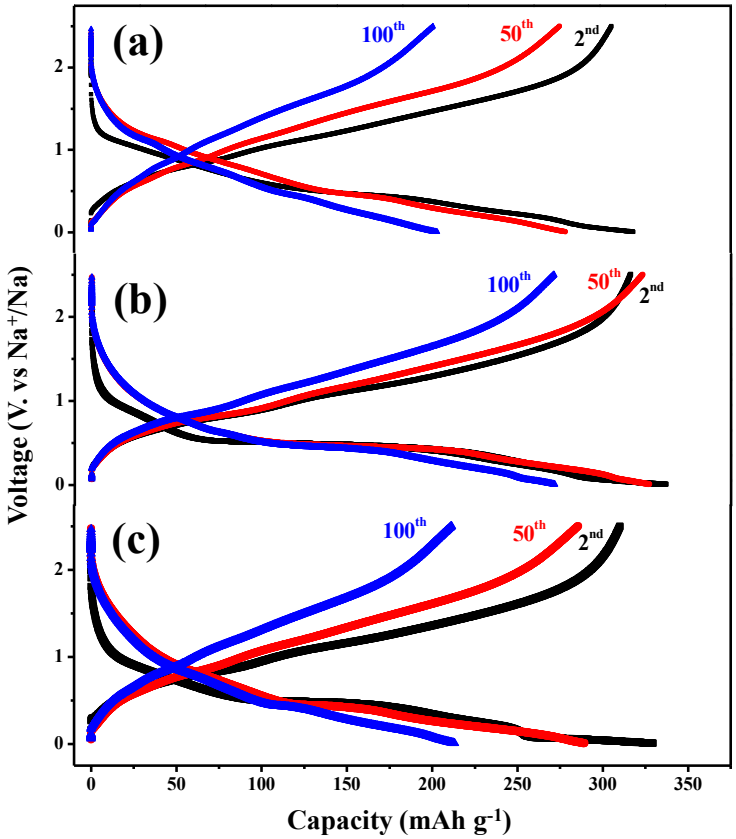

Figure 4.6 GCD curves between 0.005 V and 2.5 V versus Na^+/Na at a current rate of 100 mA g^{-1} for the 2nd, 50th, and 100th cycles of (a) NCO-250°C, (b) NCO-350°C, (c) NCO-450°C.

Figure 4.7 shows the cycling stability and rate performance of thermally treated samples. The initial discharge capacity loss of all samples is due to the formation of a SEI.[180,181] For the following several cycles, the capacity of the samples increased slightly, due to the activation of the NCO. Among the three samples studied, NCO-250°C sample showed the lowest specific capacity in both cycling stability and rate performance. The NCO-350°C sample exhibited the highest specific capacity among all cycles as well as the best rate performance. Specifically, the NCO-350°C sample exhibited a discharge capacity of 353 mAh g^{-1} at the first few cycles, and 274 mAh g^{-1} at the 100th cycle at a current density of 100 mA g^{-1}, with a capacity retention of 78%. Even at a high current density of 5.0 A g^{-1}, the capacity of NCO-350°C sample still reached 150 mAh g^{-1}. Meanwhile, its capacity can recover when the current density was reversed back to the initial low current density, which confirmed that this sample was able to tolerate the high current rate.

The 450 °C sample delivered a lower performance than that of 350 °C sample in terms of the cycling stability and rate performance. This is mainly because the increased particle size of NCO-450 °C sample with an increased sodium ions transport distance would deteriorate the electrochemical performance. The increased amount of impurity (NiO) derived from higher temperature is another reason to compromise the property of NIB, since NiO contributes less specific capacity compared to NCO (see Figure S4.5b and c). In addition, the decreased surface area of NCO-450°C would reduce the active sites accessible to the electrolyte, leading to a poor rate performance.

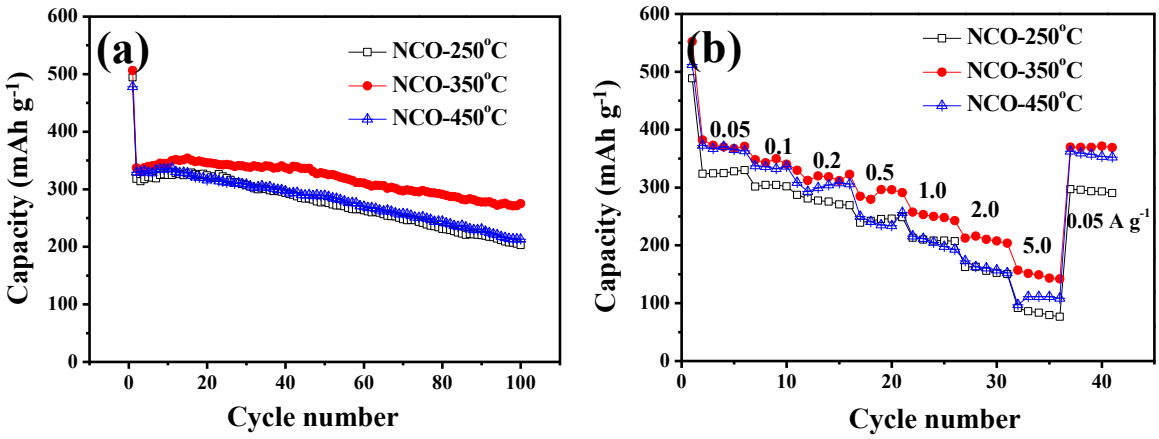

.Figure 4.7 (a) Cycling stability at a current rate of 100 mA g^{-1} and (b) rate capability of NCO-based electrodes.

Overall, the best performance of NCO-350°C sample can be attributed to: (1) it inherits sufficient active sites, because the intermediate product has been completely transformed into NCO at 350 °C; (2) it shows nanoparticles with sizes in the range of 8-12 nm, which facilitates the sodium ions transport; (3) it shows high surface area (21 m^2 g^{-1}) with sufficient active sites accessible to electrolyte which contributes to a relatively high specific capacity.

4.3.2 **Electrochemical performance in a full sodium-ion capacitor cell**

A full cell of NIC was assembled with NCO-350°C as the anode and a commercial AC as the cathode. The CV curves of the NIC cell (Figure 4.8a) exhibited evident redox peaks indicated an electrocapacitive charge storage mechanism at the electrode/electrolyte

interface. In addition, no polarizations appeared in NCO//AC NIC at the voltage range from 0-3 V, so the working voltage window of this NIC was set to be 0-3 V. Figure 4.8b presents the GCD profiles at current rates ranging from 0.5 A g^{-1} to 5 A g^{-1}. The energy and power densities were estimated and presented in Figure 4.8c. The NIC delivered an energy density of 33.75 Wh kg^{-1} at a power density of 900 W kg^{-1}. Even at a high power output of 9000 W kg^{-1}, it showed an energy density of 23.75 Wh kg^{-1}. Figure 4.8d shows the capacitance retention of the NIC, which was 70.3 % after 1000 cycles at 3 A g^{-1}.

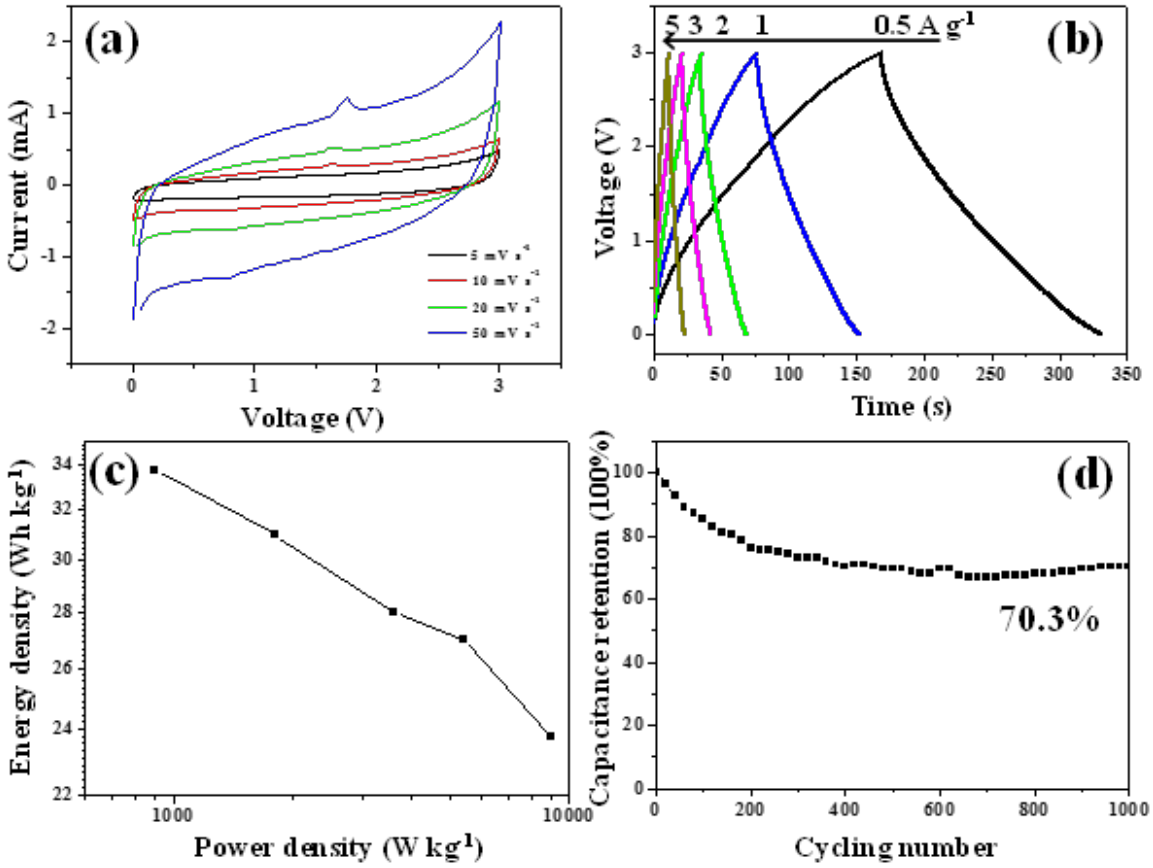

Figure 4.8 (a) CV plots, (b) GCD curves, (c) Ragone plot of the NCO//AC NIC and (d) its cycling performance at a current rate of 3 A g^{-1}.

4.4 Conclusions

In summary, we report a facile method to synthesize spherical NCO consisted of nanoparticles. The particle size and crystallinity of the NCO crystals were found to be both strongly influenced by thermal treatment temperature. The sample treated at 250 °C did not

lead to a complete crystallization of the intermediate product, therefore showed a poor electrochemical performance in NIBs. With the increase in treatment temperature, the nanoparticles of the products became larger and better crystallized. The sample treated at 350 ^{o}C showed highly crystallized nanoparticles with sizes in the range of 8-12 nm. Raising the temperature to 450 ^{o}C led to an increased nanoparticle size of 12-18 nm with an increased amount of NiO phase, as well as a decreased surface area. Overall, the NCO obtained at 350 ^{o}C exhibited the highest specific capacity, and the best rate performance, delivering a discharge capacity of 274 mAh g^{-1} after 100 cycles at 100 mA g^{-1} and 150 mAh g^{-1} at 5 A g^{-1}. A NIC assembled using this sample as the anode and a commercial AC as the cathode delivered an energy density of 33.75 Wh kg^{-1} at a power density of 900 W kg^{-1}, with a cycling stability of 70.3 % (3 A g^{-1}) after 1000 cycles. Through this work we demonstrated that the crystal structure and electrochemical properties of spherical NCO were greatly influenced by the thermal treatment.

4.5 Supplement data

Synthesis of NiO: 3 mmol of $Ni(NO_3)_2.6H_2O$ were dissolved into 45 mL of isopropanol and 9 ml of glycerol. After stirring for 20 minutes, the solution was transferred to a Teflon-lined stainless steel autoclave and kept at 180 ^{o}C for 6 h to acquire NiO-precipitate (NiO-p). After cooling down naturally, the NiO-p solid was collected by centrifugation and washed with high purified water and ethanol several times and dried in an oven at 80 ^{o}C. Then the NiO-p were thermally treated at 350 ^{o}C in air for 2 h with a slow heating rate of 2 ^{o}C min^{-1}, producing NiO.

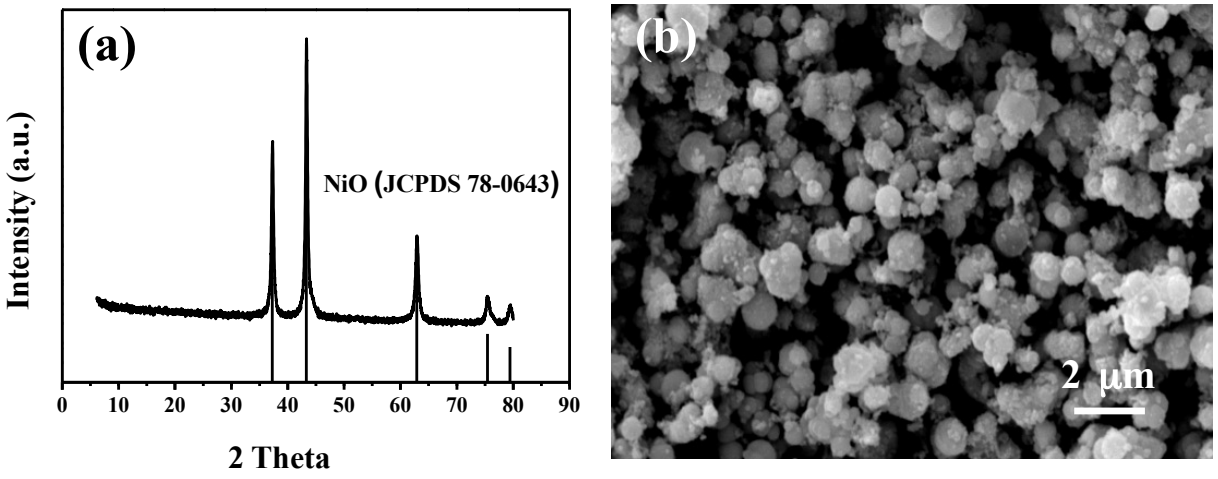

Figure S4.1 (a) XRD pattern and (b) SEM image of NiO sample.

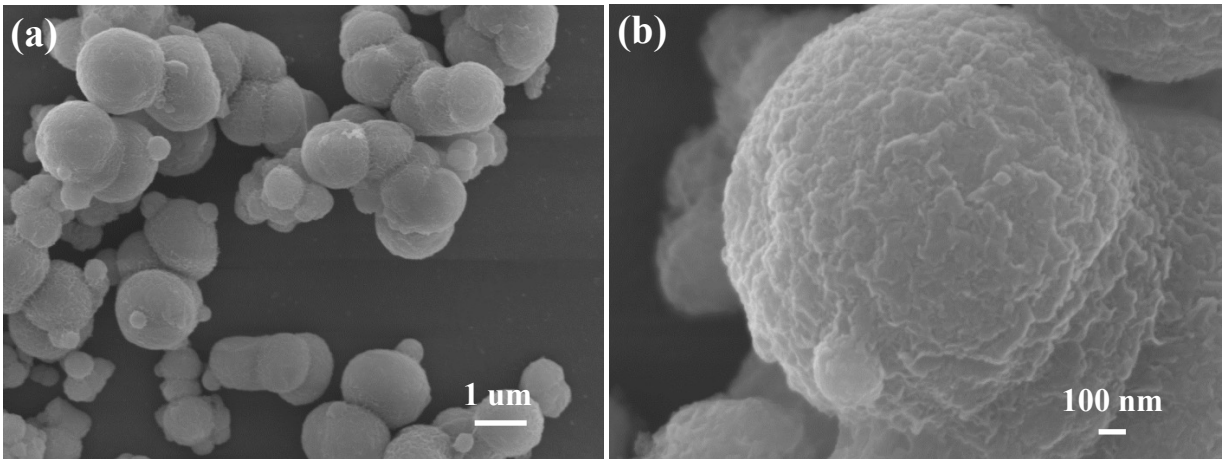

Figure S4.2 FESEM images of the intermediate product.

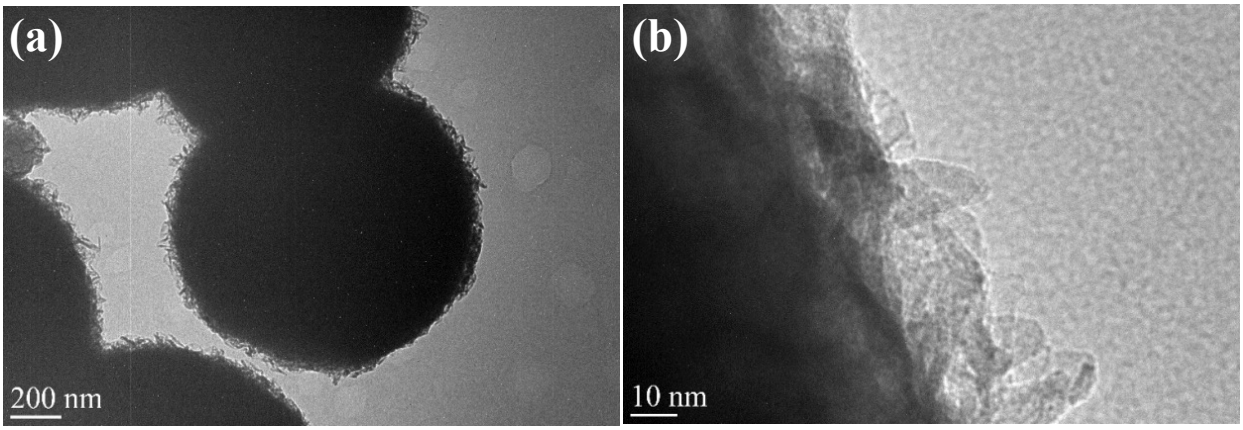

Figure S4.3 TEM images of (a) low and (b) high magnification of the intermediate product.

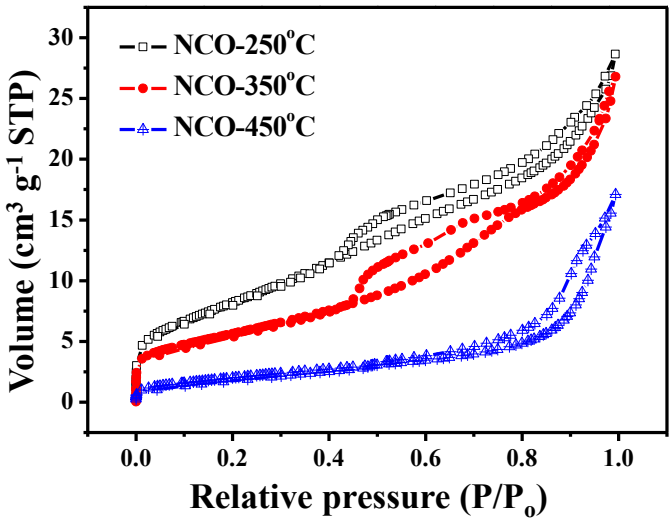

Figure S4.4 Nitrogen adsorption/desorption isotherms of NCO samples.

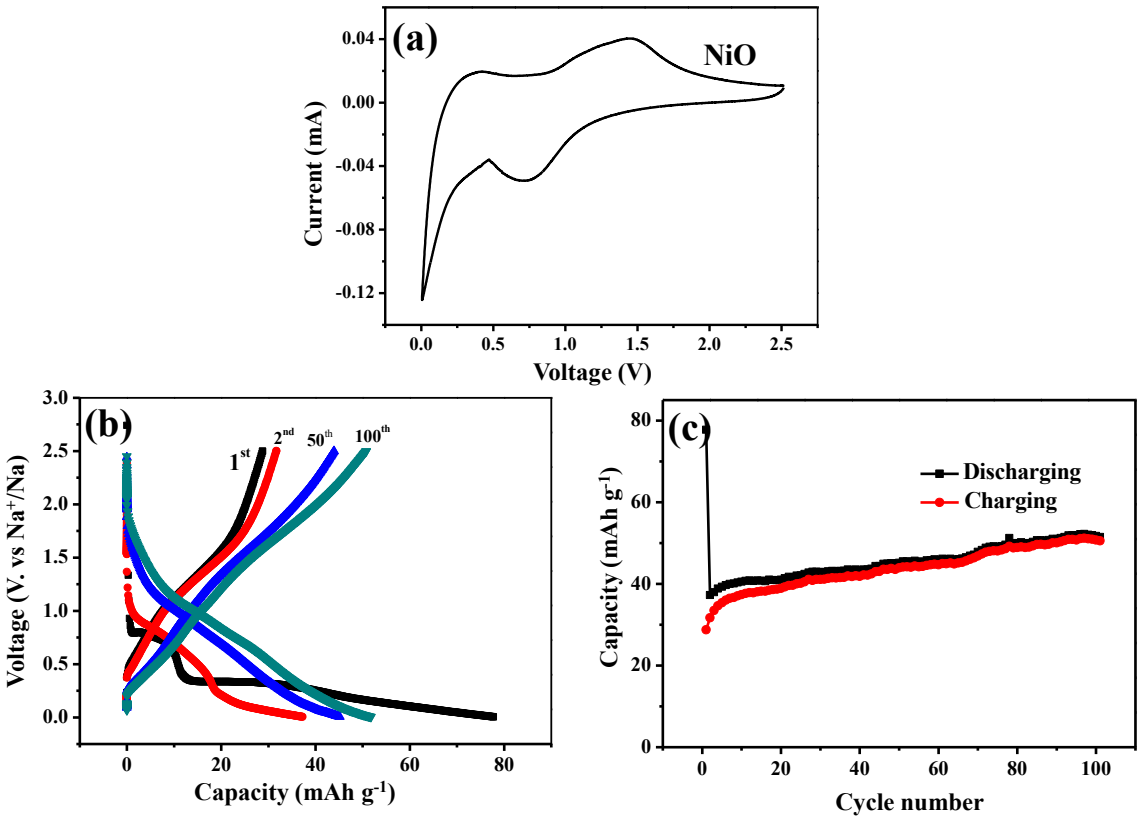

Figure S4.5 (a) CV curves, (b) GCD profiles for the 1st, 2nd, 50th, and 100th cycles and (c) cycling stability at a current rate of 100 mA g^{-1} of NiO sample.

Chapter 5 Pre-sodiated $NiCo_2O_4$ for high-performance sodium-ion capacitors

This chapter has been published in *Journal of Power Sources*, 2017, **362**, 358–365.

This chapter studies the sodium-ion storage mechanism in nickel cobaltite ($NiCo_2O_4$), and demonstrates that pre-sodiation of $NiCo_2O_4$ can significantly improve its energy density. Here, $NiCo_2O_4$ hollow spheres with a chestnut shell morphology have been solvothermally synthesized and tested in a sodium half-cell. The $NiCo_2O_4$ material exhibited a reversible capacity of 313 mAh g^{-1} at 1 A g^{-1}. A sodium-ion capacitor fabricated with pre-sodiated $NiCo_2O_4$ as the anode and an activated carbon as the cathode delivered an energy density of 60 Wh kg^{-1} at the power density of 10,000 W kg^{-1}. *Ex-situ* XRD and TEM results reveal that the $NiCo_2O_4$ phase was converted to metallic nickel and cobalt and Na_2O phases during the pre-sodiation. The metallic nickel and cobalt phases are kinetically favorable for the electrolyte diffusion and electrochemical reactions, thus significantly improving the performance of the pre-sodiated $NiCo_2O_4$ electrode.

5.1 Introduction

Electrochemical capacitors (ECs) store energy using either ion adsorption (electrical double-layer capacitors, EDLCs) or surface redox reactions (pseudocapacitors) with prominent properties, such as high power density and long cycle life.[43,182] But, the energy density of ECs is low. Rechargeable batteries exhibit high energy density, but low power density.[183] Hybrid energy storage devices have been investigated with considerable effort in recent years.[184,185] The idea is to combine the high power density of ECs with the high energy density of batteries within one system. Lithium-ion capacitors (LICs) are a typical example of such hybrid energy storage systems, which integrates the electrode component of ECs and rechargeable lithium-ion batteries (LIBs).[186,187] This integration enables the LIC to

exhibit a higher energy output than ECs and a higher power output than LIBs.[188,189,16,11,190] However, the increasing cost and limitation of lithium resources have largely hindered wide applications of this advanced energy storage technology.[9,191] In this regard, sodium-ion capacitors (NICs) have been considered as a promising alternative to LICs due to the nature abundance of sodium resources.

A NIC is generally configured with a porous carbon as the cathode and a battery electrode as the anode. A number of research attempts towards developing anode materials in the recent past as the anode significantly determines the cell performance in terms of power density and life time. To date, various anode materials have been explored, such as $Na_xH_{2-x}Ti_3O_7$,[21] V_2O_5/CNT,[19] $Na_2Ti_3O_7$@CNT,[27] $NiCo_2O_4$,[22] nitrogen-doped TiO_2,[31] and Nb_2O_5@C/rGO.[28] Among them, nickel cobaltite ($NiCo_2O_4$) with a theoretical specific capacity of 890 mAh g^{-1} [51] is of particular interest for both NICs[52] and sodium-ion batteries.[53–55,204] Zhang *et al.*[54] studied the sodium-ion storage properties of NCO spheres in a sodium half-cell. A specific capacity of about 440 mAh g^{-1} after 200 cycles was achieved at a current density of 0.1 A g^{-1}. Ding *et al.*[22] investigated $NiCo_2O_4$ (NCO) material as an anode in a full NIC cell with an activated carbon (AC) as the cathode. A poor electrochemical performance with an energy density of 13.8 Wh kg^{-1} at a power density of 308 W kg^{-1} was obtained.

In this work, NCO spheres with a chestnut shell morphology were solvothermally synthesized. The pre-sodiation strategy that has been found to be effective in improving the performance of hard carbon[20] and graphitic mesocarbon microbeads (Na_nMCMB)[108] for NICs was adopted to improve the performance of NCO. Our experimental results showed that pre-sodiation of NCO significantly enhanced the energy density. A NIC fabricated with a pre-sodiated NCO as the anode and a commercial AC as the cathode delivered energy densities of 120.3 Wh kg^{-1} and 60.0 Wh kg^{-1} at power densities of 200 W kg^{-1} and 10,000 W kg^{-1}, respectively. The electrode also exhibited a good stability against cycling with a capacitance retention of 85 % after 2000 cycles at 3 A g^{-1}.

5.2 Experimental section

5.2.1 **Materials synthesis**

NCO was synthesized using the solvothermal method. In brief, 2 mmol of $Co(NO_3)_2 \cdot 6H_2O$, 1 mmol of $Ni(NO_3)_2 \cdot 6H_2O$ and 3.6 g of urea were dissolved in a mixture of 45 mL isopropanol plus 9 mL water under stirring. Then, 175 uL ethylenediamine was added under stirring. After 10 min, the the mixture was transferred to a 70 mL Teflon-lined stainless steel autoclave and heated at 120 ºC for 10 h. The solid product was collected by centrifugation and washed with distilled water and ethanol, and dried in an oven at 80 ^{o}C. The solid was then thermally treated at 350 ºC in air for 2 h at a heating rate of 1 ºC min^{-1} to obtain the as-synthesized NCO. The pre-sodiation of the as-synthesized NCO was conducted by galvanostatically discharging a sodium half-cell (NCO//Na) from open circuit potential to 0.005 V. The discharging current density was set to be 100 mA g^{-1}. After disassembling the cell, a pre-sodiated NCO sample was obtained. The pre-sodiated sample is hereinafter designated as Na_nNCO.

5.2.2 **Materials characterization**

Crystalline phases were analysed using a Bruker D8 X-ray diffractometer with Ni-filtered Cu Kα radiation (λ = 1.54056 Å, 40 kV, 30 mA) at a scan rate of 2 º min^{-1}. FESEM (JEOL 7100) and TEM (F20Tecnai 20) were used to characterize the morphology of samples. XPS spectra was acquired on a Kratos Axis ULTRA X-ray photoelectron spectrometer with a 165 mm hemispherical electron energy analyzer and a monochromatic Al Kα (1486.6 eV) radiation at 225 W (15 kV, 15 mA). Nitrogen adsorption/desorption isotherms were measured on a Tristar II 3020 (Quantachrome) at the liquid nitrogen temperature. The specific surface areas of the samples were calculated using the BET method from the nitrogen adsorption isotherms. The total pore volumes were estimated from the nitrogen volumes absorbed at the maximum relative pressures equal to 0.99. The pore size distribution curves were obtained by the Barrett-Joyner-Halenda (BJH) method based on the nitrogen desorption data. For both *ex-situ* XRD and TEM measurements, electrode samples were collected at different states of charge and discharge by disassembling coin cells in an Ar-filled glovebox. The *ex-situ* XRD measurement was conducted in an Ar-filled container. For the *ex-situ* TEM measurement, a drop of sample suspension in ethanol was

deposited onto a carbon-coated Cu-grid and dried naturally in the glove box before transferring to the TEM chamber.

5.2.3 **Electrochemical measurements**

The NCO and a commercial AC with a specific surface area of 1200 m^2 g^{-1} from AC Technologies Pty Ltd, Australia, were respectively used as the anode and cathode in assembling NIC cells. Electrodes were prepared by mixing 70 wt.% of an active material, 20 wt.% of an electrical conductor (carbon black), and 10 wt.% of a binder (carboxymethyl cellulose, CMC) in de-ionized water to form a slurry, which were subsequently coated on a copper current collector for NCO slurry and an aluminium foil current collector for the AC slurry. After the electrodes were dried at 60 °C overnight in a vacuum oven, they were punched into circular discs and assembled in a 2032-type coin cell with a glass fibre (GF/C, Whatman, USA) as the separator and 1 M $NaClO_4$ dissolved in a mixture of ethylene carbonate (EC) and propylene carbonate (PC) (volume ratio: 1:1) plus 2 vol. % fluorinated ethylene carbonate (FEC, provided by HSC Corporation) as the electrolyte. The electrolyte preparation, the coin cell assemblies and disassembles were all performed in an Argon filled glovebox.

The sodium half-cell (NCO//Na) was assembled by using the NCO and Na metal plate as the electrodes. A NIC cell (Na_nNCO//AC) was assembled using the Na_nNCO as the anode electrode and the AC as the cathode electrode. The mass ratio of the cathode electrode (m_+) over the anode electrode (m_-) was varied from 2.0 to 3.6 for optimizing the device performance. For comparison purpose, a NIC cell (NCO//AC) was assembled using the as-prepared NCO without pre-sodiation as the negative electrode and the same AC as the positive electrode. A symmetric AC//AC supercapacitor cell was also assembled using the AC as both anode and cathode electrode.

5.3 Results and discussion

The XRD pattern (Figure S5.1a, in the supplementary data 5.5) of the NCO sample before pre-sodiation matches well with that of the NCO phase (73-1702). The FESEM images depicted in Figure 5.1a and 1b revealed that the NCO sample consists of spherical particles with a chestnut shell morphology. The spheres are hollow (Figure 5.1b). The TEM image

(Figure 5.1c) further confirmed the hollow structure and chestnut shell morphology. The TEM image in Figure 5.1d taken from the marked area of Figure 5.1c shows that each needle was composed of numerous nanoparticles.

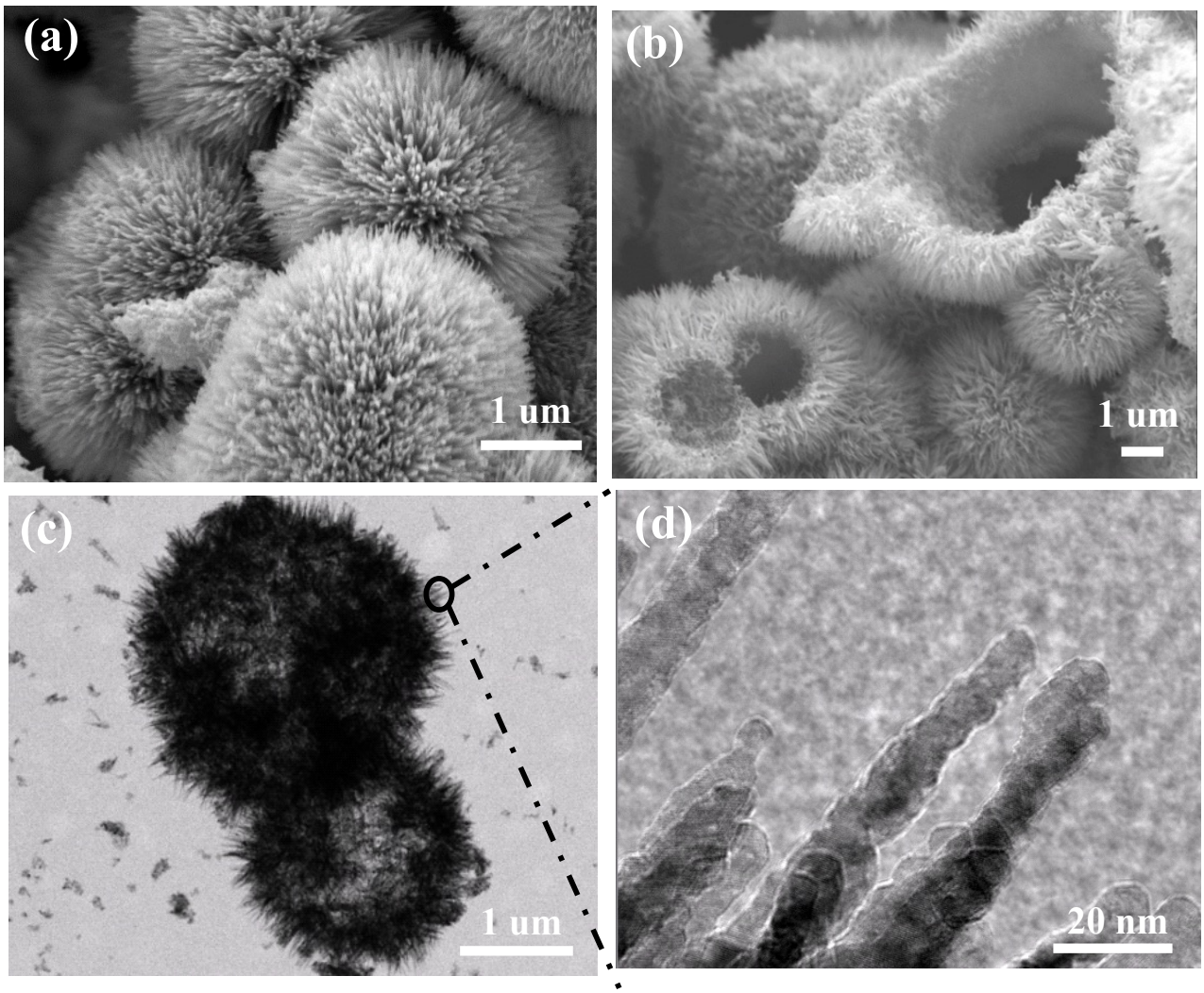

Figure 5.1 (a, b) SEM images, and (c, d) TEM images of the NCO sample before pre-sodiation.

Figure S5.1b shows the N_2 adsorption-desorption isotherms of the as-synthesised NCO sample. The type IV isotherm with a hysteresis loop in the relative pressure range between 0.7 and 1.0 is an indicative of a mesoporous material. The specific surface area was estimated to be 62.0 m^2 g^{-1}, and the pore volume was 0.291 cm^3 g^{-1}. The inset in Figure S5.1b shows the corresponding pore size distribution curve, which exhibits two prominent mesoporous peaks at 9.8 and 27 nm, respectively. The presence of mesopores provides

not only extra space for alleviating the volume expansion upon charging/discharging, but also facilitates charge transfer.

Figure 5.2 shows the XPS spectra of the as-synthesised NCO sample. The wide scan survey spectrum (Figure 5.2a) shows the presence of Ni, Co, O and C. Figure 5.2b shows the Ni 2p core electron spectrum, which was deconvoluted with two peaks assigned to Ni^{2+} and Ni^{3+} respectively, along with two satellite peaks. Similarly, the Co 2p spectrum (Figure 5.2c) was deconvoluted with two peaks of Co^{2+} and Co^{3+} also with two shakeup satellites. Figure 5.2d shows the O 1s XPS deconvoluted spectra. The three peaks at about 532.6, 531.0 and 529.4 eV were due to adsorbed water, oxygen-containing groups (defects), and metal-oxygen bonds, respectively.[194,195] The XPS results suggest that NCO sample contains the chemical bonds of Ni^{2+}/Ni^{3+} and Co^{2+}/Co^{3+}, which is in agreement with the literature.[146,194,196,197]

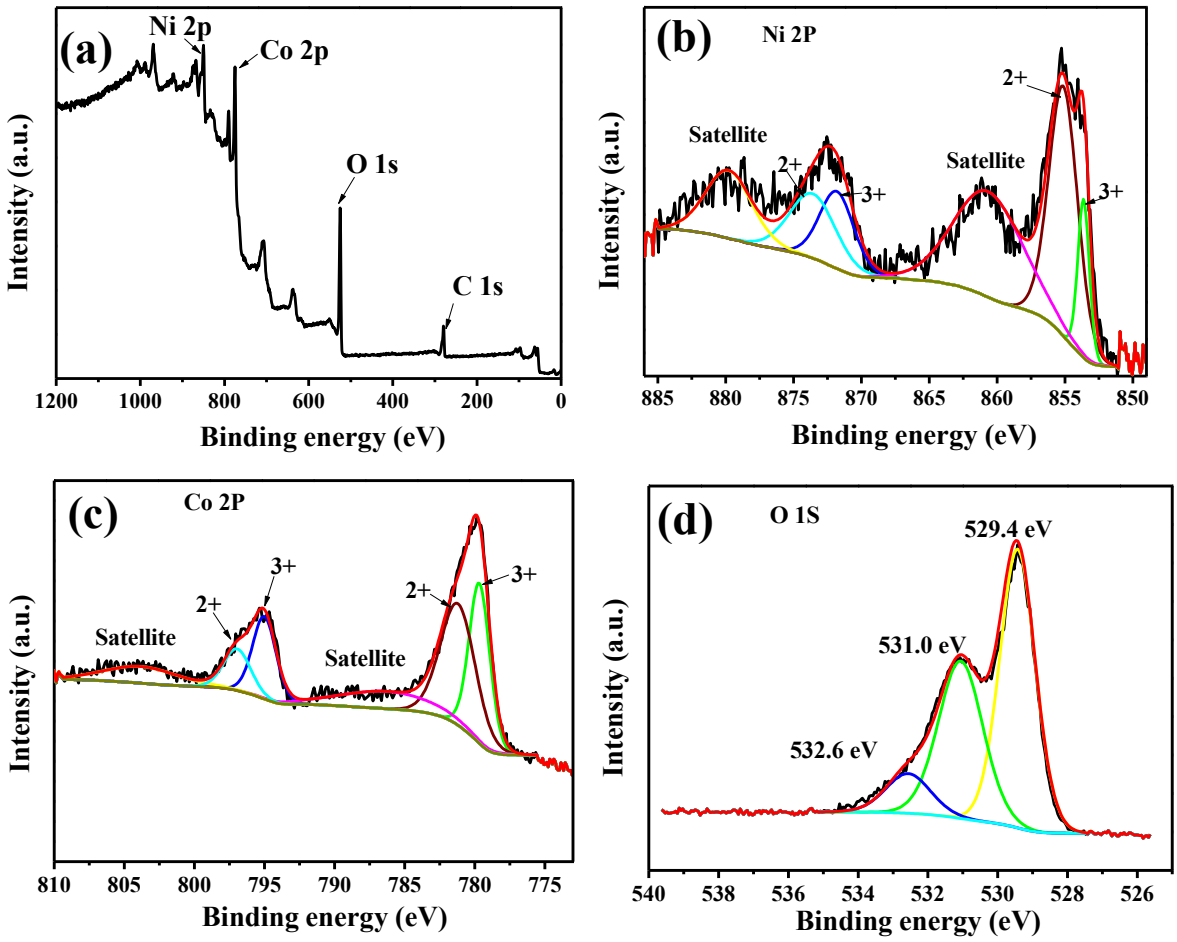

Figure 5.2 XPS spectrum of (a) survey spectrum, (b) Ni 2p, (c) Co 2p and (d) O 1s for NCO.

5.3.1 **Electrochemical performance in a sodium half-cell**

Before assembling a full NIC, the electrochemical performance of the NCO materials was assessed in a sodium half-cell. Figure 5.3a shows the CV profiles of the first three cycles. Two cathodic peaks at 0.47 and 0.95 V respectively appeared in the first cycle. However, only one cathodic peak at 0.63 V can be observed from the CV curves of the second and third cycles. The different CV profiles in the first and subsequent cycles indicate that the cathodic reaction path of the first cycle was different from that in the subsequent cycles. In contrast, two anodic peaks at 1.08 and 1.68 V respectively can be seen over the three cycles, corresponding to redox reactions, which is discussed in the section 5.3.3. Figure 5.3b shows the GCD profiles at current rates 0.1 and 1 A g^{-1}, respectively. The discharge plateau exhibited a small voltage difference when the current rate changed from 0.1 to 1 A g^{-1}, indicating that the cell experienced a low electrochemical polarization.[198,199] Figure 5.3c shows the specific capacities at different current rates. It can be seen that the cell achieved specific capacities of about 530, 480, 310, and 170 mAh g^{-1} at current densities of 0.05, 0.1, 1, and 5 A g^{-1}, respectively. Remarkably, the cell delivered a capacity of 450 mAh g^{-1} when the current density was reversed back to 0.1 A g^{-1} after having been cycled at higher current densities, indicating a good reversibility. Figure 5.3d shows the cycling performance of the as-synthesized NCO electrode. At 0.1 A g^{-1}, the initial discharge and charge capacities were 695 mAh g^{-1} and 480 mAh g^{-1}, respectively. The initial capacity loss was mainly due to the formation of solid electrolyte interphase (SEI).[200] It should be noted that 85% of capacity was retained (266 mAh g^{-1}) after 100 cycles at a current density of 1 A g^{-1}, showing a good stability against cycling at high current rates.

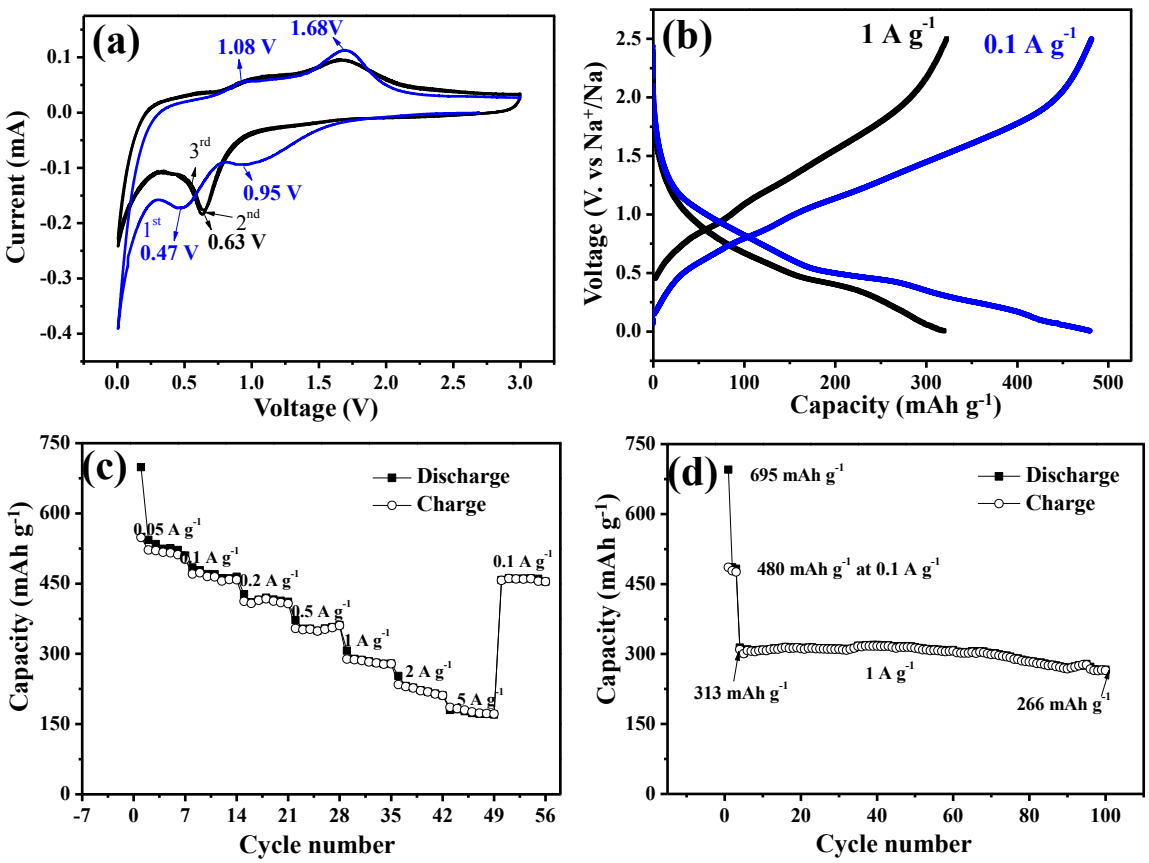

Figure 5.3 Electrochemical performance of the NCO electrode before pre-sodiation in a sodium half-cell: (a) CV curves at a scan rate of 0.2 mV s^{-1}, (b) GCD profiles at current rates of 0.1 A g^{-1} and 1 A g^{-1}, (c) specific capacities at different current rates, and (d) cycling performance at a current rate of 1 A g^{-1}.

5.3.2 **Electrochemical performance in a full sodium-ion capacitor cell**

In the hybrid system Na_nNCO//AC, the mass balance between the cathode and anode has a significant impact on the overall device performance. To optimize the mass ratio of the two electrodes, the GCD technique was used to test the performance of the 4.0 V Na_nNCO//AC cells configured with different mass ratios between the cathode (m_+) and the anode (m_-) (m_+/m_- = 2.0. 2.4, 2.8, 3.2 and 3.6) under a current rate of 0.5 A g^{-1}, and the results are shown in Figure 5.4a. Figure 5.4b shows the capacitance as a function of mass ratio. Evidently, the maximum capacitance of the NIC cell was achieved when the mass ratio of the cathode over the anode was 3.2, which was 38.8 F g^{-1}.

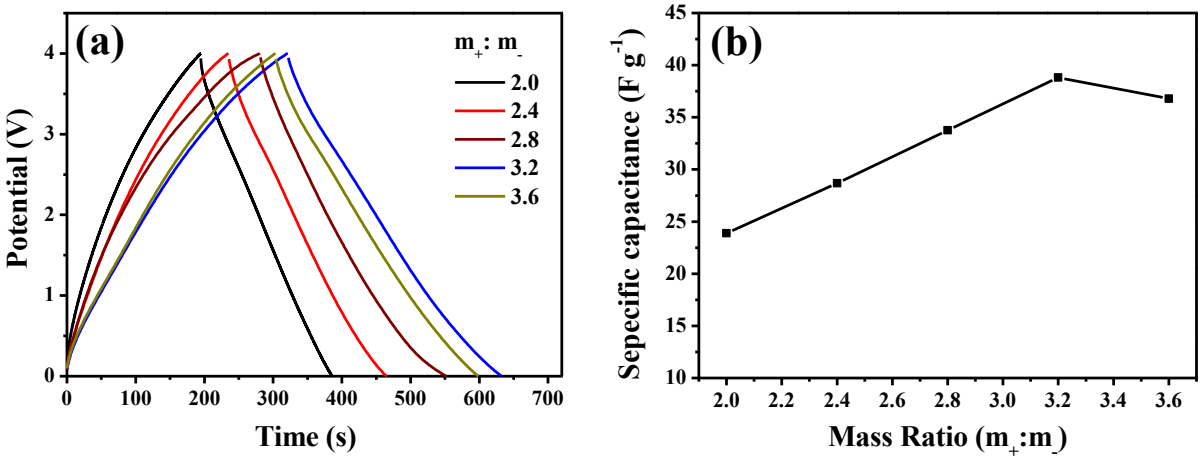

Figure 5.4 (a) GCD curves and (b) specific capacitance as a function of mass ratio between cathode and anode at 0.5 A g^{-1} of Na_nNCO//AC NIC.

Figure 5.5 compares the electrochemical performance of the NCO electrode materials before and after pre-sodiation measured using full NIC cell configuration. Unlike the CV curves of the NCO//AC NIC cell (Figure 5.5d) which exhibited evident redox peaks, the nearly rectangular shape of the CV curves of the Na_nNCO//AC cell (Figure 5.5a) indicates an electrocapacitive charge storage mechanism at the electrode/electrolyte interface.[19,29,201] In addition, the severe polarizations appeared in NCO//AC NIC at the voltage range from 0-4 V and 0-3.5 V, so the working voltage window of this NIC was set to be 0-3 V. However, a potential range from 0 to 4 V was achieved in Na_nNCO//AC cell. The high potential can be attributed to the pre-sodiation process. AC positive electrode generally shows a potential of 1.5-4.2 V versus Na^+/Na.[202] The pre-sodiation process enables the open circuit potential of the NCO electrode (2.25 V) decrease to 0.005 V, allowing Na_nNCO negative electrode shows a potential of 0.005-2.5 V versus Na^+/Na (Figure 5.3b). A high working voltage window of the capacitor is favorable to enhance the energy density and power density of the device. This Na_nNCO//AC NIC combing the advantages of the rechargeable battery and a supercapacitor, with a high operating voltage windows renders fast energy storage kinetics, is expected to acheive higher energy and power densities.

The GCD curves of Na_nNCO//AC and NCO//AC NICs are shown in Figure 5.5b, c, and e, f, respectively. At a current density of 0.1 A g^{-1}, the hybrid NIC fabricated with the pre-sodiated NCO as the anode delivered a capacitance of 54.2 F g^{-1}, three times higher than the hybrid

capacitor cell fabricated with the non-pre-sodiated NCO as the anode (19.1 F g^{-1}). The Na_nNCO//AC NIC exhibited an energy density of 120.3 W h kg^{-1} at a power density of 200 W kg^{-1}, while the NCO//AC NIC showed a much lower performance with an energy density of 24.0 Wh kg^{-1} at a power density of 120 W kg^{-1}. The performance of NCO without pre-sodiation is comparable to that of a previously reported NCO//AC NIC.[22] At a higher current rate, namely 5 A g^{-1}, the Na_nNCO//AC NIC still performed well to deliver a specific capacitance of 27.0 F g^{-1}, an energy density of 60.0 Wh kg^{-1} and a power density of 10,000 W kg^{-1}, in sharp contrast to the performance of NCO //AC NIC, which had a specific capacitance of 5.4 F g^{-1}, an energy density of 6.8 Wh kg^{-1} at the power density of 6 kW kg^{-1}. Figure 5.5g compares the Ragone plots of Na_nNCO//AC and NCO//AC NICs, with other AC-based NICs reported in the literature.[15,21,22,27,28,31,102]The electrochemical properties of the symmetric AC//AC supercapacitor were also tested for comparison purpose (Figure S5.2). Evidently, the Na_nNCO//AC NIC fabricated in this work with pre-sodiated NCO as the anode performed the best. The electrode stability against cycling was studied at a current density of at 3 A g^{-1}, and the results are shown in Figure 5.5h. It can be seen that 85.0 % of its initial capacitance can be retained after 2000 cycles, indicating this NCO is electrochemically stable against charge/discharge cycles at high current density.

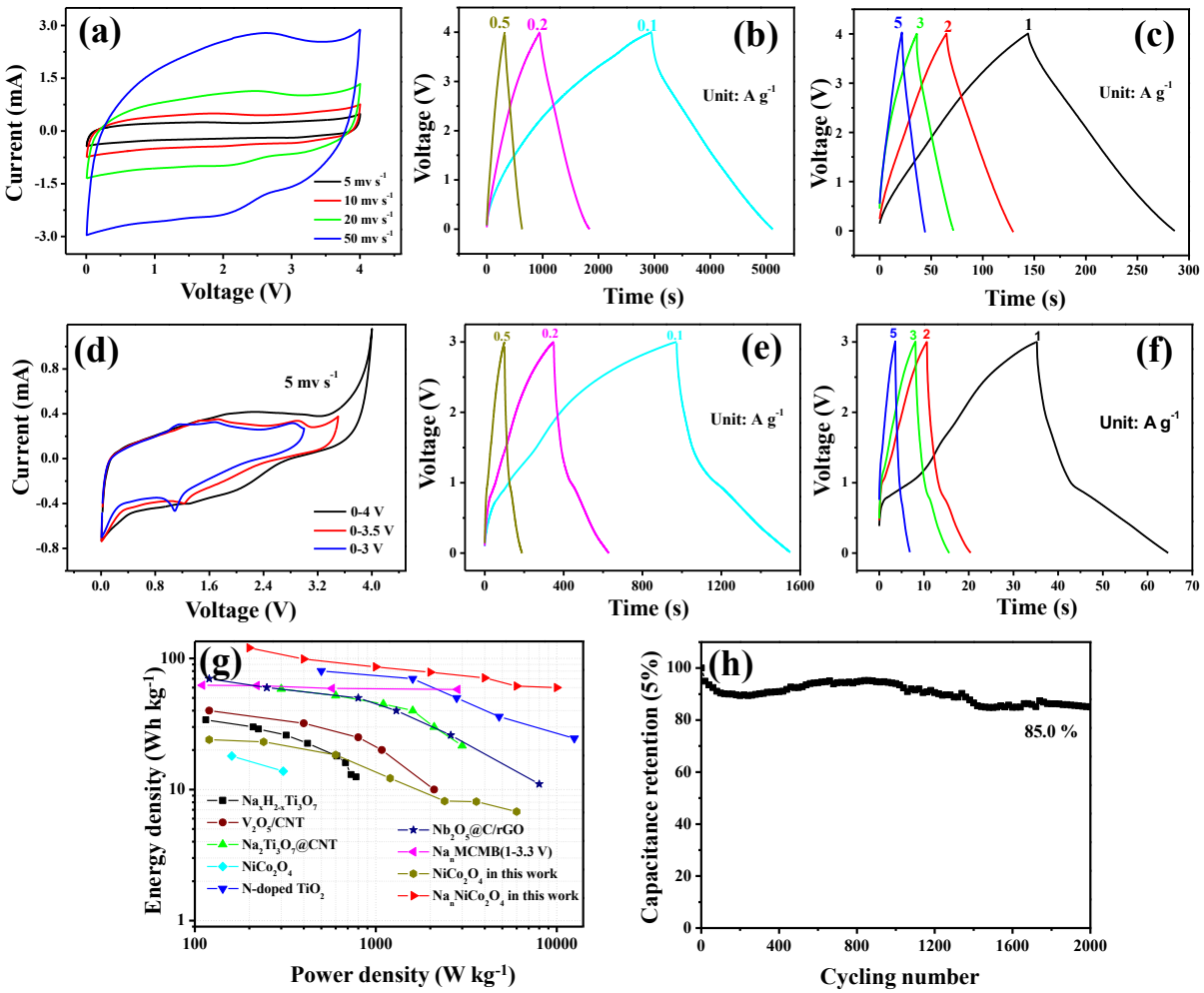

Figure 5.5 CV plots of the Na_nNCO//AC (a) and the NCO//AC NICs (d), GCD curves of the Na_nNCO//AC NIC (b and c) and the NCO//AC NIC (e and f) at different current rates, (g) Ragone plot of the Na_nNCO//AC cell in comparison with other AC-based NIC cells, and (h) cycling performance of the Na_nNCO//AC NIC at 3 A g^{-1}.

5.3.3 **Sodium-ion storage mechanism**

To reveal phase change of NCO during cycling, samples after charge/discharge at different voltages, designated as D-0.7V, D-0.005V, C-1.2V, and C-2.5V, where D and C represent discharge and charge, respectively, were collected and are shown in Figure 5.6a. The *ex-situ* XRD patterns of the as-synthesized NCO before cycling (pristine) along with the samples collected at different discharge/charge voltages are shown in Figure 5.6b. The pristine sample showed all XRD peaks corresponding to spinel NCO (Figure 5.1a). The XRD peaks became broader for sample D-0.7V, and the XRD pattern of sample D-0.005V

became featureless. The broadening and almost disappearing of the XRD peaks upon discharging were most probably due to particle size decreasing, as has been observed before [178,203]. This is supported by the *ex-situ* TEM results (Figure S5.3), from which it can be estimated that the particle size of the pristine sample is in the range of 5-10 nm (Figure S5.3a) while the discharged sample at 0.005 V exhibited smaller particle sizes in the range of 2-4 nm (Figure S5.3b). During the first charge, the XRD patterns appeared peaks at 43.0 and 61.5 two theta at C-1.2V which could be assigned to phases NiO (78-0643) and CoO (78-0431), and further appeared peak at 36.8 two theta at C-2.5V which could be contributed by Co_3O_4 (78-1969). The phases at C-2.5V were further confirmed by the HRTEM images (Figure S5.2c). The lattice fringes spacing of 2.09 Å and 2.43 Å correspond to the planes of NiO (200) and Co_3O_4 (311), respectively.

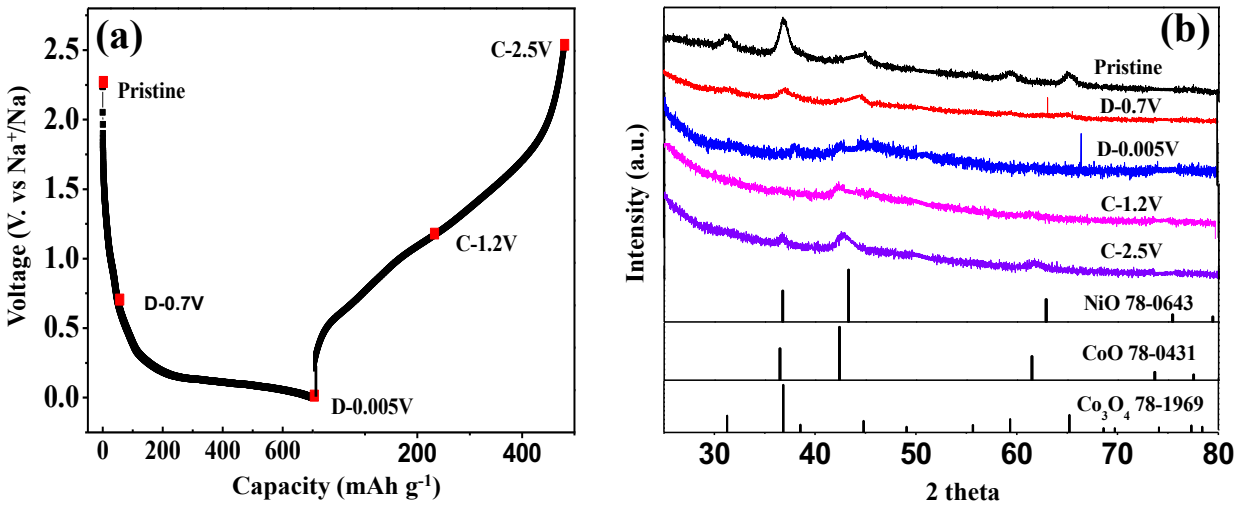

Figure 5.6 (a) First charge/discharge curves of the NCO electrode at 0.1 A g^{-1} and (b) *ex-situ* XRD patterns of electrode samples before and after charge/discharge.

Figure 5.7a shows the selected area electron diffraction (SAED) patterns of the NCO electrode during the first charge/discharge. The SAED pattern of the pristine sample confirmed the NCO phase. After the first discharge, the NCO phase was changed to metallic Ni and Co, as well as Na_2O,[51] as revealed by the presence of the (200) diffraction rings of both Ni and Co, as well as the (220) diffraction ring of Na_2O (Figure 5.7c). Besides, a couple of diffusive rings of NiO and CoO phases can be observed on sample D-0.005V. The two phases were formed probably due to self-discharging.[204] During the first charge, it appears phase changes occurred from the nickel cobaltite phase to NiO and CoO phases at C-1.2V

(Figure 5.7d), and further to NiO and Co_3O_4 phases at 2.5 V (Figure 5.7e). The two steps of conversion reaction during the charging process were evidenced by the two anodic peaks at 1.08 V and 1.68 V of the CV curves shown in Figure 5.3a. The SAED results are consistent to the XRD patterns.

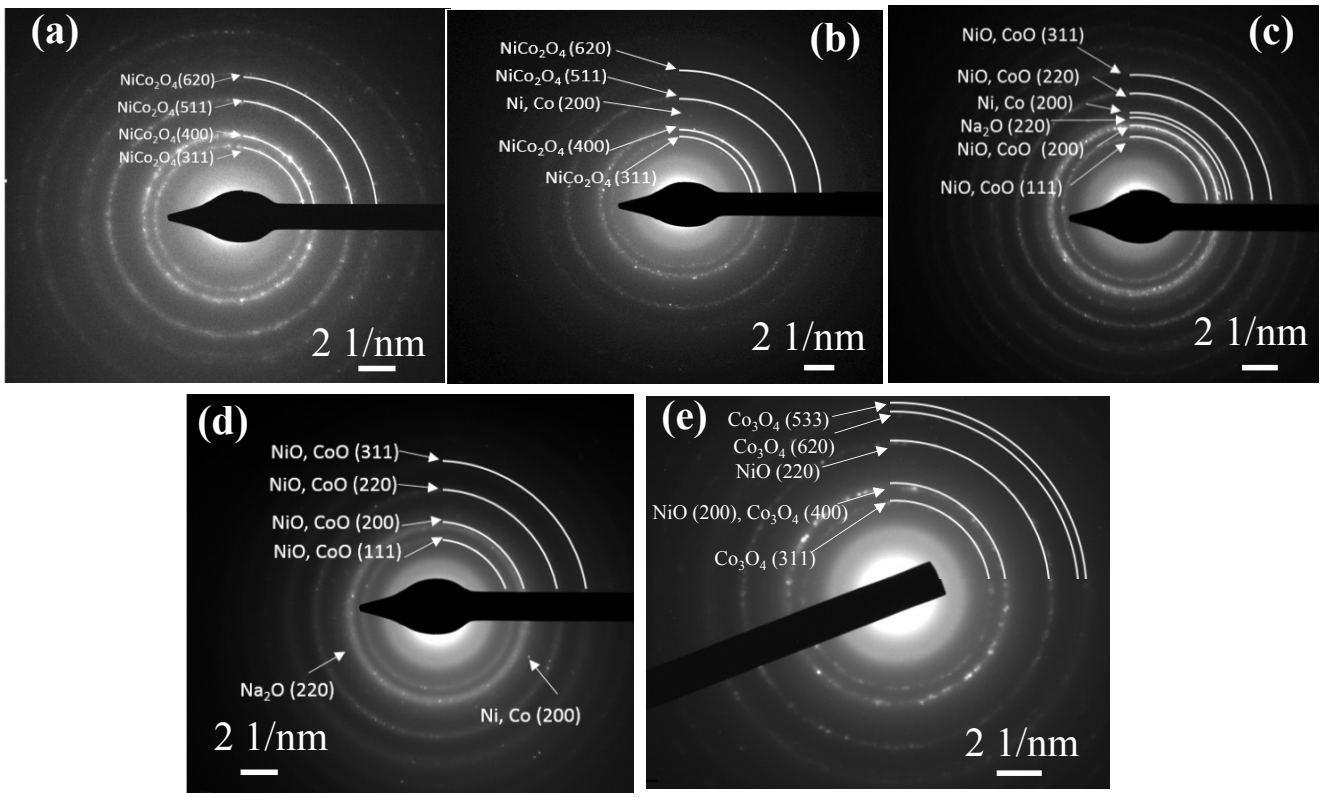

Figure 5.7 *Ex-situ* TEM SAED patterns of (a) pristine NCO, (b) D-0.7V, (c) D-0.005V, (d) C-1.2V, and (e) C-2.5V.

On the basis of the *ex-situ* XRD and TEM analysis results, the sodium-ion storage mechanism of NCO in a sodium half-cell during charge/discharge are summarized below:

In the first discharge:

$$NiCo_2O_4 + 8Na^+ + 8e \rightarrow Ni + 2Co + 4Na_2O$$

In the first charge:

$$Ni + 2Co + 3Na_2O \rightarrow NiO + 2CoO + 6Na^+ + 6e$$

$$2CoO + \frac{2}{3}Na_2O \rightarrow \frac{2}{3}CO_3O_4 + \frac{4}{3}Na^+ + \frac{4}{3}e$$

In summary, upon pre-sodiation, the NCO phase is converted to a nanocomposite consisting of Ni, Co an, Na_2O, which are the active materials in the Na_nNCO//AC NIC cell. The pre-sodiation provides more sodium ions to the NIC system and facilitates the conversion reaction taking place in the subsequent charge/discharge cycles. In addition, the small particle sizes of Ni and Co phases are kinetically favfavorabler the electrolyte diffusion as well as for fast interfacial electrochemical reactions,[205] thus minminimizing ectrode polarization and expanding the working voltage of the NIC cell, providing the device with a high energy density and a good power density.

5.4 Conclusions

Hollow NCO spheres with a chestnut shell morphology synthesized in a solvothermal system exhibited a specific capacity of 313 mAh g^{-1} at 1 A g^{-1} with a capacity retention of 85% after 100 cycles measured in a sodium half-cell. Pre-sodiation of the NCO electrode by galvanostatically discharging the sodium half-cell from an open circuit potential to 0.005 V is an excellent strategy to improve the electrode performance. A hybrid NIC fabricated with the pre-sodiated NCO as the anode and a commercial activated carbon as the cathode delivers energy and power densities of 120.3 Wh kg^{-1} and 10,000 W kg^{-1}, 5-9 times higher than a NIC based on the NCO electrode without pre-sodiation. The better performance of pre-sodiated $NiCo_2O_4$ electrode is because NCO phase is converted to metallic Ni, Co and Na_2O phases during pre-sodiation process. The small particle size of products (Ni and Co) is kinetically beneficial to the fast interfacial electrochemical reactions, while the Na_2O phase provides sodium ions.

5.5 Supplementary data

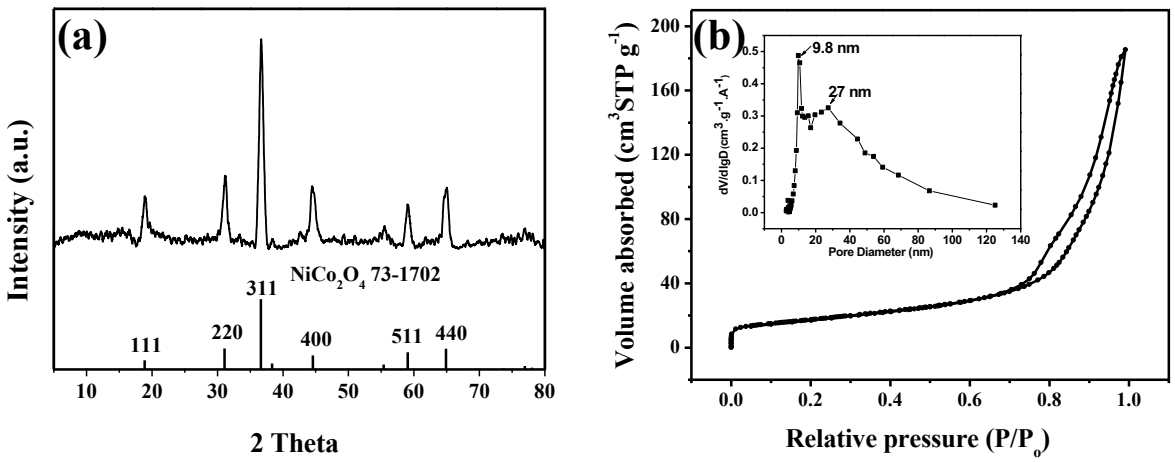

Figure S5.1 (a) XRD pattern and (b) Nitrogen adsorption-desorption isotherm with inserted corresponding pore size distribution of NCO.

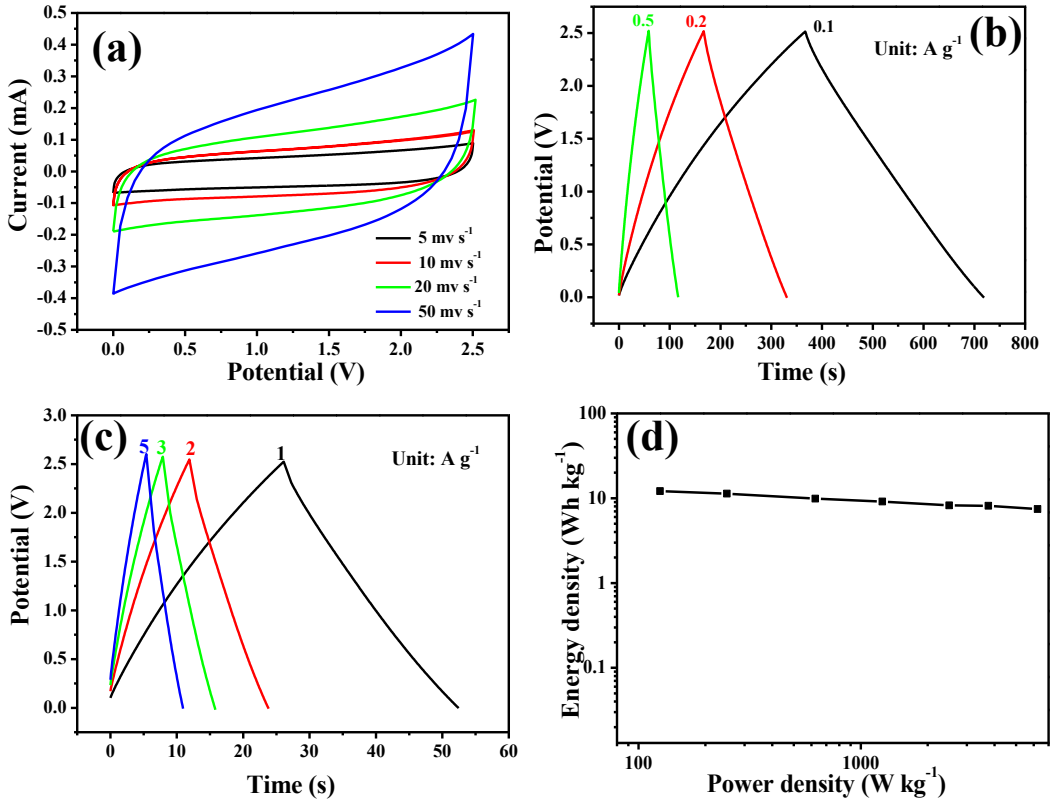

Figure S5.2 Electrochemical properties of the symmetric AC//AC supercapacitor: (a) CV plots, (b and c) GCD curves, (d) Ragone plot.

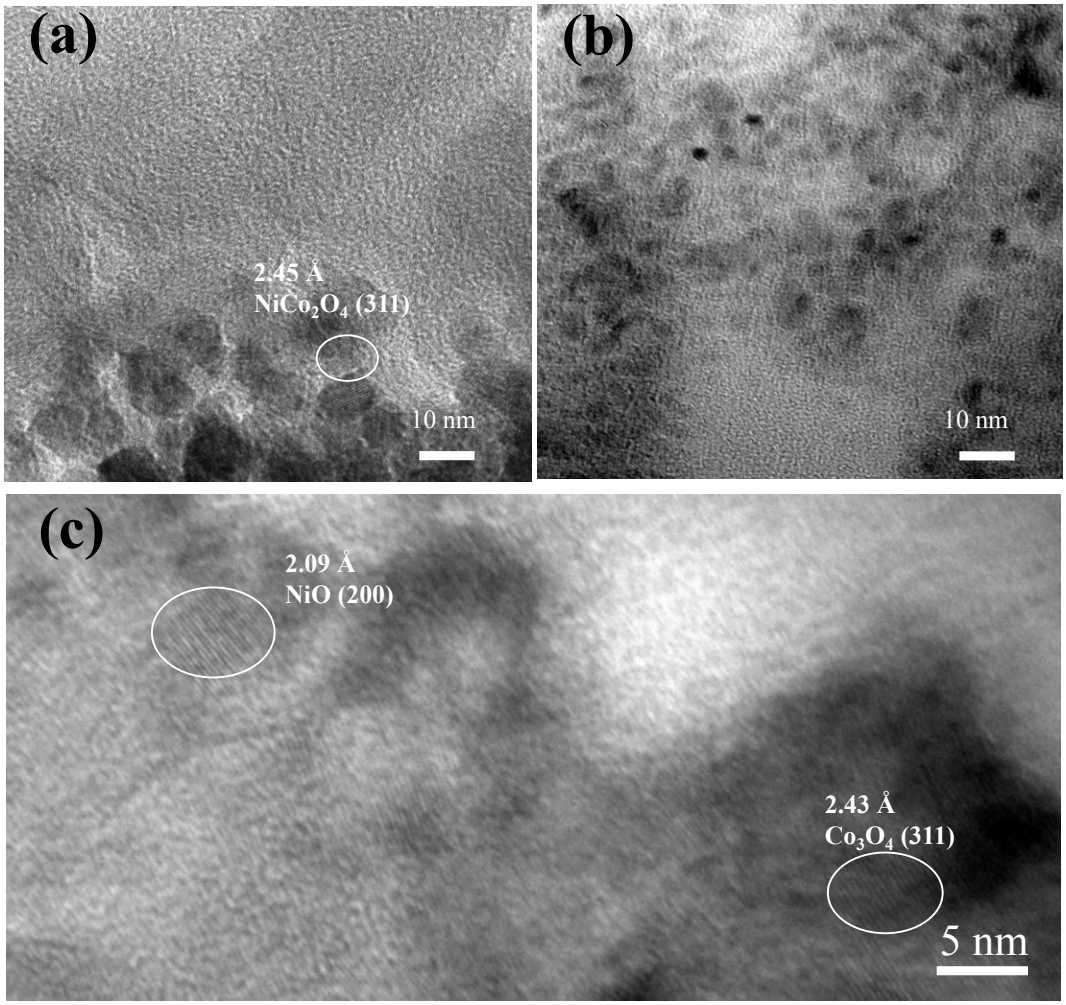

Figure S5.3 *Ex-situ* TEM images of NCO before (a) and after discharge to 0.005 V (b) and charge to 2.5 V (c).

Chapter 6 Encapsulation of $NiCo_2O_4$ in nitrogen-doped reduced graphene oxide sheets for sodium-ion capacitors

This chapter has been published in *Journal of Materials Chemistry A*, 2018, 6, 14146-14154.

Nickel cobaltite ($NiCo_2O_4$) with rich electroactive sites is a promising anode material for electrochemical capacitors and hybrid ion capacitors. However, this material is unstable due to large volume changes during repeated cycles. Here, we report an approach to improving the stability of $NiCo_2O_4$ against cycling by using a nitrogen-doped graphene framework to encapsulate $NiCo_2O_4$ particles. The graphene framework guarantees a good electronic conductivity and serves as a buffer to alleviate the volume changes of $NiCo_2O_4$. In a sodium half-cell, the composite electrode displayed a reversible capacity of about 450 mAh g^{-1} with a current rate of 0.1 A g^{-1} at the 100^{th} cycle. A sodium-ion capacitor configured with the composite as the anode and a commercial activated carbon as the cathode delivered an energy density of 48.8 Wh kg^{-1} at a power density of 9750 W kg^{-1} with a stable cycle life. The good electrochemical performance of the electrode material indicates that using nitrogen-doped graphene sheets to stabilize $NiCo_2O_4$ particles is a feasible approach towards developing high-performance anode materials for sodium-ion capacitors.

6.1 Introduction

Energy storage devices with both high energy and power densities are essential to the sustainable energy future.[65] While lithium-ion batteries (LIBs) have been widely used to power electronic devices, their power density is relatively low in comparison with, for example, supercapacitors (SCs).[42] Amatucci and co-workers firstly demonstrated a lithium-ion capacitor (LIC) with energy density higher than that of SCs and power density higher than that of LIBs.[206,207] This LIC stored energy via both non-faradaic process on the cathodic parts (capacitor-type) and faradaic process on anodic parts (battery-type). Despite the

successful commercialization of the LIC technology developed by Maxwell Technologies Inc,[18] the fast-growing demand for large-scale energy storage applications raises concerns over the limitation and cost of lithium resources.[208]

Sodium-ion capacitors (NICs) have attracted significant attention as an alternative for LICs because sodium is abundant in nature and cheaper than lithium.[185] One of the current grand challenges facing the development of the NIC technology is to find a suitable anode material.[92] Transition-metal oxides such as TiO_2,[35,45] Nb_2O_5,[28,29] $Na_2Ti_3O_7$,[30], V_2O_5,[19] Fe_3O_4,[120] and $NiCo_2O_4$,[48] have been demonstrated to be promising anode materials for NICs. For example, $NiCo_2O_4$ (NCO) holds a theoretical specific capacity as high as 890 mAh g^{-1}, yet the material is cost-effective and environmentally benign.[51] In one of our previous studies[48], it was found that NCO exhibited good charge storage capacity and rate performance. However, it was also found that being an anode material for sodium-ion storage, NCO experienced a large volume change due to phase changes during charge/discharge, leading to a poor stability against cycling.

The cycling stability of NCO can be improved by using carbon materials such as graphene,[56, 57] and carbon cloth[58]. Graphene that has high electrical conductivity, outstanding mechanical flexibility for buffering volume changes,[209–212] and good sodium-ion storage capacities[44], is particularly suitable for stabilizing NCO. In this work, NCO particles with a cubic morphology were synthesized using a solvothermal method. To improve the stability against cycling and the electronic conductivity, the NCO cubes were encapsulated in nitrogen-doped reduced graphene oxide (N-rGO) sheets. Experimental results showed that the composite electrode delivered a capability as high as 335 mAh g^{-1} at 2 A g^{-1} with a significantly improved stability against cycling. A hybrid NIC cell fabricated with the composite as the anode and a commercial activated carbon (AC) as the cathode showed both high energy and power densities with a long-term stability.

6.2 Experimental section

6.2.1 **Materials synthesis**

Synthesis of graphene oxide (GO):

The GO used in this work was synthesized from natural graphite using a modified Hummers method.[213,214] The atom percentage of oxygen and carbon in this GO was about 31.1% and 68.9%, respectively.

Synthesis of $NiCo_2O_4$ (NCO):

NCO particles with a cubic morphology were synthesized using the solvothermal method. In brief, 2 mmol of $Co(NO_3)_2 \cdot 6H_2O$, 1 mmol of $Ni(NO_3)_2 \cdot 6 H_2O$ and 3.6 g urea were dissolved in a mixture of 45 mL ethylene glycol plus 9 mL water. Next, 182 mg NaOH was added under stirring. Then, the mixture was transferred to a Teflon-lined stainless steel autoclave and heated at 120 ^oC for 10 h. The solid product was collected by centrifugation and washed with distilled water and ethanol, and dried in an oven at 80 ^oC. The solid was then thermally treated at 350 ºC in air for 2 h at a heating rate of 1 $^oC\ min^{-1}$ to obtain NCO.

Preparation of NCO@N-rGO composite:

The obtained NCO was first modified using poly (diallydimethylammonium chloride) (PDDA) to change the surface chemistry of the NCO particles. Briefly, 50 mg of NCO was added to 40 mL de-ionised water, followed by adding 1 g of PDDA under continuously magnetic stirring. The PDDA-modified NCO was obtained after centrifugation and washing with de-ionised water. Then, the PDDA-modified NCO was dispersed in 5 mL of de-ionised water to form a dispersion. This dispersion was added into 10 mL of aqueous GO suspension (0.8 $mg \cdot mL^{-1}$) under stirring at pH = 4 to form a precipitate, which is designated as NCO@GO. Finally, NCO@GO was dispersed in a mixture of 500 mg urea in 10 mL of aqueous GO suspension (0.8 $mg\ mL^{-1}$). The mixture was transferred into a Teflon-lined stainless steel autoclave and hydrothermally heated at 120 ºC for 4 h. The solid product was filtrated off and freeze-dried, followed by annealing at 350 °C for 2 h in a nitrogen atmosphere to obtain a sample, which is designated as NCO@N-rGO.

For comparison purpose, a nitrogen-doped rGO sample was prepared by reducing GO using the hydrothermal method in the presence of urea and further annealing at 350 °C for 2 h in a nitrogen atmosphere. This sample is denoted as N-rGO.

6.2.2 **Materials Characterization**

XRD patterns were collected on a Bruker D8 X-ray diffractometer with Ni-filtered Cu Kα radiation (λ = 1.54056 Å, 40 kV, 30 mA) at a scan rate of 2 º min^{-1}. FESEM (JEOL 7001) and TEM (JEOL2100) were used to characterize the morphology of samples. XPS spectra was acquired on a Kratos Axis ULTRA X-ray photoelectron spectrometer with a 165 mm hemispherical electron energy analyzer and a monochromatic Al Kα (1486.6 eV) radiation at 225 W (15 kV, 15 mA). TGA was conducted in air from room temperature up to 600 ^{o}C at a heating rate of 5 ^{o}C min^{-1} using a Perkin-Elmer STA 6000.

6.2.3 **Electrochemical measurements**

Electrodes were prepared by mixing 70 wt.% of an active material, 20 wt.% of an electrical conductor (carbon black), and 10 wt.% of a binder (carboxymethyl cellulose, CMC) in de-ionized water to form a slurry, which was subsequently coated on a current collector (copper foil for NCO, NCO@N-rGO and N-rGO and an aluminium foil current collector for AC, respectively). The AC exhibits a specific area of 1200 m^2 g^{-1}, provided by AC Technologies Pty Ltd, Australia. After the electrodes were dried at 60 ^{o}C overnight in a vacuum oven, they were punched into circular discs with a diameter of 1 cm. The half and full cell tests were conducted using 2032-type coin cells with GF/C glass fiber (Whatman, USA) as the separator and 1 M $NaPF_6$ dissolved in diethylene glycol dimethyl ether solvent as the electrolyte. The amount of electrolyte for each cell was 200 uL. The electrolyte preparation, the coin cell assemblies and disassembles were all performed in an Argon filled glovebox.

A sodium half-cell was assembled by using the above-prepared electrode and Na metal plate as the electrodes. The mass loading of the NCO, NCO@N-rGO and N-rGO electrodes was about 1 mg cm^{-2}. A full NIC cell was fabricated with NCO@N-rGO as the anode and a commercial AC (a specific area of 1200 m^2 g^{-1} from AC Technologies Pty Ltd, Australia) as the cathode. Before assembling the full cell, The NCO@N-rGO electrode was pre-cycled 3 times at 0.1 A g^{-1} in a sodium half-cell and then sodiated to 0.1 V versus Na^+/Na. To balance the charge density of the two electrodes, the mass loading of the cathode and the anode was about 3.2 mg cm^{-2} and 1 mg cm^{-2}, respectively.

6.3 Results and discussion

Scheme 6.1 schematically illustrates the procedure for preparing the composite material, NCO@N-rGO. The solvothermally synthesized NCO particles were modified with PDDA to render the surface to be positively charged at pH < 8 as is seen from the zeta potential profile shown in Figure S6.1 (Supplementary data 6.5). GO is negatively charged at a wide range of pH. Therefore, the PDDA-modified NCO interacted strongly with GO sheets via electrostatic forces at pH 4, enabling the latter to encapsulate the former to form a precipitate (NCO@GO), which was further hydrothermally treated in a urea-containing GO dispersion. This treatment not only guaranteed a well encapsulation of the NCO particles by GO sheets, but also enabled cross-link between GO and NCO@GO via oxygen-containing groups.[65] Simultaneously, GO was reduced and doped with nitrogen by urea.[215] After freeze-drying and thermal treatment, NCO@N-rGO was obtained.

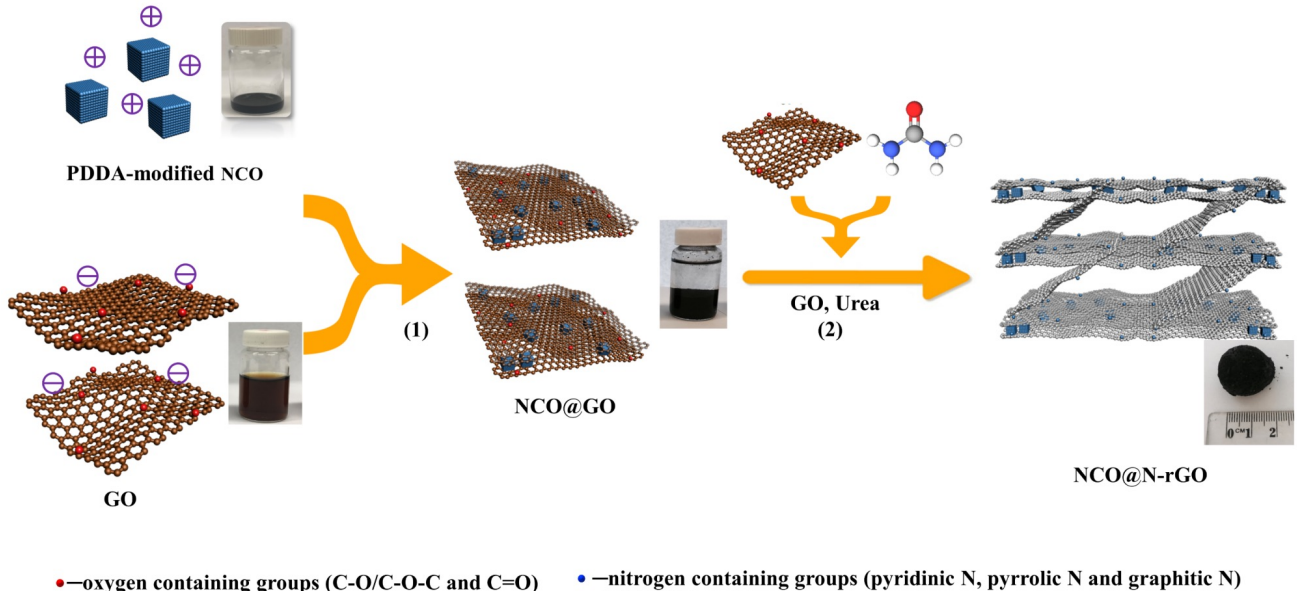

Scheme 6.1. Schematic and photograph illustration of the preparation of NCO@N-rGO: (1) formation of NCO@GO via electrostatic attraction, (2) dispersing NCO@GO in a urea-dissolved GO suspension for hydrothermal treatment to obtain NCO@N-rGO.

Figure 6.1 shows the SEM and TEM images of sample NCO@N-rGO, along with elemental mapping results. A porous graphene framework can be seen from the SEM image in Figure 6.1a. NCO cubes (as confirmed by the SEM images in Figure S6.2) with sizes between 200

and 250 nm were encapsulated in the porous graphene framework (Figures 6.1b and c). This structure was further confirmed by the TEM image in Figure 6.1d, which shows that NCO cubes were intimately encapsulated in a few-layer graphene substrate with wrinkles surrounding them. Such a close contact guarantees a good electronic contact between NCO and N-rGO. The HAADF-STEM image and elemental mapping results of NCO@N-rGO (Figure 6.1e) confirmed the NCO cubes were encapsulated in N-rGO with Ni, Co, and O, while N and C were well distributed over all scope, suggesting that N heteroatoms are homogeneously doped in the graphene sheets.

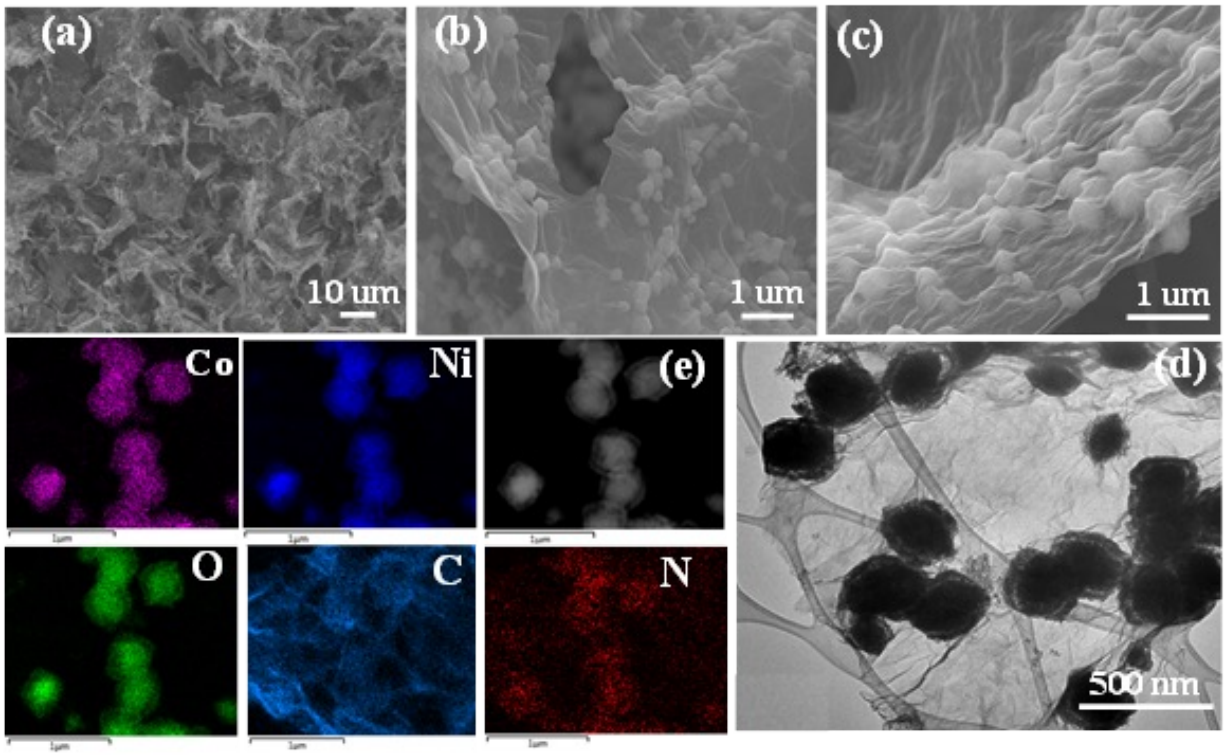

Figure 6.1 The morphology and microstructure characterization of NCO@N-rGO: (a-c) SEM images at different magnifications, (d) TEM image, (e) HAADF-STEM image and elemental mapping results.

Figure 6.2a shows the XRD pattern of sample NCO@N-rGO. All the sharp diffraction peaks can be indexed to crystalline NCO (JCPDS 73-1702). The small diffraction hump appearing in the range of 22-28 degrees two theta is attributed to stacked graphene sheets as confirmed by the XRD pattern of sample N-rGO in Figure S6.3, which depicts the XRD patterns of samples NCO, N-rGO, and GO. For N-rGO sample, a broad peak in the two theta ranges of 22-28 degree can be seen, but the peak at 11.2 degrees two theta

disappeared, indicating the GO sheets were reduced after the hydrothermal treatments, leading to sheet stacking. The TGA profile shown in Figure S6.4 showed that sample NCO@N-rGO contained 16.1 wt.% graphene, which was lower than the graphene content of previously reported NCO/graphene composites.[216–218]

Figure 6.2b shows the wide-scan XPS survey spectrum of sample NCO@N-rGO. The binding energies of 399.8, 530.8, 779.8 and 854.8 eV corresponded to N 1s, O 1s, Co 2p and Ni 2p, respectively, with the reference binding energy at 284.8 eV for the C 1s peak. Figs. 2c and 2d present the high-resolution XPS spectra of Ni 2p and Co 2p of NCO@N-rGO, respectively. The Ni 2p and Co 2p spectra were deconvoluted with two peaks assigned to Ni^{2+}/Ni^{3+} and Co^{2+}/Co^{3+} respectively, with two satellite peaks as well. This matched well with previously reported XPS spectra of Ni 2p and Co 2p in NCO.[51] Figure 6.2e shows the high-resolution XPS spectrum of N 1s, which can be resolved into three components centered at 398.2, 399.6 and 401.6 eV, representing the pyridinic, pyrrolic and graphitic types of N atoms, respectively. In addition, the XPS analysis revealed that the N-doping level was 4.05 at.% in N-rGO. Doping N in graphene not only enhances its electronic conductivity, but also improves the wettability between graphene and the organic electrolyte.[219] Figure 6.2f compares the C 1s high-resolution XPS spectra of GO and NCO@N-rGO; the dramatic loss of oxygen-containing functional groups (C-O/C-O-C and C=O) further confirmed the reduction of GO. Therefore, the XRD and XPS result confirmed the integration of NCO and N-rGO, the reduction of GO and the successful N-doping in GO.

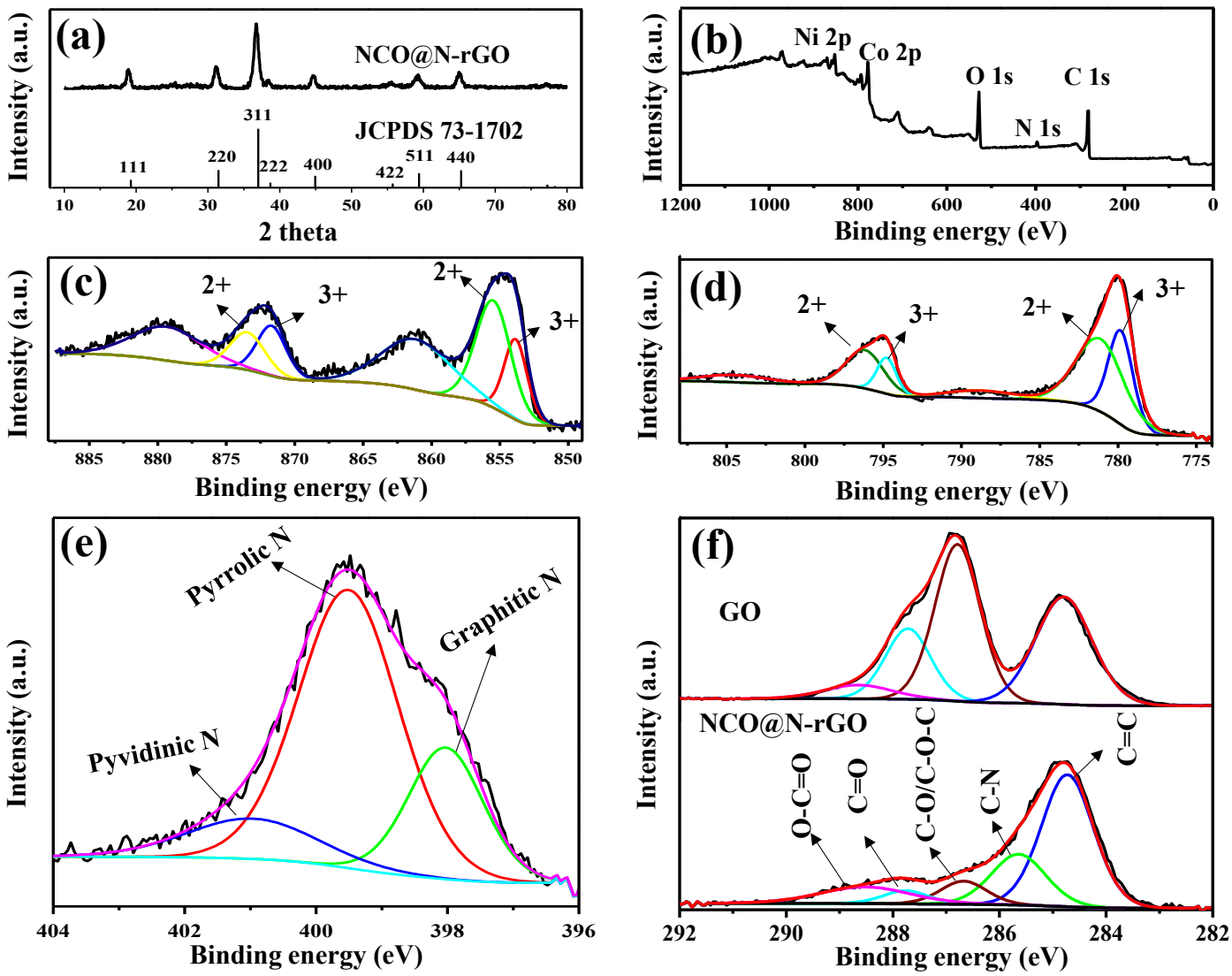

Figure 6.2 (a) XRD patterns of NCO@N-rGO and the standard NCO (JCPDS card no. 73-1702). (b) XPS survey of NCO@N-rGO. (c, d and e) High-resolution XPS spectrum of Ni 2p, Co 2p and N 1s for NCO@N-rGO, respectively. (f) High-resolution XPS spectrum of C 1s for NCO@N-rGO and GO.

6.3.1 **Electrochemical performance in sodium half-cells**

Figure 6.3a shows the GCD profiles of sample NCO@N-rGO at the potential range between 0.1 and 3.0 V versus Na^+/Na at current densities of 0.1 to 5.0 A g^{-1}. As previously reported in our study, the NCO phase reacted with sodium ions to produce Ni, Co and Na_2O phases during discharging, then transformed into NiO and Co_3O_4 phases during charging, corresponding with evident voltage plateaus in the GCD profiles.[48] However, in this work, NCO@N-rGO produced GCD profiles without a noticeable plateau at all current densities.

This might imply that the reaction mechanism between sodium ions and NCO@N-rGO not only involves in phases conversion but also has a large contribution of surface capacitive behavior.

Figure 6.3b compares the rate performance of NCO@N-rGO and NCO. Both electrodes exhibited continuously decreasing capacities at the first few cycles. The capacities loss can be attributed to the formation of solid electrolyte interphase (SEI) on the electrode surface, leading to an irreversible reaction of sodium ions during the discharge process. As the current rate steadily increased, the difference in rate capability between these two electrodes became obvious. Specifically, electrode NCO@N-rGO delivered capacities of 439, 420, 388, 378, 358, 335 and 308 mAh g^{-1} at current rates of 0.05, 0.1, 0.2, 0.5, 1, 2 and 5 A g^{-1}, respectively. When the current rate was reversed back to 0.05 A g^{-1}, the electrode capacity was about 438 mAh g^{-1}, very close to 439 mAh g^{-1}. In contrast, the capacity of electrode NCO dropped sharply in the first 10 cycles, and the specific capacities in the subsequent cycles at different current rates were much lower than those of NCO@N-rGO. The observed high rate capability of electrode NCO@N-rGO is ascribed to the porous graphene framework providing a continuous pathway for both sodium ions and electron transfers.

The cycling stability of NCO@N-rGO was also much better than that of NCO as is shown in Figure 6.3c. Both electrodes were cycled using a current rate of 0.1 A g^{-1}. Despite the decay in the initial few cycles, the reversible capacity of electrode NCO@N-rGO exhibited a slowly increasing trend from the 8^{th} cycle, reaching to 452 mAh g^{-1} at the 100^{th} cycle. This capacity-increasing trend with cycling is most probably due to the activation of sodium transport sites in the electrodes (*e.g.*, nano-cavities between RGO sheets and edge-type sites).[214] For the NCO electrode, it showed a high specific capacity of 693 mAh g^{-1} at the 2^{nd} cycle. However, its rapid capacity fading resulted in a capacity of only 116 mAh g^{-1} at the 100^{th} cycle. For comparison, the performance of N-rGO was also measured and the data are included in Figure 6.3c. Electrode N-rGO contributed a reversible specific capacity of 205 mAh g^{-1} at the 100^{th} cycle, which was higher than that of a rGO electrode reported previously.[64] This is because the nitrogen functional groups are highly active which promote the electrolyte adsorption and diffusion.[220,221]

The NCO@N-rGO electrode also displayed a long cycling performance as shown in Figure 6.3d. After activated at 0.1 A g^{-1} for the first few cycles, NCO@N-rGO remained the capacity of 309 mAh g^{-1} at 1 A g^{-1} at the 400th cycle with a capacity retention of 86.3%. Such a good cycling performance of the NCO@N-rGO sample was attributed to the structure robustness of the N-rGO sheets, which provided space for accommodating the volume changes of the NCO particles during charge/discharge as schematically illustrated in Figure 6.3e. Meanwhile, the high electronic conductivity of N-rGO facilitated the electron and sodium ions transport, leading to the observed good cycling and rate performance. Moreover, the coulombic efficiency of NCO@N-rGO electrode was higher than 96% after the 2nd cycle at both current densities of 0.1 A g^{-1} (Figure 6.3c) and 1 A g^{-1} (Figure 6.3d).

Figure 6.3f shows the Nyquist plots of electrodes of NCO@N-rGO and NCO, along with a fitted circuit. Both plots showed a single semicircle in the high-to-medium frequency region and the charge-transfer kinetics at the electrode/electrolyte interface (R_{ct}), as well as a slope in the low frequency region which stands for the diffusive Warburg impedance (W). R_c is the resistance of the electrolyte. According to the fitting results as listed in Table. S6.1, NCO@N-rGO showed a smaller resistance of R_{ct} (117 Ω) than that of NCO (264 Ω), further demonstrating that N-rGO indeed improved the electron transport kinetics of the electrode materials.

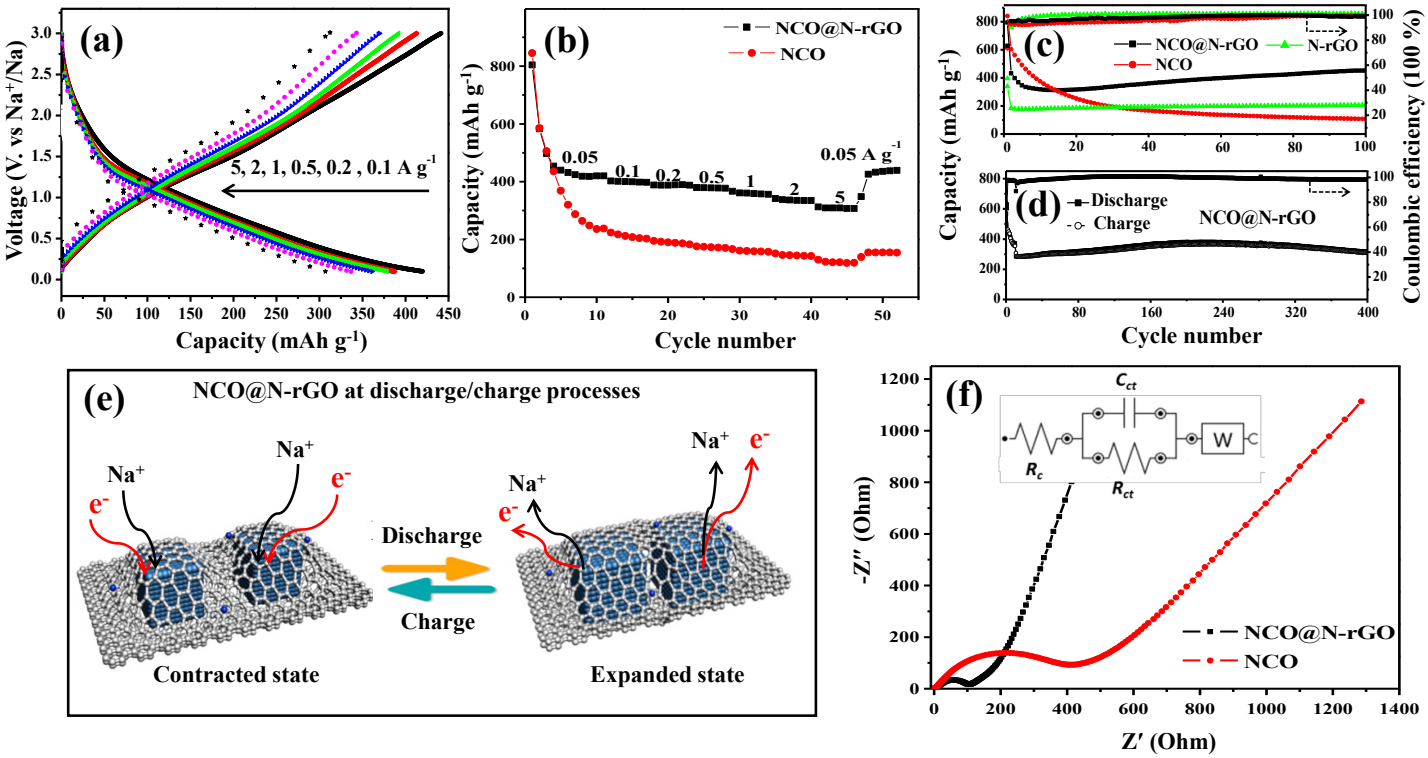

Figure 6.3 (a) GCD profiles of NCO@N-rGO at various current densities from 0.05 to 5.0 A g^{-1}. (b) Rate performance of NCO and NCO@N-rGO electrodes. (c) Cycling performance combined with coulombic efficiency of NCO@N-rGO, NCO and N-rGO electrodes at 0.1 A g^{-1}. (d) Cycling performance combined with coulombic efficiency of NCO@N-rGO at 1 A g^{-1}. (e) A schematic illustration of the NCO@N-rGO electrode reacting with sodium ions upon charge/discharge, showing the function of graphene sheets for stabilizing NCO crystals and improving the electronic conductivity. (f) Nyquist plots of NCO and NCO@N-rGO electrodes.

6.3.2 **Electrokinetics study**

The electrokinetics of electrode NCO@N-rGO was studied using the cyclic voltammetry (CV) technique and the results are shown in Figure 6.4a. The main cathodic peak is labeled with C1 and the second small and broad cathodic peak is labeled with C2. The two anodic peaks are labeled with A1 and A2, respectively. The energy storage contributions from the surface capacitive and diffusion-controlled faradic processes can be differentiated from the parameters in the following power-law kinetics [205,222]:

$$i = av^b \qquad (6\text{-}1)$$

where *i* is the current (A), *v* is the scan rate (mV s^{-1}), *a* and *b* are variables values. By plotting log (|*i*|) versus log (*v*), the *b* value can be derived from the slope of the liner line. Generally, b-value of 0.5 indicates the reaction is a diffusion-controlled sodium ions faradic process, while a value of 1.0 indicates a capacitive charge storage (here is pseudocapacitance and double-layer capacitance taking place in the surface/interfaces of NCO@N-rGO).

Figure S6.5a shows the plog of log (|*i*|) versus log (*v*) for anodic (A1 and A2) and cathodic peaks (C1 and C2), The b-value of C1 was 0.58, indicating diffusion-controlled contribution was more pronounced, while the b-value of C2, A1 and A2 were 0.88, 0.72 and 0.63 respectively, indicative of combined capacitive and diffusion-controlled sodium-ion storage. More specifically, we quantitatively separated the contributions from surface capacitive and diffusion-controlled sodium- ion storage by using the following equation between current (*i*) and scan rate (*v*) [205]:

$$i = k_1 v + k_2 v^{1/2} \qquad (6\text{-}2)$$

where $k_1$and k_2 are variables values. Here, $k_1 v$ and $k_2 v^{1/2}$ represent the capacitive and faradic elements, respectively. Through dividing both sides of the *eq (6-2)* by the square root of the scan rate and plot the $i/v^{1/2}$ versus $v^{1/2}$, a straight line with a slope of k_1 and an intercept of k_2 was obtained, which provides quantitative information regarding the capacitive and diffusion-controlled mechanisms (see Figure 6.4b). Based on this quantitative analysis, we divided the electrochemical reactions into four regions as shown in Figure S6.5b and Table. S6.2. It is clear that the diffusion-controlled redox reaction occurred primarily in region C1*, while other regions (C2*, A1*, A2*) involved in redox reaction combined with a large contribution of capacitive reaction. The total ratios of the capacitive contribution to the diffusion-controlled contribution at different scan rate were calculated and shown in Figure 6.4c. At a scan rate of 1 mV s^{-1}, 44.69% of the stored charge is attributed to the capacitive process. Based on the quantitative contributions of capacitive storage for different electrochemical regions in Table S2, the surface capacitive charge can be roughly outlined by the shadow area as shown in the Figure 6.4d. Overall, capacitive behavior provides a large contribution (39.6%-46.8% from 0.2-1.2 mV s^{-1}) to the charge storage in the NCO@N-rGO electrode, allowing ultrafast uptake and release of sodium ions with small degradation of the active material.

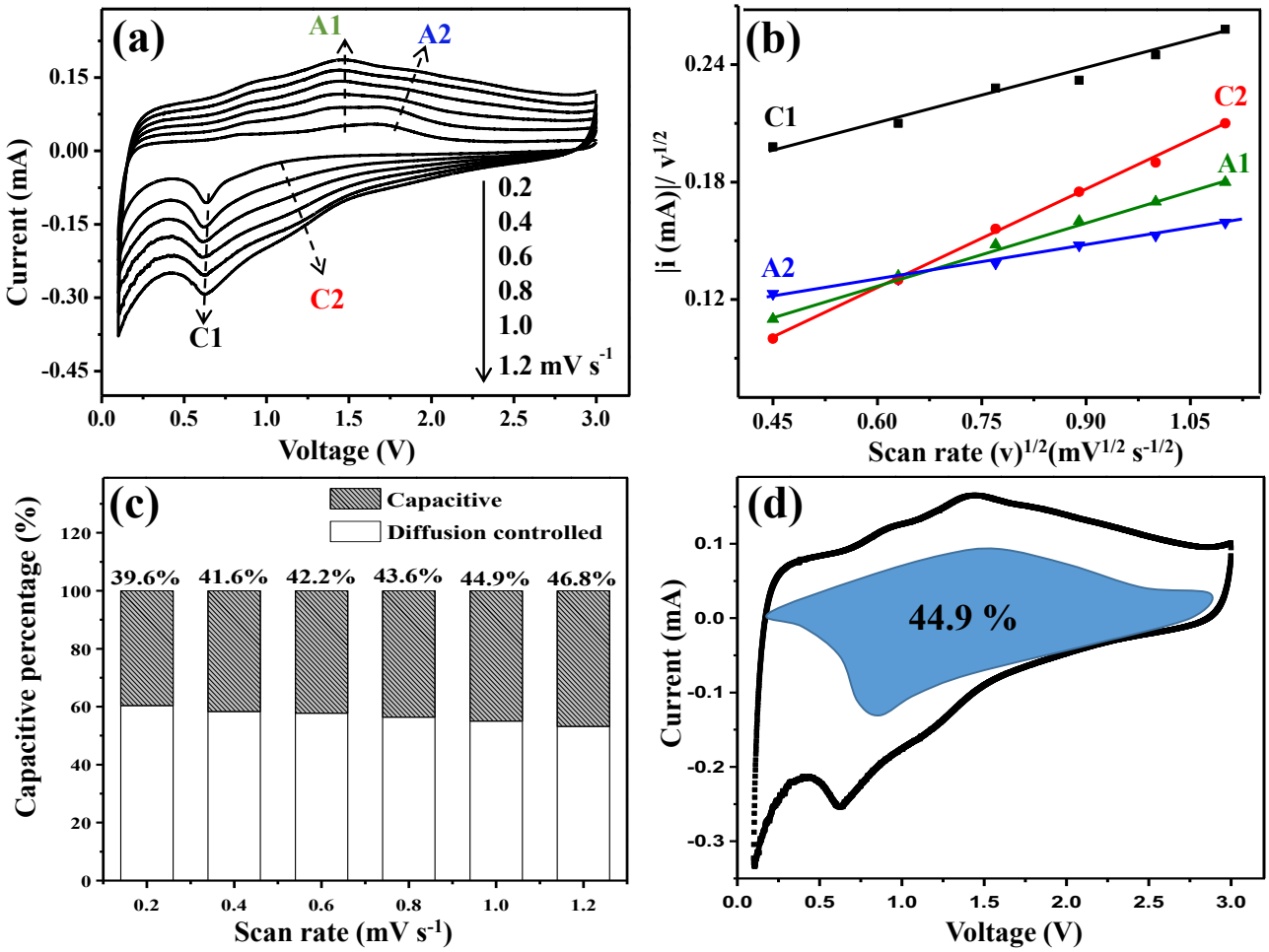

Figure 6.4 Kinetics analysis of the electrochemical behavior towards sodium ions for NCO@N-rGO electrode. (a) CV curves at various sweep rates from 0.2 to 1.2 mV s^{-1}. (b) Peak current dependence on the scan rate, used to determine the capacitive and intercalation contributions to energy storage. (c) Quantitative contributions of surface capacitive and diffusion-controlled faradic reactions to sodium-ion storage. (d) CV curve of NCO@N-rGO with separation between total current (solid line) and surface capacitive current (shaded regions) at 1 mV s^{-1}.

6.3.3 **Electrochemical performance in a full sodium-ion capacitor cell**

A full cell of NIC was assembled with NCO@N-rGO as the anode and a commercial AC as the cathode to evaluate the electrochemical performance of the composite electrode. The working potential window of each electrode was determined by using the CV technique in a half-cell configuration (top of Figure 6.5a). The AC electrode stored energy (PO_6^- anion) via

an electric double layer mechanism up to 4 V versus Na/Na^+ during charge. To avoid electrolyte decomposition and other possible side reactions, the working voltage window of the full NIC cell was set between 0.1 and 3.8 V (bottom of Figure 6.5a). Figure 6.5b presents the GCD profiles at current rates ranging from 0.2 A g^{-1} to 5 A g^{-1}. The energy and power densities are presented in the inset of Figure 6.5c. Specifically, the NIC delivered an energy density of 92.8 Wh kg^{-1} at a power density of 390 W kg^{-1}. Even at a high power output of 9750 W kg^{-1}, it showed an energy density of 48.8 Wh kg^{-1}. Figure 6.5d shows the cycling stability of the NIC at 2 A g^{-1}. The energy density decreased in the first 500 cycles, and retained over 83.7% of its initial energy density after 4000 cycles. Compared in Figure 6.5d are the Ragone plots of the NIC cell fabricated in this work with some representative graphene-based NIC devices. The NIC device reported in this work exhibited a higher energy density at the same power density when compared to those of previous graphene-based NICs, such as TiO_2@graphene,[35] Nb_2O_5@C/rGO,[28] $Na_2Ti_3O_7$@GF,[223] SnS_2/Graphene-CNT,[47] and $NaTi_2(PO_4)_3$/rGO,[37], further demonstrating that using nitrogen-doped graphene sheets to stabilise NCO particles is a feasible approach towards developing high performance NICs.

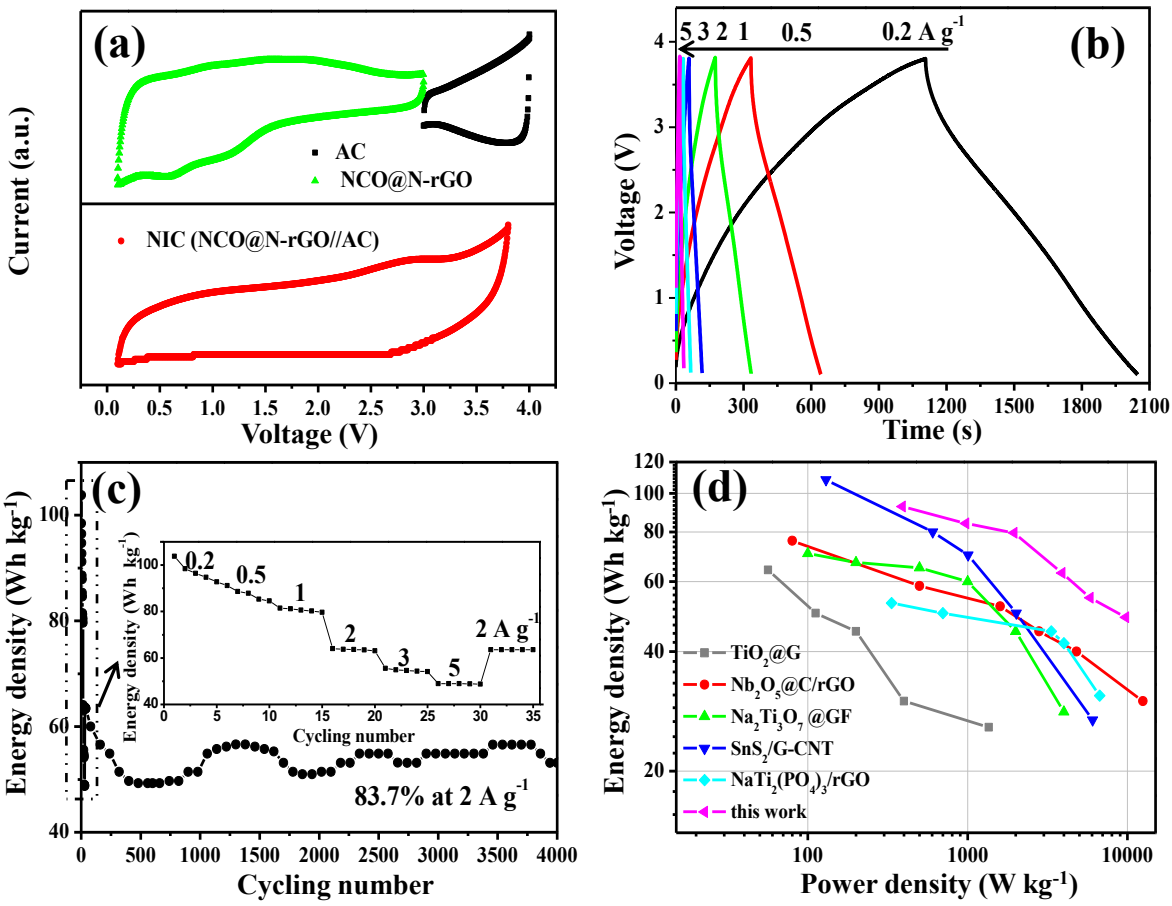

Figure 6.5 (a) CV curves of NCO@N-rGO and AC in half cells (top) and full cell of NIC (bottom) at 5 mV s^{-1}, indicating the voltage window of the full cell from 0.1 to 3.8 V. (b) GCD profiles at 0.2-5 A g^{-1}. (c) The long-term cycle life of NIC at 2 A g^{-1}, with inset of rate capability of the NIC at various current densities from 0.2 to 5 A g^{-1}. (d) Ragone plots in comparison with representative graphene-based NICs in literature.

The good electrochemical performance of the NCO@N-rGO material can be interpreted as follows: (1) the close contact between NCO particles and N-rGO surface guarantees a good electronic contact between them, which was beneficial for the electrons transfer between these two components, (2) N-rGO framework serves as a buffer to accommodate the volume change during charge/discharge, (3) the combined capacitive and diffusion-controlled sodium-ion storage mechanism is beneficial to the good rate capability and long-term cycling stability.

6.4 Conclusions

Encapsulation of NCO particles in nitrogen-doped graphene framework is a feasible approach to improving the electrochemical performance of NCO. The robust architecture in combination with the fast electron transport pathways, and the large contribution of surface capacitive charge storage are the primary factors contributing to observed good sodium-ion storage properties of the composite material with the high-rate capability and cycling stability. The composite electrode delivered a reversible capacity of 450 mAh g^{-1} at the 100th cycle at a current rate of 0.1 A g^{-1}. By coupling with a commercial AC as the cathode, a full NIC exhibited an energy density as high as 92.8 Wh kg^{-1} at a power density of 390 W kg^{-1}, or as high as 48.8 Wh kg^{-1} at a power output of 9750 W kg^{-1}. Moreover, over 83.7% of the energy density was retained after 4000 cycles. All of these features manifest the NCO@N-rGO composite material a promising anode for sodium-ion based electrochemical energy storage devices.

6.5 Supplementary data

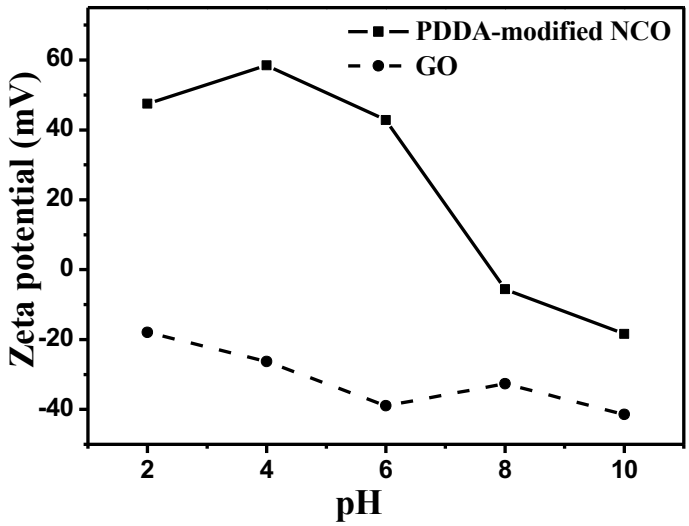

Figure S6.1 Zeta potential profiles of PDDA-modified NCO and GO in the pH range between 2 and 10.

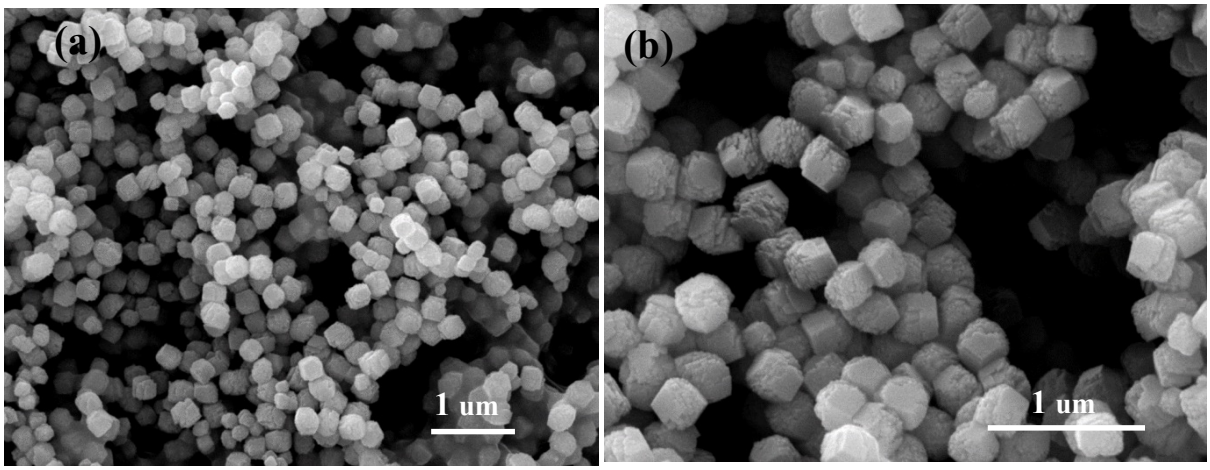

Figure S6.2 SEM images of NCO particles.

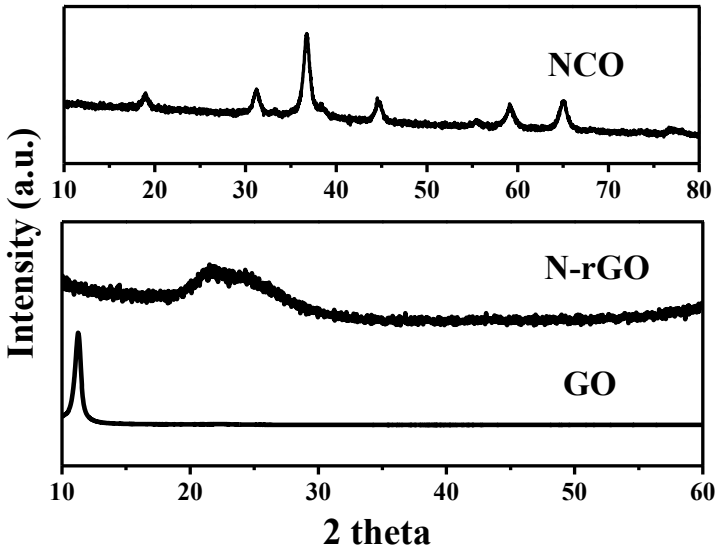

Figure S6.3 XRD patterns of GO, N-rGO and NCO.

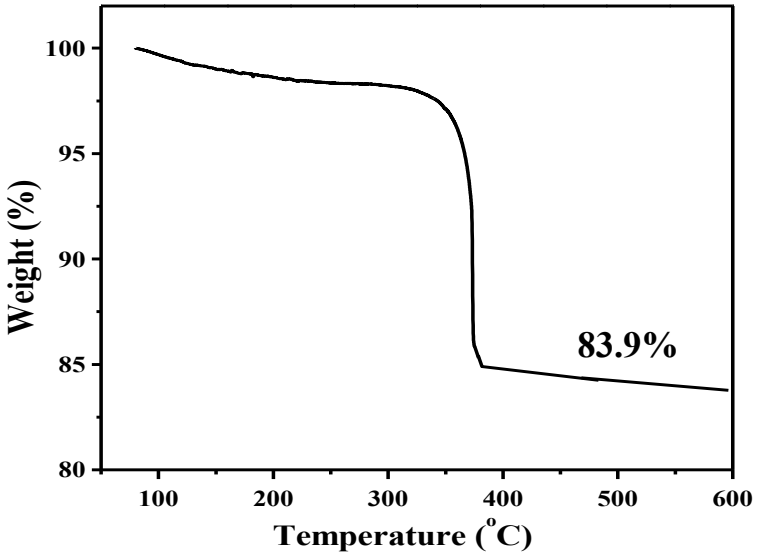

Figure S6.4 TGA of NCO@N-rGO.

Table S6.1 Fitting results of the EIS spectra in Figure 6.3f using the inserted equivalent circuit.

Circuit element	NCO@N-rGO	NCO
R_c (Ω)	5.73	3.80
R_{ct} (Ω)	117	264
C_{ct} (nF)	690	902
W (mMho)	2.65	757

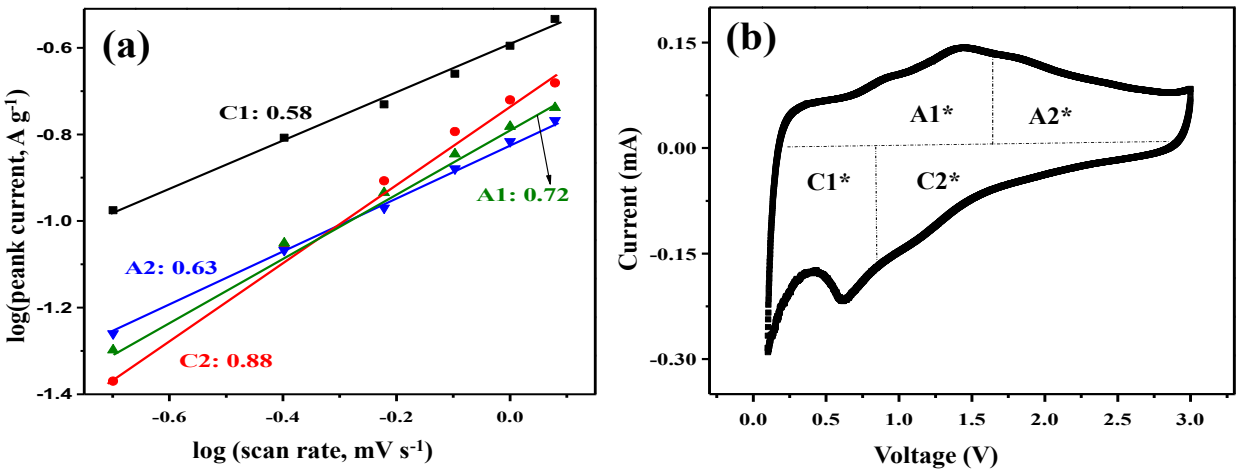

Figure S6.5 (a) b-values plotted as a function of potential for anodic and cathodic sweeps. (b) The electrochemical reactions were divided into four regions (A1*, A2*, C1*, and C2*).

Table S6.2 Quantitative contributions of capacitive sodium-ion storage for different electrochemical regions in Figure S6.5b.

Scan rate	A1*	A2*	C1*	C2*
0.2	33.47%	24.14%	3.95%	76.05%
0.4	41.57%	31.03%	5.50%	81.79%
0.6	46.56%	35.53%	6.65%	84.62%
0.8	50.16%	38.89%	7.60%	86.40%
1	52.94%	41.57%	8.42%	87.66%
1.2	55.20%	43.80%	9.16%	88.61%

Chapter 7 Three-dimensional nitrogen-doped holey graphene and transition-metal oxides composites for sodium-ion storage

This chapter has been published in *Journal of Materials Chemistry A*, 2019, DOI: 10.1039/C8TA09188A.

Nickel cobaltite (NCO) with rich electroactive sites is a promising anode material for sodium-ion storage. However, this material suffers from large volume change during charge/discharge, poor electron conductivity and severe aggregation of NCO nanoparticles. Here, we report an approach to improve the electrochemical performance of NCO nanoparticles by stabilizing them on three-dimensional (3D) nitrogen-doped holey graphene (N-HG), forming a NCO@N-HG composite material. The thin graphene sheets in the composite facilitate the electron transport and buffer the volume changes, while the interconnected 3D macroporous network with a pore size in several micrometers range, combined with the nanopores in the N-HG provide pathways for rapid ion transport. As expected, the composite showed high specific capacities, rate capability and cycling performance in NIBs. This approach was also extended to modify magnetite (Fe_3O_4) by synthesizing Fe_3O_4@N-HG composite. The good electrochemical performance of the electrode materials indicates that using N-HG to support NCO and Fe_3O_4 nanoparticles is an effective approach towards developing high-performance anode materials for sodium-ion storage.

7.1 Introduction

Sodium-ion storage including sodium-ion batteries (NIBs) and sodium-ion capacitors (NICs) are gaining fast growing attention as an alternative to lithium-ion storage because of the rich

abundance and low cost of sodium sources.[154,208] One of the current grand challenges of the sodium-ion storage technology is to find suitable anode materials with both high reversible capacities and long cycling life.[109,121] Transition-metal oxides (TMOs) such as TiO_2,[224,225] Nb_2O_5,[226,227] $NiCo_2O_4$,[48,56] and Fe_3O_4,[228–230] have been demonstrated to be promising anode materials for sodium-ion storage. However, the TMOs suffer from large volume change and sluggish kinetics of both ion and electron transport, as well as severe aggregation for TMOs nanoparticles (NPs), resulting in poor rate performance and cycling stability.[171,231] One strategy for solving these problems is to combine TMOs with carbon materials, such as graphene, to prepare composite electrodes.[56,57,228,232] While graphene is an excellent carbon material, graphene sheets tend to stack or agglomerate during electrochemical reactions, leading to blockage of some ion transport pathways.[66,67]

Using three-dimensional (3D) porous graphene aerogels with 3D ion diffusion channels to support TMOs has been shown to be a more effective approach to fabricating TMO-graphene composite electrode materials.[65,228,232–234] However, ion transport across the basal plane of individual two-dimensional (2D) graphene sheets has been a great challenge.[68] Introducing nanoholes in graphene sheets is regarded as a good approach to solve this problem. Zhao *et al.*[69] reported that graphene can be etched by nitric acid to obtain holy graphene (HG). Jiang *et al.*[70] reported that potassium hydroxide can also be used to create holes for preparing HG. The HG in the above two work exhibited a significantly improved rate capability with an excellent cycling stability as anode for lithium-ion batteries. Later, Xu *et al.*[235] reported that graphene can be etched by using a more environmentally friendly agent, namely hydrogen peroxide (H_2O_2) to obtain HG, which showed efficient capacitive energy storage. Recently, Sun and co-workers[68] prepared a HG by etching graphene in the presence of H_2O_2, which was then used as a conductive scaffold for Nb_2O_5 to form a 3D architecture electrode. The HG greatly improved ion access to the Nb_2O_5, leading to an ultrahigh-rate lithium-ion storage with a capacity of 75 mAh g^{-1} at 100 C. On the other hand, nitrogen (N) doping is an effective approach to further improving the electron conductivity and wettability of carbon materials.[65,219] Therefore, it can be expected that constructing a 3D porous architecture consisting of nitrogen-doped HG (N-HG) and the TMOs could significantly facilitate electron and sodium ion transport throughout the entire architecture.

It has been reported that nickel cobaltite (NCO) [48,54,56] and magnetite (Fe_3O_4)[228–230,236] are typical TMOs with rich electroactive sites are promising electrode materials for electrochemical energy storage due to their low cost, abundance in nature, and high theoretical specific capacities in NIBs (~ 890 mAh g^{-1} for NCO and 925 mAh g^{-1} for Fe_3O_4). However, their severe volume change during electrochemical cycling, inferior electric and ionic conductivity, and severe aggregation of NPs are critical issues that must be solved before such TMOs can find practical applications. In this work, N-HG was used to modify NCO and Fe_3O_4 nanoparticles by forming 3D porous N-HG supported NCO and Fe_3O_4 composites, which were designated as NCO@N-HG and Fe_3O_4@N-HG, respectively. The thin graphene sheets in both composites facilitate the electron transport and buffer the volume changes. In addition, the interconnected 3D macroporous network with a pore size in several micrometers range, combined with the nanoporous channels in the N-HG provide pathways for rapid ion transport. As expected, the composites exhibited enhanced rate capabilities with specific capacities of 403 and 350 mAh g^{-1} for NCO@N-HG and Fe_3O_4@N-HG at a current rate of 1 A g^{-1}, respectively, and a stable cycling performance when used as anodes in NIBs. NICs configured with the composites as the anode and a commercial AC as the cathode delivered an energy density of 52 Wh kg^{-1} for NCO@N-HG, and 47 Wh kg^{-1} for Fe_3O_4@N-HG at power densities of 10, 000 W kg^{-1}.

7.2 Experimental section

7.2.1 **Materials synthesis**

Synthesis of graphene oxide (GO):

The GO used in this work was synthesized from natural graphite using the modified Hummers method as described elsewhere.[213]

Synthesis of holey GO (HGO):

The HGO was prepared by etching GO with H_2O_2 using a previously reported method.[68,237] Briefly, 40 mL of 2 mg mL^{-1} GO aqueous dispersion was mixed with 4 mL of 30% H_2O_2 aqueous solution under stirring. The mixture was heated at 100 ºC for 2 h still under stirring. The as-prepared HGO was purified by washing and centrifuging to remove the residual H_2O_2 and then re-dispersed in 30 mL deionized (D.I.) water to obtain a HGO dispersion.

Preparation of Graphene-supported TMOs composites (TMO@G):

The graphene-supported NCO composite (NCO@G) was synthesized using the hydrothermal method. In brief, 4 mmol of $Co(NO_3)_2 \cdot 6H_2O$, 2 mmol of $NiSO_4 \cdot 6H_2O$ and 0.3 g hexamethylenetetramine (HMTA) were dissolved in 10 mL D.I. water under stirring. Then, 20 mL of GO aqueous dispersion (2 mg mL^{-1}) was added under stirring. After 10 min, the mixture was transferred to a Teflon-lined stainless steel autoclave and heated at 180 ºC for 12 h. The solid product was filtered off and washed with D.I. water, freeze dried, and thermally treated at 300 ºC in air for 2 h at a heating rate of 1 ºC min^{-1} to obtain NCO@G sample. The graphene-supported Fe_3O_4 composite (Fe_3O_4@G) was prepared according to a method reported previously.[238] Briefly, 10 mL of D.I. water containing 2.5 mmol of $FeSO_4 \cdot 7H_2O$ was added into 15 mL of 2 mg mL^{-1} GO dispersion. Then, 2.5 mL of D.I. water containing 0.20 g of NaOH was added under stirring. After 1 h, 10 mL of $N_2H_4 \cdot H_2O$ was added. The mixture was sealed in a Teflon-lined stainless steel autoclave and heated at 180 °C for 8 h. The solid product was filtered off and washed with D.I. water, and freeze dried to obtain a Fe_3O_4@G sample.

Preparation of 3D N-HG and TMO composites (TMO@N-HG):

NCO@N-HG was prepared by co-assembly of the aforementioned HGO and NCO@G. In brief, 15 mg of NCO@G was dispersed in a mixture of 100 mg urea and 2.5 mL of aqueous HGO suspension under ultrasonication. The mixture was then transferred into a Teflon-lined stainless steel autoclave and hydrothermally heated at 120 ºC for 4 h. The solid product was filtrated off, washed with D.I. water, freeze-dried, and thermally treated at 350 °C for 2 h in a nitrogen atmosphere to obtain a composite sample of NCO@N-HG. Another sample, Fe_3O_4@N-HG was similarly prepared by hydrothermal treatment of Fe_3O_4@G and HGO.

Preparation of other samples:

NCO and Fe_3O_4 nanoparticles were also synthesized following the same synthesis procedure of NCO@G and Fe_3O_4@G composites without adding GO. N-HG was prepared by hydrothermally reducing 2.5 mL HGO suspension in the presence of 100 mg urea at 120 ºC for 4 h, followed by thermal treatment at 350 °C for 2 h in a nitrogen atmosphere.

7.2.2 **Materials characterization**

XRD patterns were collected on a Bruker D8 X-ray diffractometer with Ni-filtered Cu Kα radiation (λ = 1.54056 Å, 40 kV, 30 mA) at a scan rate of 2 º min^{-1}. FESEM (JEOL 7100F) and TEM (TECNAI F20) were used to characterize the morphology of samples. XPS was acquired on a Kratos Axis ULTRA X-ray photoelectron spectrometer with a 165 mm hemispherical electron energy analyzer and a monochromatic Al Kα (1486.6 eV) radiation at 225 W (15 kV, 15 mA). Argon sorption isotherms were measured on Tristar II 3020 at the liquid Argon temperature. Before measurement, the samples were degassed at 150 ºC for 24 h. The pore size distribution curves were obtained by the density functional theory (DFT) method. TGA was conducted in air from room temperature up to 700 ºC at a heating rate of 5 ºC min^{-1} using a Perkin-Elmer STA 6000.

7.2.3 **Electrochemical measurements**

All electrodes were prepared by mixing 70 wt. % of an active material, 20 wt. % of an electrical conductor (carbon black), and 10 wt.% of a binder (carboxymethyl cellulose, CMC) in D.I. water to form a slurry, which was subsequently coated on a copper foil. After drying at 60 ºC overnight in a vacuum oven, the copper foil was punched into circular discs.

A NIB was assembled using a 2032-type coin cell with the discs as the anode, sodium foil as the counter electrode, glass fiber (Whatman, GF/C, USA) as the separator and 1 M $NaPF_6$ dissolved in diethylene glycol dimethyl ether solvent as the electrolyte. Both the electrolyte preparation and the coin cell fabrication were performed in an Argon-filled glovebox. Full NIC cells were fabricated with NCO@N-HG or Fe_3O_4@N-HG as the anode and a commercial AC (a specific area of 1200 m^2 g^{-1} from AC Technologies Pty Ltd, Australia) as the cathode. Before assembling the full cells, both NCO@N-HG and Fe_3O_4@N-HG electrodes were pre-cycled 3 times at 0.1 A g^{-1} in sodium half-cells and then sodiated to 0.1 V versus Na^+/Na. To balance the charge density of the two electrodes, the mass loading of the cathode and the anode was about 3.2 mg cm^{-2} and 1 mg cm^{-2}, respectively.

7.3 Results and discussion

7.3.1 **Structure and electrochemical performance in sodium half-cells**

Scheme 7.1 illustrates the procedure for preparing of the composite of TMO@N-HG. HGO was firstly prepared by etching the carbon atoms around the defective sites of GO with H_2O_2.[68,237] TMO@G were prepared in a hydrothermal method. In this process, oxygen-containing groups (carboxyl, hydroxyl and epoxy groups) in GO served as the active sites for nucleation and growth of TMO NPs. In the meantime, GO was reduced.[209] TMO@N-HG was then prepared by co-assembly of the aforementioned HGO and TMO@G. Briefly, the obtained TMO@G was crushed and dispersed in a urea dissolved aqueous HGO suspension for a hydrothermal treatment. During this treatment, the HGO linked with TMO@G via oxygen-containing groups to self-assemble into 3D hydrogels. Simultaneously, HGO was reduced and doped with nitrogen by urea. After freeze-drying and thermal treatment, a TMO@N-HG with macroporous channels derived from 3D assembly, as well as nanoporous channels derived from the etched nanoholes in graphene sheets formed. The details of sample preparation are provided in the experimental section.

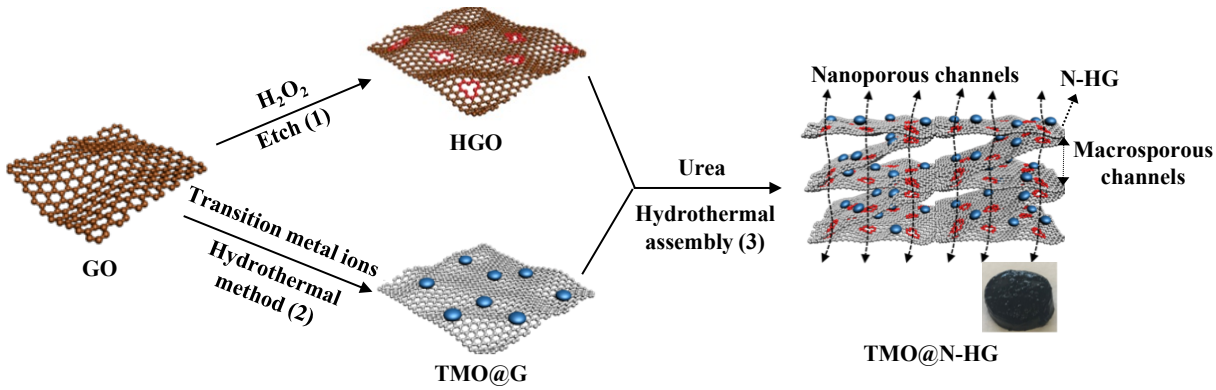

Scheme 7.1 The overall synthetic procedure of TMO@N-HG: (1) preparation of HGO by etching GO sheets with H_2O_2, (2) preparation of TMO@G using a hydrothermal method, (3) dispersing TMO@G in a urea-dissolved HGO suspension for a hydrothermal treatment to obtain TMO@N-HG.

Figure 7.1a shows the TEM image of N-HG, which was synthesized by etching GO with H_2O_2 followed by a hydrothermal reaction in the presence of urea. The N-HG sheets exhibited abundant in-plane nanoholes of diameters ranging from 1.0 to 3.5 nm. This confirmed that H_2O_2 can partially oxidize and etch GO, leaving behind nanoholes in GO to form HGO.[235] The HGO assembled with NCO@G (Figure S7.1a, in the supplementary data 7.5) to prepare 3D NCO@N-HG composite based on the synthetic procedure in Scheme 1. As expected, the composite exhibited various cumulative volumes of pores (Figure S7.2), and the pore size distribution curve indicates the presence of both micropores peaked at 1.1 nm and prominent mesopores peaked at 3.2 nm, which is consistent with the TEM study in Figure 7.1a. Figures 1b-g show the SEM and TEM images of sample NCO@N-HG. A 3D graphene framework with interconnected macrospores ranging from sub-micrometers to several micrometers can be seen from Figures 7.1b and 1c. The TEM images (Figure 7.1d and e) of NCO@N-HG show that many NCO NPs with sizes of about 5 nm were on the graphene sheets. The lattice fringes of NCO NP with a space of 0.245 nm agrees well with the d-space of the (311) plane of the NCO crystal.[216] Meanwhile, the selected area electron diffraction (SAED) pattern show diffraction rings (Figure 7.1f) of (311), (400), (511), and (620) which were well indexed to the crystal planes of NCO.[48] The high-angle annular dark-field scanning TEM (HAADF-STEM) image and elemental mapping results of NCO@N-HG (Figure 7.1g) confirmed the existence of elements C, N, Ni, Co, and O, suggesting that N has been doped in the graphene sheets. The unique macro- and nanoporous feature of NCO@N-HG combined with nitrogen doping is favorable for electrolyte accessibility and rapid sodium ions transport.

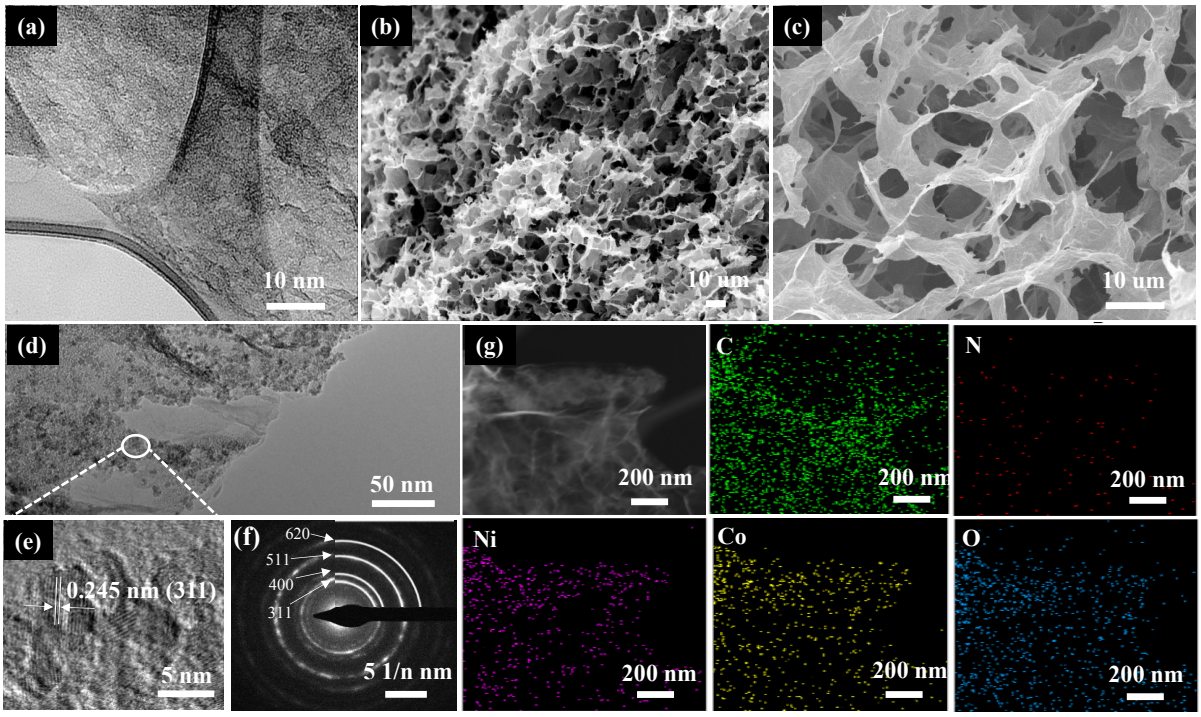

Figure 7.1 (a) TEM images of N-HG sheets with etched pores. (b-c) SEM images of NCO@N-HG at different magnifications. (d and e) TEM and HRTEM images, (f) SAED pattern, and (g) HAADF-STEM image and elemental mapping results of NCO@N-HG.

Figure 7.2a shows the XRD pattern of sample NCO@N-HG. The broad diffraction peak at 36.7 degrees two theta confirmed that the size of the NCO crystals is in the nanometer range, which is consistent with the TEM data. The small diffraction hump appearing in the range of 22-28 degrees two theta is attributed to the re-stacked graphene sheets as confirmed by the XRD pattern of sample N-HG shown in Figure S7.3, which compares the XRD patterns of samples N-HG and GO. For sample N-HG, a broad peak in the two theta ranges of 20-30 degrees can be seen. However, the peak at 11.2 degrees two theta disappeared, indicating the GO sheets were reduced after the hydrothermal treatment, leading to sheets stacking.

Figure 7.2b shows the XPS survey scan of sample NCO@N-HG. The binding energies of 284.8, 399.8, 530.8, 779.8 and 854.8 eV corresponded to C 1s, N 1s, O 1s, Co 2p and Ni 2p, respectively, confirming the integration of NCO and N-HG. Figures 7.2c and 7.2d present the high-resolution XPS spectra of Ni 2p and Co 2p of NCO@N-HG, respectively. The Ni 2p and Co 2p spectra were deconvoluted with two peaks assigned to Ni^{2+}/Ni^{3+} and Co^{2+}/Co^{3+}, respectively, with two satellite peaks as well. This matched well with previously reported XPS spectra of Ni 2p and Co 2p in NCO.[51] Figure 7.2e shows the high-resolution XPS

spectrum of N 1s, which can be resolved into three components centered at 398.2, 399.6 and 401.6 eV, representing the pyridinic, pyrrolic and graphitic types of N atoms, respectively. In addition, the XPS results revealed that the N-doping level was 6.0 at.% in N-HG. Doping N in graphene not only enhances its electronic conductivity, but also improves the wettability between graphene and the organic electrolyte.[219] Figure 7.2f compares the C 1s high-resolution XPS spectra of GO and NCO@N-HG. The dramatic loss of oxygen-containing functional groups (C-O/C-O-C and C=O) further confirmed the reduction of GO. Therefore, the XRD and XPS results confirmed the formation of NCO and N-HG composite, the reduction of GO and the successful N-doping in graphene.

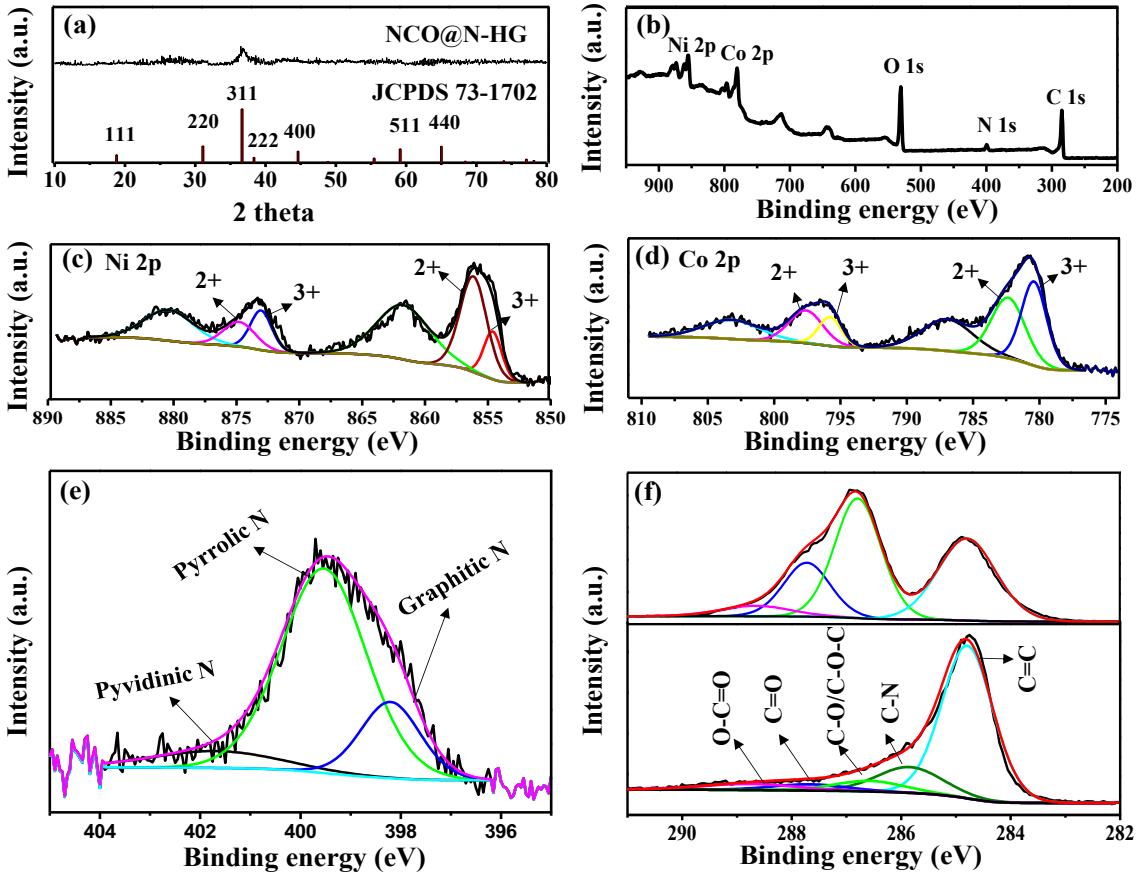

Figure 7.2 (a) XRD pattern of NCO@N-HG and the standard NCO JCPDS card (no. 73-1702). (b) XPS survey of NCO@N-HG. (c, d and e) High-resolution XPS spectrum of Ni 2p, Co 2p and N 1s for NCO@N-HG, respectively. (f) High-resolution XPS spectrum of C 1s for NCO@N-HG (bottom) and GO (top).

Figure 7.3a shows the CV curves of the NCO@N-HG electrode for the first four cycles in the potential range of 0.005 to 3.000 V (versus Na^+/Na) at a scan rate of 0.2 mV s^{-1}. For the

first cathodic scan, the strong reduction peak observed at 0.76 V corresponds to the reduction of Ni^{2+}/Ni^{3+} and Co^{2+}/Co^{3+} to Ni^{o} and Co^{o}, and the formation of a solid electrolyte interphase (SEI). For the anodic scan, two broad peaks appeared at 0.76 V and 1.73 V, which are attributed to the oxidation of Ni^{o}/Co^{o} to Ni^{2+}/Co^{2+}, and Co^{2+} further to Co^{3+}, respectively.[48] Figure 7.3b shows the GCD profiles of NCO@N-HG at current densities ranging from 0.1 to 5.0 A g^{-1}. NCO@N-HG produced GCD profiles without a noticeable plateau at all current densities. This indicates that the reaction mechanism between sodium ions and NCO@N-HG not only involves in phases conversion but also has a large contribution of surface capacitive behavior.[239] The NCO@N-HG electrode also displayed a long cycling performance, as shown in Figure 7.3c. After activated at 0.1 A g^{-1} for the first few cycles, NCO@ N-HG remained the capacity of 348 mAh g^{-1} at 1 A g^{-1} at the 500^{th} cycle with a capacity retention of 85.7 %.

An electrochemical study compared with NCO@G (Figure S7.1a) and NCO (in Figure S7.1b) electrodes was performed in Figure 7.3d-f. Figure 7.3d shows the rate performance of samples NCO@N-HG, NCO@G and NCO. All electrodes exhibited continuously decrease in capacity in the first few cycles. The capacity loss can be attributed to the formation of SEI on the electrode surface. In the subsequent cycles, electrode NCO@N-HG delivered capacities of 639, 446, 442, 427, 403, 370, and 310 mAh g^{-1} at current rates of 0.05, 0.1, 0.2, 0.5, 1, 2 and 5 A g^{-1}, respectively. When the current rate was reversed back to 0.1 A g^{-1}, the electrode capacity was about 443 mAh g^{-1}, very close to 446 mAh g^{-1}, indicating an excellent cycling stability of this electrode. In contrast, the capacities of NCO and NCO@G electrodes dropped fast in the first 20 cycles, and the specific capacities in the subsequent cycles at different current rates were much lower than that of electrode NCO@N-HG.

Figure 7.3e compares the cycling performance of the three electrodes measured at 0.1 A g^{-1}. Despite the decay in the initial few cycles, NCO@N-HG exhibited the best cycling performance with a capacity which was slowly increased to 510 mAh g^{-1} at the 100^{th} cycle. This capacity-increasing trend with cycling is most probably due to the activation of sodium transport sites in the electrodes,[214] and the reversible formation of a polymeric gel-like film, which grows continuously and delivers additional reversible capacity after the first few cycles.[240–242] By contrast, the capacities of NCO@G and NCO were rapidly decreased to 221 and 150 mAh g^{-1} respectively at the same testing conditions. The superior rate and cycling performance of NCO@N-HG was attributed to the structure robustness of 3D N-HG

foam, which could buffer the volume change of NCO during the charge/discharge process. Meanwhile, the high electronic conductivity of the graphene enhanced the electron transport, and the unique pore structure consists of macrospores in the 3D network and nanopores in the graphene sheets facilitated the sodium ions transport.

Figure 7.3f compares the Nyquist plots of electrodes, along with a fitted circuit. Both plots showed a single semicircle in the high-to-medium frequency region and the charge-transfer kinetics at the electrode/electrolyte interface (R_{ct}), as well as a slope in the low frequency region which stands for the diffusive Warburg impedance (W). R_c is the resistance of the electrolyte. According to the fitting results, NCO@N-HG showed a smaller resistance of R_{ct} (63 Ω) than that of NCO@G and NCO (128 and 227 Ω, respectively), further demonstrating that addition of N-HG indeed improved the electron transport kinetics of the electrode materials. Based on TGA measurement (Figure S7.4), the mass ratio of the graphene in NCO@N-HG composite was about 31.9%.

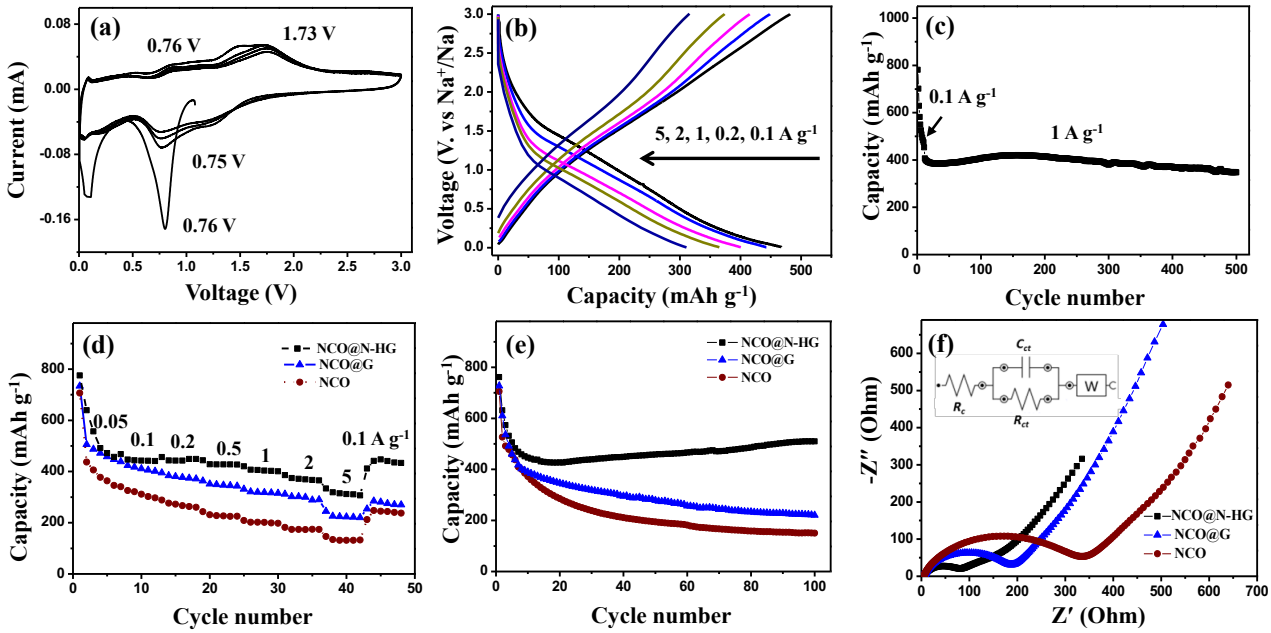

Figure 7.3 (a) CV curves at a scan rate of 0.2 mV s^{-1}, (b) GCD profiles at various current densities from 0.1 to 2.0 A g^{-1}, and (c) cycling performance at 1 A g^{-1} of NCO@N-HG. (d) Rate performance from current densities from 0.05 to 5.0 A g^{-1}, (e) cycling performance at 0.1 A g^{-1} and (f) Nyquist plots of NCO@N-HG, NCO@G and NCO electrodes.

The 3D Fe_3O_4@N-HG architecture was also constructed based on the synthetic procedure in Scheme 7.1. Fe_3O_4@N-HG (Figures 7.4a and b) showed a similar morphology to that of

NCO@N-HG, exhibiting the macroporous structure arising from the 3D graphene architecture. DFT analysis (Figures S7.5a and b) of Fe_3O_4@N-HG confirmed the presence of the nanopores peaking at about 1.0 and 3.3 nm which were mainly derived from the addition of holey graphene. The mass ratio of graphene in Fe_3O_4@N-HG was about 34.3% (Figure S7.4), similar to that of graphene in NCO@N-HG. TEM images (Figure 7.4c and d) show that graphene sheets were anchored with nanoparticles with sizes about 20 to 35 nm. The lattice fringes of NP (Figure 7.4d) with a space of 0.253 nm corresponds to the d-space of the (311) plane in Fe_3O_4, and the diffraction rings of (220), (311), (400), (422), (511) and (440) in the SAED patterns (Figure 7.4e) further confirmed that the nanoparticles were Fe_3O_4 crystals. This is in consistent with the XRD patterns in Figure S7.5c. The HAADF-STEM image and elemental mapping results of Fe_3O_4@N-HG (Figure 7.4f) confirmed the existence of elements C, N, Fe and O, suggesting that N has been doped in the graphene sheets.

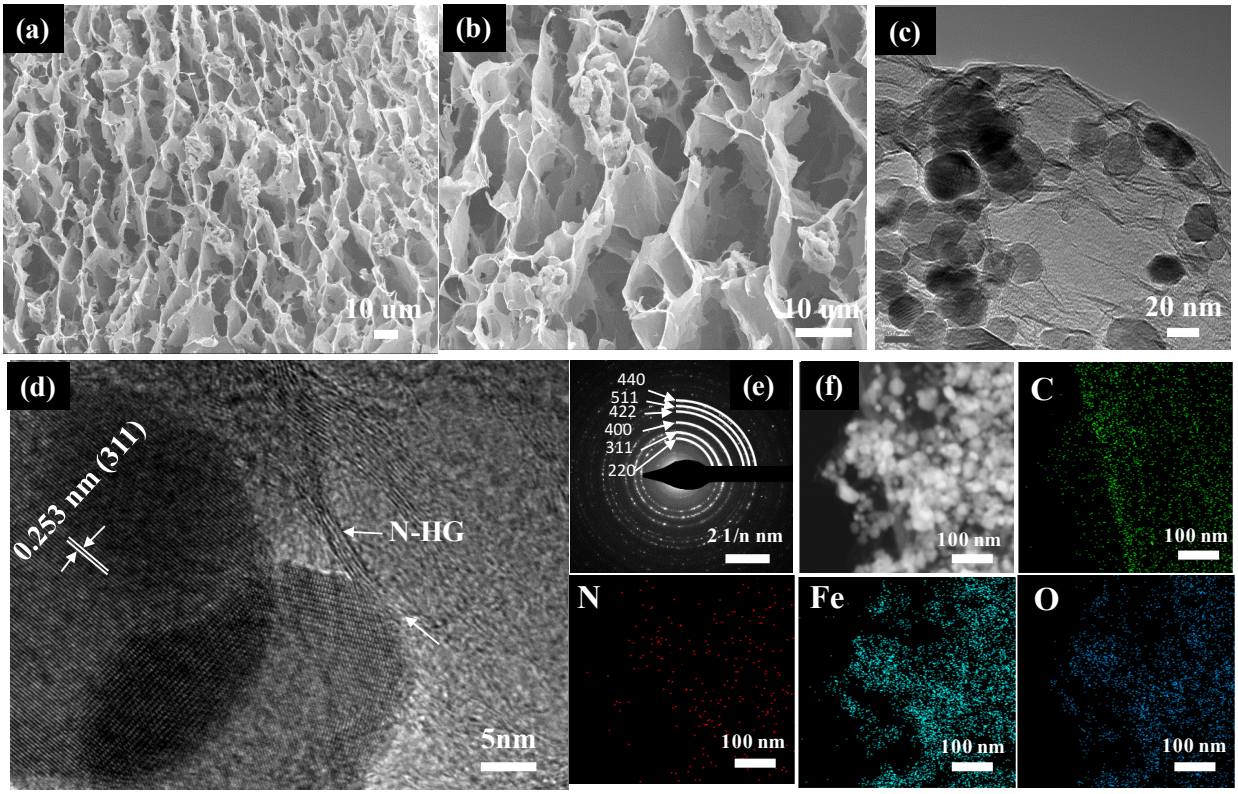

Figure 7.4 (a, b) SEM images, (c-d) TEM images, (e) SAED pattern and (f) HAADF-STEM image with elemental mapping results of the Fe_3O_4@N-HG.

Figure 7.5a shows the CV curves of the Fe_3O_4@N-HG electrode for the first four cycles in the potential range of 0.005 to 3.000 V versus Na/Na^+ at a scan rate of 0.2 mV s^{-1}. For the first cathodic scan, the strong reduction peak observed at 0.65 V corresponds to the reduction of Fe^{2+}/Fe^{3+} to Fe^0, and the formation of a SEI.[228,236] For the anodic scan, two broad peaks appeared at 0.78 V and 1.50 V, which are attributed to the oxidation of Fe^0 to Fe^{2+}, and further to Fe^{3+}, respectively.[232] In the subsequent cycles, the full sodiation potential was characterized by a high voltage at 0.75 V. This potential change from 0.65 to 0.75 V is mainly in virtue of the improved kinetics of Fe_3O_4@N-HG, originating from the inherent nanosize effects in the TMO electrode during cycling.[243] Figure 7.5b shows the GCD profiles of Fe_3O_4@N-HG at current densities ranging from 0.1 to 5.0 A g^{-1}. The slope charge-discharge curves reveals that the sodium storage in Fe_3O_4@N-HG involved in both the capacitive and diffusion-controlled process.[244] Figure 7.5c compares the rate performance of the Fe_3O_4@N-HG, Fe_3O_4@G and Fe_3O_4 electrodes. Electrode Fe_3O_4@N-HG delivered capacities of about 448, 442, 425, 390, 350, 310, and 220 mAh g^{-1} at current rates of 0.05, 0.1, 0.2, 0.5, 1, 2 and 5 A g^{-1}, respectively. When the current rate was reversed back to 0.1 A g^{-1}, the electrode capacity was about 444 mAh g^{-1}, very close to 442 mAh g^{-1}. By contrast, the specific capacities of Fe_3O_4@G and Fe_3O_4 at different current rates were much lower than those of Fe_3O_4@N-HG. For example, Fe_3O_4@G and Fe_3O_4 showed the low capacities of only 205 and 245 mAh g^{-1} at 0.1 A g^{-1}, respectively. At a current rate of 2 A g^{-1}, low capacities of 155 and 130 mAh g^{-1} were exhibited, respectively. The low capacities were mainly due to the significant aggregation of Fe_3O_4@G (Figure S7.1c) and Fe_3O_4 (Figure S7.1d) occurred during electrode preparation, thus lowering the active sites accessible to the electrolyte. The cycling performance of the three samples is shown in Figure 7.5d. The capacity of Fe_3O_4@N-HG was also superior to that of Fe_3O_4@G and Fe_3O_4 electrodes. The Fe_3O_4@N-HG sample kept a capacity-increasing trend with a capacity of 443 mAh g^{-1} at the 100^{th} cycle at 0.1 A g^{-1}, which was higher than the reported Fe_3O_4 based materials for NIBs.[228,229,232,236] The enhanced electrochemical performance of Fe_3O_4@N-HG was mainly attributed to the bi-continuous pathways for both sodium ions and electrons constructed by the N-HG framework.

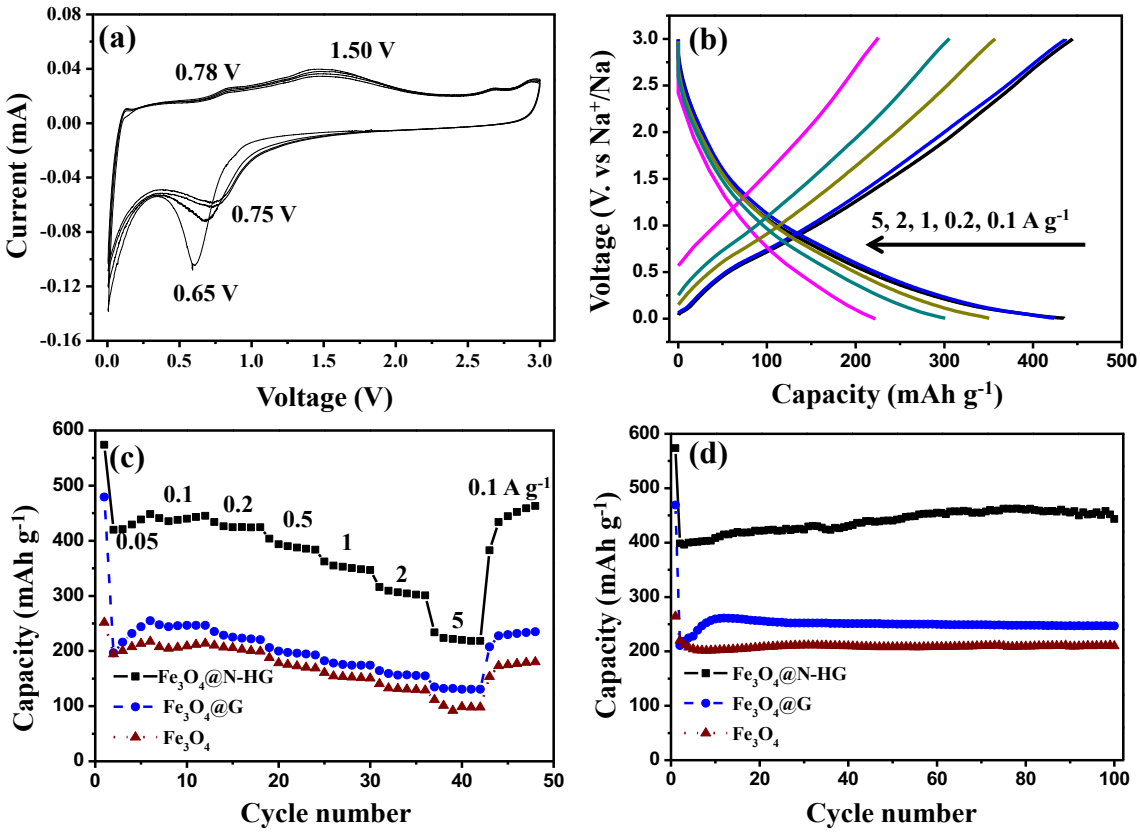

Figure 7.5 (a) CV curves at a sweep rate of 0.2 mV s^{-1} and (b) GCD profiles at various current densities from 0.1 to 2.0 A g^{-1} of Fe_3O_4@N-HG. (c) Rate performance from current densities from 0.05 to 5.0 A g^{-1} and (d) cycling performance of Fe_3O_4@N-HG, Fe_3O_4@G, and Fe_3O_4 electrodes at 0.1 A g^{-1}.

7.3.2 **Electrochemical performance in full sodium-ion capacitor cells**

Full cell of NICs were assembled with NCO@N-HG or Fe_3O_4@N-HG electrodes as the anodes and commercial activated carbons (AC) as the cathodes. The assembled NICs which were designated as NCO@N-HG//AC and Fe_3O_4@N-HG//AC, respectively. Figure 7.6a and b shows their GCD curves from 0.5 A g^{-1} to 5 A g^{-1}. Both GCD curves are not strictly linear, indicating an electrocapacitive charge storage mechanism at the electrode/electrolyte interface. The energy and power densities were estimated and presented in Figure 7.6c. At power densities of 400 W kg^{-1} and 10, 000 W kg-1, the NCO@N-HG//AC NIC delivered energy densities of 107 Wh kg^{-1} and 52 Wh kg^{-1}, respectively, while the Fe_3O_4@N-HG//AC NIC exhibited the energy densities of 106 Wh kg^{-1} and 47 Wh kg^{-1} correspondingly. Figure 7.6d shows the cycling stability of the NICs at a current rate of 3 A

g^{-1}. The capacitance retentions for both NICs were more than 89.0% after 1000 cycles, further demonstrating that using nitrogen-doped holey graphene sheets to stabilize NCO and Fe_3O_4 particles is an effective approach towards developing high performance NICs.

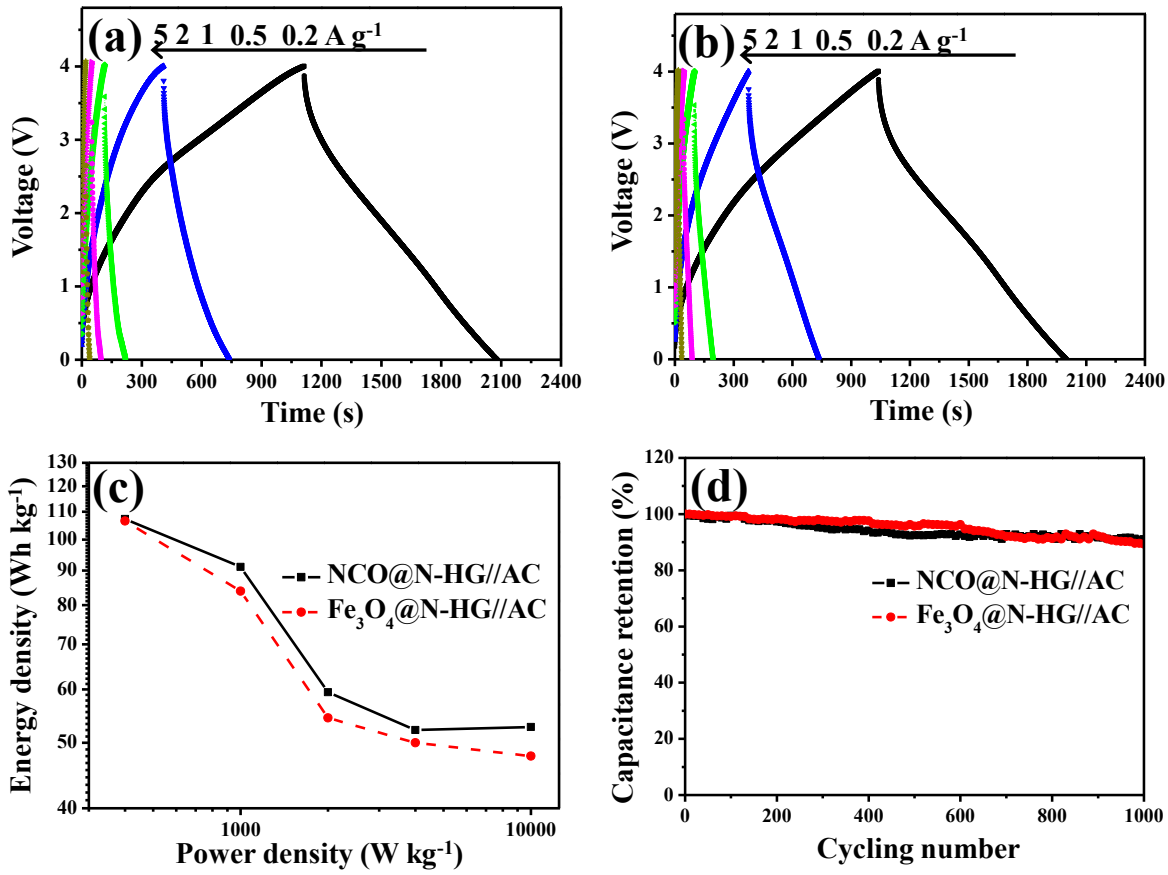

Figure 7.6 GCD curves of (a) NCO@N-HG//AC and (b) Fe_3O_4@N-HG//AC. (c) Ragone plot of the NICs. (d) Cycling performance of NICs at a current rate of 3 A g^{-1}.

7.4 Conclusions

We have demonstrated an effective approach to preparing high-performance sodium-ion storage anode materials by loading NCO and Fe_3O_4 nanoparticles in 3D N-HG framework. The thin graphene sheets buffer the volume change and the unique macroporous architecture in combination with the presence of nanopores in graphene sheets facilitate ion transport and during charge/discharge, contributing to the observed high capacity and good

cycling performance. Specifically, charge storage capacities of 510 mAh g^{-1} and 443 mAh g^{1} were achieved with electrodes NCO@N-HG and Fe_3O_4@N-HG, respectively, at the 100th cycle at 0.1 A g^{-1} in NIBs. By coupling with a commercial AC as the cathode, the NCO@N-HG//AC NIC delivered energy densities of 107 Wh kg^{-1} and 52 Wh kg^{-1} at power densities of 400 W kg^{-1} and 10, 000 W kg^{-1} respectively, while the Fe_3O_4@N-HG//AC NIC exhibited the energy densities of 106 Wh kg^{-1} and 47 Wh kg^{-1} correspondingly. These features manifest the NCO@N-HG and Fe_3O_4@N-HG composite materials as promising anodes for sodium-ion storage. While only NCO and Fe_3O_4 were investigated in this work, it is believed that the approach can be extended to modify other transition-metal oxides for sodium-ion storage, such as Co_3O_4, NiO, Fe_2O_3, and TiO_2.

7.5 Supplementary data

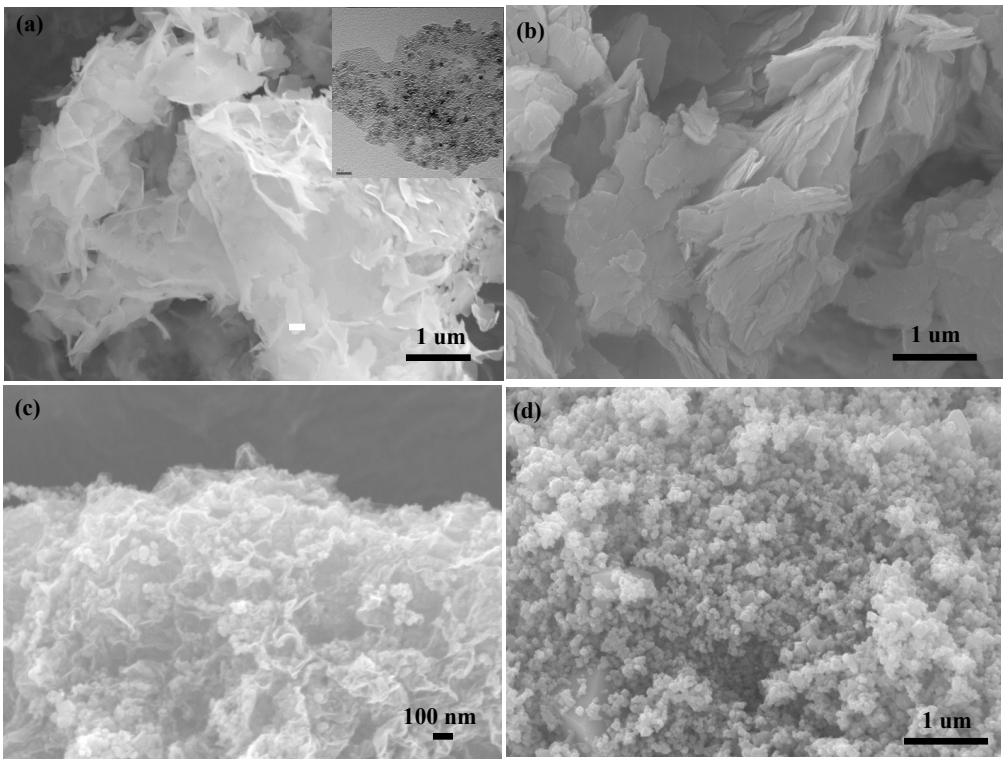

Figure S7.1 SEM images of (a) NCO@G (the inset shows its TEM image), (b) NCO, (c) Fe_3O_4@G and (d) Fe_3O_4.

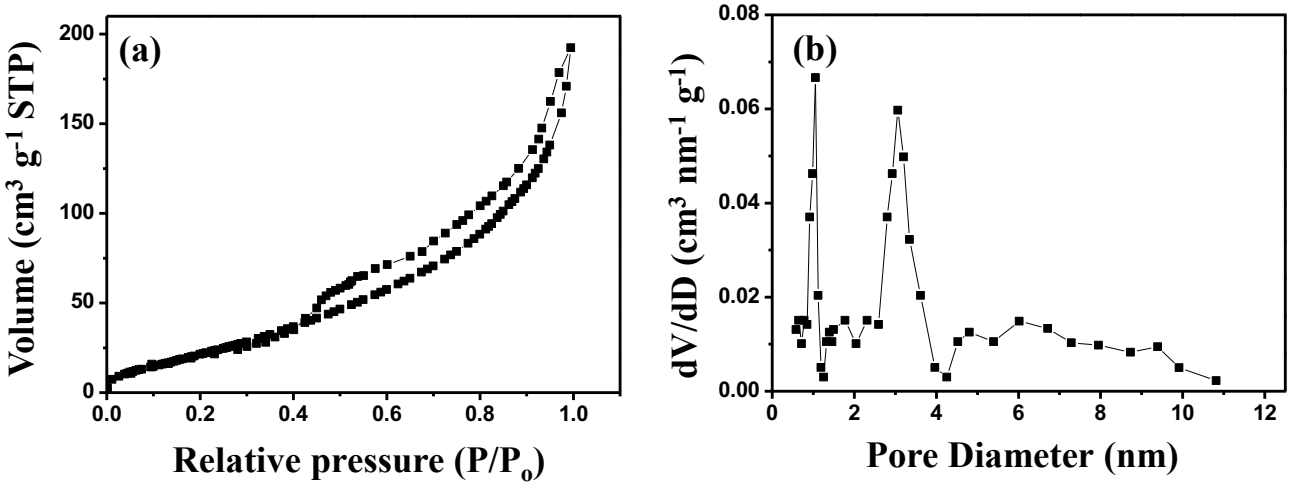

Figure S7.2 (a) Argon adsorption/desorption isotherms and (b) DFT pore size distributions of NCO@N-HG.

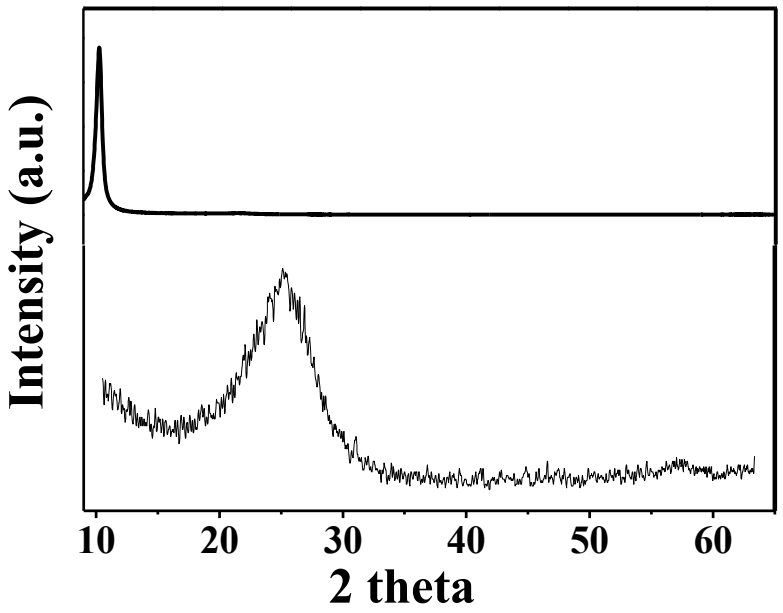

Figure S7.3 XRD patterns of GO (top) and N-HG (bottom).

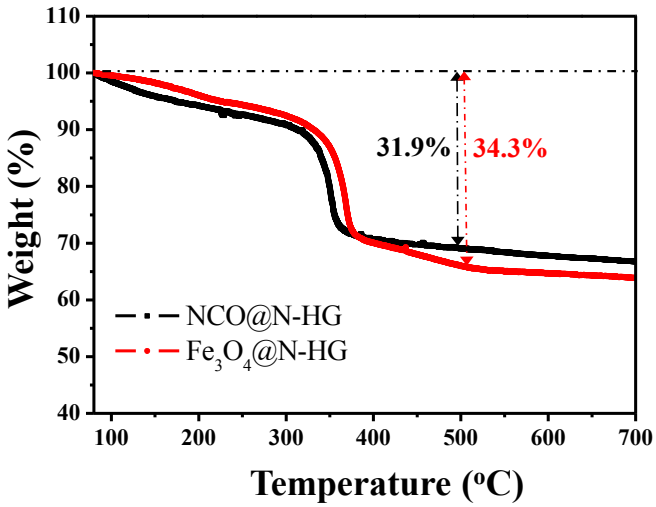

Figure S7.4 TGA curves of NCO@N-HG and Fe_3O_4@N-HG.

The weight loss below 500°C was mainly due to the removal of the graphene in the composites. Temperature from 500 °C to 700 °C, both curves show a small decreasing trend, which are probably due to the decomposition of the NCO and Fe_3O_4 crystals.[245,246]

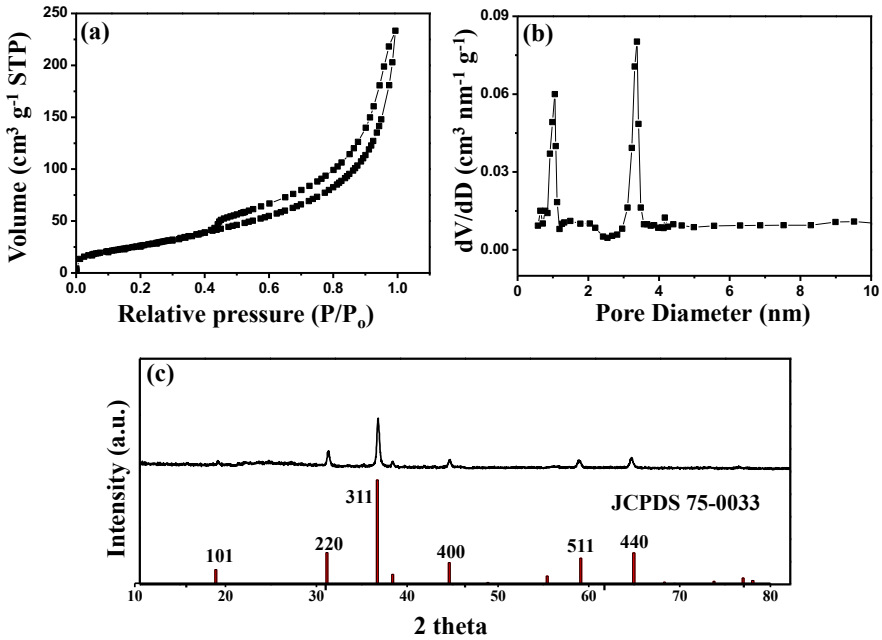

Figure S7.5 (a) Argon adsorption/desorption isotherms, (b) DFT pore size distributions of Fe_3O_4@N-HG. (c) XRD patterns for Fe_3O_4@N-HG and the standard Fe_3O_4 (JCPDS card no. 75-0033)

Chapter 8 Conclusions and recommendations

8.1 Conclusions

The objectives of this PhD project were to significantly improve the electrochemical properties of nickel cobaltite ($NiCo_2O_4$) in sodium-ion capacitors (NICs). As a transition metal oxide (TMO), $NiCo_2O_4$ (NCO) with rich electroactive sites is a promising anode material for sodium-ion storage. However, this material suffers from large volume change during repeated cycles and poor electronic/ionic conductivity, leading to poor rate capability and cycling stability. This PhD thesis work has significantly improved the physical and electrochemical properties of nickel cobaltite with regard to electrical conductivity, structural stability, and sodium ion diffusivity in the bulk electrode.The following conclusions could be drawn:

1 Spherical NCO particles have been synthesized by using a solvothermal method. It was found that subsequent thermal treatment temperature played an important role in determining the crystalline structure and electrochemical properties of spherical NCO. The NCO sample treated at 350 ^{o}C showed an optimal performance as anode in a sodium half-cell with a specific discharge capacity of 274 mA h g^{-1} after 100 cycles at a current density of 100 mA g^{-1}. A NIC assembled using this sample as the anode and a commercial activated carbon (AC) as the cathode delivered an energy density of 33.75 Wh kg^{-1} at a power density of 900 W kg^{-1}, with a cycling retention of 70.3 % after 1000 cycles. Hollow NCO spheres with a chestnut shell morphology have also been synthesized using the solvothermal method. It exhibited a reversible capacity of 313 mAh g^{-1} at 1 A g^{-1} in a sodium half-cell.

2 Mechanism study revealed that the NCO phase was converted to metallic nickel, cobalt and sodium oxide phases upon pre-sodiation. The pre-sodiation of NCO was found to improve its energy density by 5-9 times in a NIC. A NIC assembled with the pre-sodiated

NCO as the anode and an AC as the cathode exhibited an energy density of 60 Wh kg^{-1} at a power density of 10,000 W kg^{-1}, much better performance than that reported in the literature.

3 The physical and electrochemical properties of the NCO particles were improved by using nitrogen-doped reduced graphene oxide (N-rGO). A porous N-rGO framework was used to encapsulate NCO particles to form a NCO@N-rGO composite. In addition to enhance electronic conductivity and alleviated the volume changes of NCO during charge/discharge, the N-rGO network also contributed to charge storage via a capacitive mechanism. A NIC assembled with NCO@N-rGO as the anode and an AC as the cathode delivered an energy density of 48.8 Wh kg^{-1} at a power density of 9750 W kg^{-1} with a stable cycle life. The good electrochemical performance of the electrode material indicates that using N-rGO to stabilize NCO particles is a feasible approach towards developing high-performance anode materials for NICs.

4 A three-dimensional (3D) nitrogen-doped holey graphene (N-HG) was prepared and used to stabilize NCO particles, forming a NCO@N-HG composite. This composite exhibited good rate capabilities with a capacity of 403 mAh g^{-1} at a current density of 1 A g^{-1}, which was higher than the 358 mAh g^{-1} of NCO@N-rGO in a sodium half-cell. A NIC assembled with NCO@N-HG as the anode and an AC as the cathode also delivered a higher energy density of 52 Wh kg^{-1} at a power density of 10,000 W kg^{-1}. The physical and electrochemical properties of magnetite (Fe_3O_4) nanoparticles were also improved by using the 3D N-HG. The thin graphene sheets in the composites facilitate the electron transport and buffer the volume changes during charge/discharge, while the interconnected 3D macroporous network with a pore size in several micrometers range, combined with the nanopores in the N-HG provide pathways for rapid ion transport. The good electrochemical performance of the composites indicates that using 3D N-HG to support TMOs particles is an effective and general approach towards developing high-performance anode materials for sodium-ion storage.

8.2 Recommendations

The good electrochemical performance indicates that NCO-based materials hold a great promise as anode for high-performance NICs with competing energy and power densities. Based on the research results obtained in this thesis work, a few recommendations are given in the future studies:

1 NCO hollow spheres with a chestnut shell morphology showed high specific capacity in sodium-ion storage, but the tap density of NCO should be low due to its porous and hollow structure. The low tap density of NCO is still a critical issue which needs to be addressed in the future for commercial use.

2 Using 3D N-HG framework to support TMOs particles is an effective and general approach towards developing high-performance anode materials for sodium-ion storage. Balancing well the weight ratio of NCO and N-HG could further optimize the performance. This is an issue for future research to explore.

3 The mass loadings of anodes electrodes were about 1 mg cm^{-2} in this thesis work. Optimization of the mass loadings can maximize the volumetric energy density, which deserves further discussion to develop the materials into practical applications.

4 In this thesis work, electrodes were prepared by using a binder (carboxymethyl cellulose, CMC) to stick the active materials and an electrical conductor (carbon black), which were subsequently coated on a copper current collector. However, further attempts on using the 3D graphene composites aerogel as a flexible free-standing electrode without the addition of any additives, binders, or current collectors are desired.

5 The initial coulombic efficiency of graphene composites samples were relatively low due to the solid electrolyte interphase (SEI). The mechanism of such SEI formation is interesting and needs further investigation.

References

1 G. Team, EIA, https://www.green4sea.com/eia-fossil-fuel-still-dominate-us-energy-consumption, (accessed February 6, 2018).

2 O. Ellabban, H. Abu-Rub and F. Blaabjerg, *Renew. Sustain. Energy Rev.*, 2014, **39**, 748–764.

3 E. Yao, H. Wang, L. Liu and G. Xi, *Energies*, 2014, **8**, 154–171.

4 Electricity storage and renewables: Costs and markets to 2030, http://www.irena.org/publications/2017/Oct/Electricity-storage-and-renewables-costs-and-markets, (accessed August 22, 2018).

5 W. Martin and R. Brodd, *Chem. Rev.,* 2004, **10**, 4245-4270.

6 X. Luo, J. Wang, M. Dooner and J. Clarke, *Appl. Energy*, 2015, **137**, 511–536.

7 J. B. Goodenough and K.-S. Park, *J. Am. Chem. Soc.*, 2013, **135**, 1167–1176.

8 M. D. Slater, D. Kim, E. Lee and C. S. Johnson, *Adv. Funct. Mater.*, 2013, **23**, 947–958.

9 B. L. Ellis and L. F. Nazar, *Curr. Opin. Solid State Mater. Sci.*, 2012, **16**, 168–177.

10 H. Wang, C. Zhu, D. Chao, Q. Yan and H. J. Fan, *Adv. Mater.* 2017, **29**, 1702093.

11 S. R. Sivakkumar and A. G. Pandolfo, *Electrochimica Acta*, 2012, **65**, 280–287.

12 G. G. Amatucci, F. Badway, A. Du Pasquier and T. Zheng, *J. Electrochem. Soc.*, 2001, **148**, A930–A939.

13 Q. Wang, Z. H. Wen and J. H. Li, *Adv. Funct. Mater.*, 2006, **16**, 2141–2146.

14 J.-Y. Luo and Y.-Y. Xia, *J. Power Sources*, 2009, **186**, 224–227.

15 V. Aravindan, Y. L. Cheah, W. F. Mak, G. Wee, B. V. R. Chowdari and S. Madhavi, *ChemPlusChem*, 2012, **77**, 570–575.

16 H. Wang, C. Guan, X. Wang and H. J. Fan, *Small*, 2015, **11**, 1470–1477.

17 Company. Front runner of Lithium Ion Capacitor. JM Energy Corporation, http://www.jmenergy.co.jp/en/profile.html, (accessed February 6, 2018).

18 Maxwell Technologies Delivers First Commercial Application of Lithium-Ion Capacitor Technology in China, http://investors.maxwell.com/investors/news-and-events/press-releases/press-release-details/2016/Maxwell-Technologies-Delivers-First-Commercial-Application-of-Lithium-Ion-Capacitor-Technology-in-China/default.aspx, (accessed February 7, 2018).

19 Z. Chen, V. Augustyn, X. Jia, Q. Xiao, B. Dunn and Y. Lu, *ACS Nano*, 2012, **6**, 4319–4327.

20 K. Kuratani, M. Yao, H. Senoh, N. Takeichi, T. Sakai and T. Kiyobayashi, *Electrochimica Acta*, 2012, **76**, 320–325.

21 J. Yin, L. Qi and H. Wang, *ACS Appl. Mater. Interfaces*, 2012, **4**, 2762–2768.

22 R. Ding, L. Qi and H. Wang, *Electrochimica Acta*, 2013, **114**, 726–735.

23 Y.-X. Wang, S.-L. Chou, D. Wexler, H.-K. Liu and S.-X. Dou, *Chem. Eur. J.*, 2014, **20**, 9607–9612.

24 J. Zhang, Z. Shi and C. Wang, *Electrochimica Acta*, 2014, **125**, 22–28.

25 J. Ding, H. Wang, Z. Li, K. Cui, D. Karpuzov, X. Tan, A. Kohandehghan and D. Mitlin, *Energy Env. Sci*, 2015, **8**, 941–955.

26 X. Wang, S. Kajiyama, H. Iinuma, E. Hosono, S. Oro, I. Moriguchi, M. Okubo and A. Yamada, *Nat. Commun.*, 2015, **6**, 6544.

27 S. Dong, L. Shen, H. Li, P. Nie, Y. Zhu, Q. Sheng and X. Zhang, *J. Mater. Chem. A*, 2015, **3**, 21277–21283.

28 E. Lim, C. Jo, M. S. Kim, M.-H. Kim, J. Chun, H. Kim, J. Park, K. C. Roh, K. Kang, S. Yoon and others, *Adv. Funct. Mater.*, 2016, **26**, 3711–3719.

29 H. Li, Y. Zhu, S. Dong, L. Shen, Z. Chen, X. Zhang and G. Yu, *Chem. Mater.*, 2016, **28**, 5753–5760.

30 S. Dong, L. Shen, H. Li, G. Pang, H. Dou and X. Zhang, *Adv. Funct. Mater.*, 2016, **26**, 3703–3710.

31 S. Liu, Z. Cai, J. Zhou, A. Pan and S. Liang, *J. Mater. Chem. A*, 2016, **4**, 18278–18283.

32 Y. Ding, B. Yang, J. Chen, L. Zhang, J. Li, Y. Li and X. Yan, *Sci. China Mater.*, 2018, **2**, 285-295.

33 R. Wang, S. Wang, X. Peng, Y. Zhang, D. Jin, P. K. Chu and L. Zhang, *ACS Appl. Mater. Interfaces*, 2017, **9**, 32745-32755.

34 B. Babu and M. M. Shaijumon, *J. Power Sources*, 2017, **353**, 85–94.

35 Z. Le, F. Liu, P. Nie, X. Li, X. Liu, Z. Bian, G. Chen, H. B. Wu and Y. Lu, *ACS Nano*, 2017, **11**, 2952–2960.

36 K. R., N. C., K. R. and V. R. R. B., *Electrochimica Acta*, 2017, **256**, 221–231.

37 H.-K. Roh, M.-S. Kim, K. Yoon Chung, M. Ulaganathan, V. Aravindan, S. Madhavi, K. Chul Roh and K.-B. Kim, *J. Mater. Chem. A*, 2017, **5**, 17506–17516.

38 S. Liu, Z. Cai, J, Zhou, M. Zhu, A. Pan, and S. Liang, *J. Mater. Chem. A*, 2017, **5**, 9169-9176.

39 T. Wei, G. Yang and C. Wang, *ACS Appl. Mater. Interfaces*, 2017, **9**, 31861–31870.

40 Y. Dall'Agnese, P. L. Taberna, Y. Gogotsi, and P. Simon, *J. Phys. Chem. Lett.,* 2015, **6**, 2305-2309.

41 M. Rosa Palacín, *Chem. Soc. Rev.*, 2009, **38**, 2565–2575.

42 L. Li Zhang and X. S. Zhao, *Chem. Soc. Rev.*, 2009, **38**, 2520–2531.

43 C. Xu, B. Xu, Y. Gu, Z. Xiong, J. Sun and X. S. Zhao, *Energy Environ. Sci.*, 2013, **6**, 1388–1414.

44 N. Ashok Kumar, R. Ranganathan Gaddam, M. Suresh, S. Rao Varanasi, D. Yang, S. K. Bhatia and X. S. Zhao, *J. Mater. Chem. A*, 2017, **5**, 13204–13211.

45 Y.-E. Zhu, L. Yang, J. Sheng, Y. Chen, H. Gu, J. Wei and Z. Zhou, *Adv. Energy Mater.,* 2017, **22**, 1701222.

46 Li, H., Zhu, Y., Dong, S., Shen, L., Chen, Z., Zhang, X., & Yu, G, *Chem. Mater.,* 2016, **28**, 5753-5760.

47 J. Cui, S. Yao, Z. Lu, J.-Q. Huang, W. G. Chong, F. Ciucci and J.-K. Kim, *Adv. Energy Mater.,* 2017, **1,** 85-95.

48 D. Yang, X. Sun, K. Lim, R. Ranganathan Gaddam, N. Ashok Kumar, K. Kang and X. S. Zhao, *J. Power Sources*, 2017, **362**, 358–365.

49 K. Cao, T. Jin, L. Yang and L. Jiao, *Mater. Chem. Front.*, 2017, **1**, 2213–2242.

50 J, Chen,Q, Ru, Y, Mo, S Hu and X Hou, Phys. *Chem. Chem. Phys.,* 2016, **18**, 18949-18957.

51 R. Alcántara, M. Jaraba, P. Lavela and J. L. Tirado, *Chem. Mater.*, 2002, **14**, 2847–2848.

52 R. Ding, L. Qi and H. Y. Wang, *Electrochimica Acta*, 2015, **168**, 423–423.

53 J.-W. Lee, H.-S. Shin, C.-W. Lee and K.-N. Jung, *Nanoscale Res. Lett.*, 2016, **11**, 45.

54 X. Q. Zhang, Y. C. Zhao, C. G. Wang, X. Li, J. D. Liu, G. H. Yue and Z. D. Zhou, *J. Mater. Sci.*, 2016, **51**, 9296–9305.

55 J. Chen, Q. Ru, Y. Mo, S. Hu and X. Hou, *Phys. Chem. Chem. Phys.*, 2016, **18**, 18949–18957.

56 Y. Wang, H. Huang, Q. Xie, Y. Wang and B. Qu, *J. Alloys Compd.*, 2017, **705**, 314–319.

57 D. Li, D. Yan, X. Zhang, T. Lu, G. Yang and L. Pan, *J. Mater. Sci. Mater. Electron.*, 2017, **28,** 10411-10419.

58 K. Wang, Y. Huang, M. Wang, M. Yu, Y. Zhu and J. Wu, *Carbon*, 2017, **125**, 375–383.

59 G. Gao, H. B. Wu and X. W. (David) Lou, *Adv. Energy Mater.*, 2014, **4**, 1400422.

60 Y. Wei, S. Chen, D. Su, B. Sun, J. Zhu and G. Wang, *J. Mater. Chem. A*, 2014, **2**, 8103–8109.

61 Y. Chen, J. Zhu, B. Qu, B. Lu and Z. Xu, *Nano Energy*, 2014, **3**, 88–94.

62 D. Carriazo, J. Patiño, M. C. Gutiérrez, M. L. Ferrer and F. del Monte, *RSC Adv.*, 2013, **3**, 13690–13695.

63 G. He, L. Wang, H. Chen, X. Sun and X. Wang, *Mater. Lett.*, 2013, **98**, 164–167.

64 N. A. Kumar, R. R. Gaddam, S. R. Varanasi, D. Yang, S. K. Bhatia and X. S. Zhao, *Electrochimica Acta*, 2016, **214**, 319–325.

65 B. Wang, W. A. Abdulla, D. Wang and X. S. Zhao, *Energy Environ. Sci.*, 2015, **8**, 869-875.

66 M. Pumera, *Energy Environ. Sci.*, 2011, **4**, 668–674.

67 R. Atif and F. Inam, *Beilstein J. Nanotechnol.*, 2016, **7**, 1174–1196.

68 H. Sun, L. Mei, J. Liang, Z. Zhao, C. Lee, H. Fei, M. Ding, J. Lau, M. Li and C. Wang, *Science*, 2017, **356**, 599–604.

69 X. Zhao, C. M. Hayner, M. C. Kung and H. H. Kung, *ACS Nano*, 2011, **5**, 8739–8749.

70 Z. Jiang, B. Pei and A. Manthiram, *J. Mater. Chem. A*, 2013, **1**, 7775–7781.

71 J. Gamby, P. L. Taberna, P. Simon, J. F. Fauvarque and M. Chesneau, *J. Power Sources*, 2001, **101**, 109–116.

72 K. Kadirvelu, K. Thamaraiselvi and C. Namasivayam, *Bioresour. Technol.*, 2001, **76**, 63–65.

73 K. G. Adani, R. W. Barley and R. D. Pascoe, *Miner. Eng.*, 2005, **18**, 1269–1276.

74 X. Wang, S. Kajiyama, H. Iinuma, E. Hosono, S. Oro, I. Moriguchi, M. Okubo and A. Yamada, *Nat. Commun.,* 2015, **6**, 6544.

75 R. Thangavel, K. Kaliyappan, K. Kang, X. Sun and Y.-S. Lee, *Adv. Energy Mater.*, 2016, **6**, 1502199.

76 Y.-X. Wang, S.-L. Chou, H.-K. Liu and S.-X. Dou, *Carbon*, 2013, **57**, 202–208.

77 F. Wang, X. Wang, Z. Chang, X. Wu, X. Liu, L. Fu, Y. Zhu, Y. Wu and W. Huang, *Adv. Mater.*, 2015, **27**, 6962–6968.

78 M, Naguib, VN, Mochalin, MW, Barsoum, and Y, Gogotsi, *Adv Mater.*, 2014, **26**, 992-1005.

79 M. Naguib, M. Kurtoglu, V. Presser, J, Lu, J, Niu, M, Heon, L, Hultman, Y, Gogotsi, and MW, Barsoum, *Adv Mater,* 2011, **23**, 4248-4253.

80 D, Er, J. Li, M, Naguib, Y, Gogotsi, and V. B. Shenoy, *ACS Appl. Mater. Interfaces*, 2014, **6**, 11173-11179.

81 P. Barpanda, G. Oyama, SI. Nishimura, SC. Chung and A. Yamada, *Nat. Commun.,* 2014, **17**, 4358.

82 Y. Meng, T. Yu, S. Zhang and C. Deng, *J. Mater. Chem. A*, 2016, **4**, 1624–1631.

83 L.L, Wong, H.M, Chen, and S. Adams, *Phys. Chem. Chem. Phys.*, 2015, **17**, 9186-9193.

84 D. Dwibedi, R. B. Araujo, S. Chakraborty, P. P. Shanbogh, N. G. Sundaram, R. Ahuja and P. Barpanda, *J. Mater. Chem. A*, 2015, **3**, 18564–18571.

85 E. Hosono, T. Saito, J. Hoshino, M. Okubo, Y. Saito, D. Nishio-Hamane, T. Kudo and H. Zhou, *J. Power Sources*, 2012, **217**, 43–46.

86 F. Sauvage, L. Laffont, J.-M. Tarascon and E. Baudrin, *Inorg. Chem.*, 2007, **46**, 3289–3294.

87 B. Fu, X. Zhou and Y. Wang, *J. Power Sources*, 2016, **310**, 102–108.

88 Q. Liu, Z. Hu, M. Chen, Q. Gu, Y. Dou, Z. Sun, S. Chou and S. X. Dou, *ACS Appl. Mater. Interfaces*, 2017, **9**, 3644–3652.

89 X. Xie, M.-Q. Zhao, B. Anasori, K. Maleski, C. E. Ren, J. Li, B. W. Byles, E. Pomerantseva, G. Wang and Y. Gogotsi, *Nano Energy*, 2016, **26**, 513–523.

90 A. Ponrouch, D. Monti, A. Boschin, B. Steen, P. Johansson and M. R. Palacín, *J. Mater. Chem. A*, 2015, **3**, 22–42.

91 D. J. Devlin and P. J. Herley, *React. Solids*, 1987, **3**, 75–84.

92 S. You Hong, Y. Kim, Y. Park, A. Choi, N.-S. Choi and K. Tae Lee, *Energy Environ. Sci.*, 2013, **6**, 2067–2081.

93 H. Kim, J. Hong, Y.-U. Park, J. Kim, I. Hwang and K. Kang, *Adv. Funct. Mater.*, 2015, **25**, 534–541.

94 H. Kim, J. Hong, G. Yoon, H. Kim, K.-Y. Park, M.-S. Park, W.-S. Yoon and K. Kang, *Energy Environ. Sci.*, 2015, **8**, 2963–2969.

95 D. R. MacFarlane, N. Tachikawa, M. Forsyth, J. M. Pringle, P. C. Howlett, G. D. Elliott, J. H. Davis, M. Watanabe, P. Simon and C. A. Angell, *Energy Environ. Sci.*, 2014, **7**, 232–250.

96 D. Monti, E. Jónsson, M. R. Palacín and P. Johansson, *J. Power Sources*, 2014, **245**, 630–636.

97 N. Wongittharom, T.-C. Lee, C.-H. Wang, Y.-C. Wang and J.-K. Chang, *J. Mater. Chem. A*, 2014, **2**, 5655–5661.

98 A. Fukunaga, T. Nohira, R. Hagiwara, K. Numata, E. Itani, S. Sakai, K. Nitta and S. Inazawa, *J. Power Sources*, 2014, **246**, 387–391.

99 C. Ding, T. Nohira, K. Kuroda, R. Hagiwara, A. Fukunaga, S. Sakai, K. Nitta and S. Inazawa, *J. Power Sources*, 2013, **238**, 296–300.

100 Y. Q. Yang, Z. Chang, M. X. Li, X. W. Wang and Y. P. Wu, *Solid State Ion.*, 2015, **269**, 1–7.

101 D. Kumar and S. A. Hashmi, *Solid State Ion.*, 2010, **181**, 416–423.
102 H. Li, L. Peng, Y. Zhu, X. Zhang and G. Yu, *Nano Lett.*, 2016, **16**, 5938–5943.
103 S. Wang, J. Zhao, L. Wang, X. Liu, Y. Wu and J. Xu, *Ionics*, 2015, **21**, 2633–2638.
104 K. Lu, B. Song, X. Gao, H. Dai, J. Zhang and H. Ma, *J. Power Sources*, 2016, **303**, 347–353.
105 R.-S. Kühnel, D. Reber and C. Battaglia, *ACS Energy Lett.*, 2017, **2**, 2005–2006.
106 T. P. Kumar, T. S. D. Kumari and M. A. Stephan, *J. Indian Inst. Sci.*, 2012, **89**, 393–424.
107 B. Jache and P. Adelhelm, *Angew. Chem. Int. Ed.*, 2014, **53**, 10169–10173.
108 P. Han, X. Han, J. Yao, L. Zhang, X. Cao, C. Huang and G. Cui, *J. Power Sources*, 2015, **297**, 457–463.
109 D. A. Stevens and J. R. Dahn, *J. Electrochem. Soc.*, 2000, **147**, 1271–1273.
110 R. R. Gaddam, D. Yang, R. Narayan, K. Raju, N. A. Kumar and X. S. Zhao, *Nano Energy*, 2016, **26**, 346-352.
111 H. Wang, D. Mitlin, J. Ding, Z. Li and K. Cui, *J Mater Chem A*, 2016, **4**, 5149–5158.
112 M. Losurdo, M. M. Giangregorio, P. Capezzuto and G. Bruno, *Phys. Chem. Chem. Phys.*, 2011, **13**, 20836–20843.
113 M. Batzill, *Surf. Sci. Rep.*, 2012, **67**, 83–115.
114 Y. Zhu, S. Murali, W. Cai, X. Li, J. W. Suk, J. R. Potts and R. S. Ruoff, *Adv. Mater.*, 2010, **22**, 3906–3924.
115 C. Lee, X. Wei, J. W. Kysar and J. Hone, *Science*, 2008, **321**, 385–388.
116 Y. Zhang, J. P. Small, W. V. Pontius and P. Kim, *Appl. Phys. Lett.*, 2005, **86**, 073104.
117 Y. Wu, B. Wang, Y. Ma, Y. Huang, N. Li, F. Zhang and Y. Chen, *Nano Res.*, 2010, **3**, 661–669.
118 Y. Huang, J. Liang and Y. Chen, *Small*, 2012, **8**, 1805–1834.
119 K. Ramakrishnan, C. Nithya and R. Karvembu, *ACS Appl. Energy Mater.*, 2018, **1**, 841-850.
120 K. Lu, D. Li, X. Gao, H. Dai, N. Wang and H. Ma, *J. Mater. Chem. A*, 2015, **3**, 16013–16019.
121 H. Hou, X. Qiu, W. Wei, Y. Zhang and X. Ji, *Adv. Energy Mater.,* 2017, **7**,1602898.
122 S. Kajiyama, L. Szabova, K. Sodeyama, H. Iinuma, R. Morita, K. Gotoh, Y. Tateyama, M. Okubo and A. Yamada, *ACS Nano*, 2016, **10**, 3334–3341.
123 Y. Dong, Z.-S. Wu, S. Zheng, X. Wang, J. Qin, S. Wang, X. Shi and X. Bao, *ACS Nano*, 2017, **11**, 4792–4800.

124 C. Zhu, X. Mu, P. A. van Aken, Y. Yu and J. Maier, *Angew. Chem. Int. Ed.*, 2014, **53**, 2152–2156.

125 L. Kong, C. Zhang, J. Wang, W. Qiao, L. Ling and D. Long, *ACS Nano*, 2015, **9**, 11200–11208.

126 H. Kim, E. Lim, C. Jo, G. Yoon, J. Hwang, S. Jeong, J. Lee and K. Kang, *Nano Energy*, 2015, **16**, 62–70.

127 D. Pal, R. K. Pal, J. L. Pandey, S. H. Abdi and A. K. Agnihotri, *J. Mater. Sci. Mater. Electron.*, 2010, **21**, 1181–1185.

128 P. Senguttuvan, G. Rousse, V. Seznec, J.-M. Tarascon and M. R. Palacin, *Chem. Mater.*, 2011, **23**, 4109–4111.

129 J. Yang, Z. Jin, X. Wang, W. Li, J. Zhang, S. Zhang, X. Guo and Z. Zhang, *Dalton Trans.*, 2003, **0**, 3898–3901.

130 C. Chen, Y. Wen, X. Hu, X. Ji, M. Yan, L. Mai, P. Hu, B. Shan and Y. Huang, *Nat. Commun.*, 2015, **6**, 6929.

131 C. Chen, X. Hu, Y. Jiang, Z. Yang, P. Hu, and Y. Huang, *Chem. Eur. J.*, 2014, **20**, 1383-1388.

132 J.-Y. Hwang, S.-T. Myung, J.-H. Lee, A. Abouimrane, I. Belharouak and Y.-K. Sun, *Nano Energy*, 2015, **16**, 218–226.

133 S. Tepavcevic, H. Xiong, V. R. Stamenkovic, X. Zuo, M. Balasubramanian, V. B. Prakapenka, C. S. Johnson and T. Rajh, *ACS Nano*, 2012, **6**, 530–538.

134 D. Wang, Q. Liu, C. Chen, M. Li, X. Meng, X. Bie, Y. Wei, Y. Huang, F. Du, C. Wang and G. Chen, *ACS Appl. Mater. Interfaces*, 2016, **8**, 2238–2246.

135 S. Chen, C. Wu, L. Shen, C. Zhu, Y. Huang, K. Xi, J. Maier and Y. Yu, *Adv. Mater.*, 2017, **29**, 1700431.

136 T. Wei, G. Yang, and C. Wang. *ACS Appl. Mater. Interfaces*, 2017, **37**, 31861-31870.

137 S. Gao, J. Zhao, Y. Zhao, Y. Wu, X. Zhang, L. Wang, X. Liu, Y. Rui and J. Xu, *Mater. Lett.*, 2015, **158**, 300–303.

138 N. Xia, J. Zhao, C. Lai, H. Wang, S. Gao, Z. Zhang and J. Xu, *J. Appl. Electrochem.*, 2017, **47**, 343–349.

139 K. Singh, B. Kirubasankar and S. Angaiah, *Ionics*, 2017, **23**, 731–739.

140 N. Nitta, F. Wu, J. T. Lee and G. Yushin, *Mater. Today*, 2015, **18**, 252–264.

141 L. Shen, L. Yu, X.-Y. Yu, X. Zhang and X. W. D. Lou, *Angew. Chem. Int. Ed.*, 2015, **54**, 1868–1872.

142 L. Li, S. Peng, Y. Cheah, P. Teh, J. Wang, G. Wee, Y. Ko, C. Wong and M. Srinivasan, *Chem. Eur. J.*, 2013, **19**, 5892–5898.

143 J. Liang, Z. Fan, S. Chen, S. Ding and G. Yang, *Chem. Mater.*, 2014, **26**, 4354–4360.

144 G. Zhang and X. W. D. Lou, *Adv. Mater.*, 2013, **25**, 976–979.

145 L. Shen, Q. Che, H. Li and X. Zhang, *Adv. Funct. Mater.*, 2014, **24**, 2630–2637.

146 Y. Lei, J. Li, Y. Wang, L. Gu, Y. Chang, H. Yuan and D. Xiao, *ACS Appl. Mater. Interfaces*, 2014, **6**, 1773–1780.

147 M. Hu, Y. Jiang, W. Sun, H. Wang, C. Jin and M. Yan, *ACS Appl. Mater. Interfaces*, 2014, **6**, 19449–19455.

148 Q. Sun, Q.-Q. Ren, H. Li and Z.-W. Fu, *Electrochem. Commun.*, 2011, **13**, 1462–1464.

149 H. Hou, M. Jing, Z. Huang, Y. Yang, Y. Zhang, J. Chen, Z. Wu and X. Ji, *ACS Appl. Mater. Interfaces*, 2015, **7**, 19362–19369.

150 Y. Zhu, X. Han, Y. Xu, Y. Liu, S. Zheng, K. Xu, L. Hu and C. Wang, *ACS Nano*, 2013, **7**, 6378–6386.

151 D. V. Ragone, *SAE Technical Paper*, 1968, 680453.

152 B. Wang, B. Xu, T. Liu, P. Liu, C. Guo, S. Wang, Q. Wang, Z. Xiong, D. Wang and X. S. Zhao, *Nanoscale*, 2014, **6**, 986–995.

153 A. Rudola, K. Saravanan, C. W. Mason and P. Balaya, *J. Mater. Chem. A*, 2013, **1**, 2653–2662.

154 H. Pan, Y.-S. Hu and L. Chen, *Energy Environ. Sci.*, 2013, **6**, 2338–2360.

155 D. Su, S. Dou and G. Wang, *Chem. Mater.*, 2015, **27**, 6022–6029.

156 Y. Cao, L. Xiao, W. Wang, D. Choi, Z. Nie, J. Yu, L. V. Saraf, Z. Yang and J. Liu, *Adv. Mater.*, 2011, **23**, 3155–3160.

157 L. Wu, D. Buchholz, D. Bresser, L. Gomes Chagas and S. Passerini, *J. Power Sources*, 2014, **251**, 379–385.

158 K.-T. Kim, G. Ali, K. Y. Chung, C. S. Yoon, H. Yashiro, Y.-K. Sun, J. Lu, K. Amine and S.-T. Myung, *Nano Lett.*, 2014, **14**, 416–422.

159 B. Qu, C. Ma, G. Ji, C. Xu, J. Xu, Y. S. Meng, T. Wang and J. Y. Lee, *Adv. Mater.*, 2014, **26**, 3854–3859.

160 Z. Hu, L. Wang, K. Zhang, J. Wang, F. Cheng, Z. Tao and J. Chen, *Angew. Chem.*, 2014, **126**, 13008–13012.

161 T. Zhou, W. K. Pang, C. Zhang, J. Yang, Z. Chen, H. K. Liu and Z. Guo, *ACS Nano*, 2014, **8**, 8323–8333.

162 J. Park, J.-S. Kim, J.-W. Park, T.-H. Nam, K.-W. Kim, J.-H. Ahn, G. Wang and H.-J. Ahn, *Electrochimica Acta*, 2013, **92**, 427–432.

163 X. Xie, K. Kretschmer, J. Zhang, B. Sun, D. Su and G. Wang, *Nano Energy*, 2015, **13**, 208–217.

164 Y. Yui, Y. Ono, M. Hayashi, Y. Nemoto, K. Hayashi, K. Asakura and H. Kitabayashi, *J. Electrochem. Soc.*, 2015, **162**, A3098–A3102.

165 Y. Liu, N. Zhang, L. Jiao, Z. Tao and J. Chen, *Adv. Funct. Mater.*, 2015, **25**, 214–220.

166 Y. C. Lu, C. Ma, J. Alvarado, T. Kidera, N. Dimov, Y. S. Meng and S. Okada, *J. Power Sources*, 2015, **284**, 287–295.

167 J. Ding, H. Wang, Z. Li, A. Kohandehghan, K. Cui, Z. Xu, B. Zahiri, X. Tan, E. M. Lotfabad, B. C. Olsen and D. Mitlin, *ACS Nano*, 2013, **7**, 11004–11015.

168 Y. Cao, L. Xiao, M. L. Sushko, W. Wang, B. Schwenzer, J. Xiao, Z. Nie, L. V. Saraf, Z. Yang and J. Liu, *Nano Lett.*, 2012, **12**, 3783–3787.

169 L. Zhao, J. Zhao, Y.-S. Hu, H. Li, Z. Zhou, M. Armand and L. Chen, *Adv. Energy Mater.*, 2012, **2**, 962–965.

170 Y. Park, D.-S. Shin, S. H. Woo, N. S. Choi, K. H. Shin, S. M. Oh, K. T. Lee and S. Y. Hong, *Adv. Mater.*, 2012, **24**, 3562–3567.

171 Y. Jiang, M. Hu, D. Zhang, T. Yuan, W. Sun, B. Xu and M. Yan, *Nano Energy*, 2014, **5**, 60–66.

172 J. Zhao, Y. Zou, X. Zou, T. Bai, Y. Liu, R. Gao, D. Wang and G.-D. Li, *Nanoscale*, 2014, **6**, 7255.

173 R. Ding, L. Qi and H. Wang, *J. Solid State Electrochem.*, 2012, **16**, 3621–3633.

174 W. Yang, Z. Gao, J. Ma, X. Zhang, J. Wang and J. Liu, *J. Mater. Chem. A*, 2014, **2**, 1448–1457.

175 J. C. Arrebola, A. Caballero, M. Cruz, L. Hernán, J. Morales and E. R. Castellón, *Adv. Funct. Mater.*, 2006, **16**, 1904–1912.

176 H. Y. Xu, H. Wang, Z. Q. Song, Y. W. Wang, H. Yan and M. Yoshimura, *Electrochimica Acta*, 2004, **49**, 349–353.

177 A. K. Mondal, D. Su, S. Chen, X. Xie and G. Wang, *ACS Appl. Mater. Interfaces*, 2014, **6**, 14827–14835.

178 H. Kim, H. Kim, H. Kim, J. Kim, G. Yoon, K. Lim, W.-S. Yoon and K. Kang, *Adv. Funct. Mater.*, 2016, **26**, 5042–5050.

179 M. M. Rahman, A. M. Glushenkov, T. Ramireddy and Y. Chen, *Chem. Commun.*, 2014, **50**, 5057.

180 C. Han, D. Yang, Y. Yang, B. Jiang, Y. He, M. Wang, A.-Y. Song, Y.-B. He, B. Li and Z. Lin, *J. Mater. Chem. A*, 2015, **3**, 13340–13349.

181 Y. Xu, Y. Zhu, Y. Liu and C. Wang, *Adv. Energy Mater.*, 2013, **3**, 128–133.

182 L. Li Zhang, Y. Gu and X. S. Zhao, *J. Mater. Chem. A*, 2013, **1**, 9395–9408.

183 J. R. Miller and A. F. Burke, *Electrochem. Soc. Interface*, 2008, **17**, 53.

184 V. Aravindan, J. Gnanaraj, Y.-S. Lee and S. Madhavi, *Chem. Rev.*, 2014, **114**, 11619–11635.

185 V. Aravindan, M. Ulaganathan and S. Madhavi, *J. Mater. Chem. A*, 2016, **4**, 7538–7548.

186 A. K. Shukla, A. Banerjee, M. K. Ravikumar and A. Jalajakshi, *Electrochimica Acta*, 2012, **84**, 165–173.

187 A. Krause, P. Kossyrev, M. Oljaca, S. Passerini, M. Winter and A. Balducci, *J. Power Sources*, 2011, **196**, 8836–8842.

188 M. Schroeder, M. Winter, S. Passerini and A. Balducci, *J. Power Sources*, 2013, **238**, 388–394.

189 V. Aravindan, J. Sundaramurthy, A. Jain, P. S. Kumar, W. C. Ling, S. Ramakrishna, M. P. Srinivasan and S. Madhavi, *ChemSusChem*, 2014, **7**, 1858–1863.

190 W.-H. Qu, F. Han, A.-H. Lu, C. Xing, M. Qiao and W.-C. Li, *J. Mater. Chem. A*, 2014, **2**, 6549–6557.

191 V. Palomares, P. Serras, I. Villaluenga, K. B. Hueso, J. Carretero-González and T. Rojo, *Energy Environ. Sci.*, 2012, **5**, 5884–5901.

192 R. Alcántara, M. Jaraba, P. Lavela and J. L. Tirado, *Chem. Mater.*, 2002, **14**, 2847–2848.

193 K. Zhou, Z. Hong, C. Xie, H. Dai and Z. Huang, *J. Alloys Compd.*, 2015, **651**, 24–28.

194 J. F. Marco, J. R. Gancedo, M. Gracia, J. L. Gautier, E. Rios and F. J. Berry, *J. Solid State Chem.*, 2000, **153**, 74–81.

195 J.-H. Zhong, A.-L. Wang, G.-R. Li, J.-W. Wang, Y.-N. Ou and Y.-X. Tong, *J. Mater. Chem.*, 2012, **22**, 5656–5665.

196 J. Li, S. Xiong, Y. Liu, Z. Ju and Y. Qian, *ACS Appl. Mater. Interfaces*, 2013, **5**, 981–988.

197 S. Khalid, C. Cao, A. Ahmad, L. Wang, M. Tanveer, I. Aslam, M. Tahir, F. Idrees and Y. Zhu, *RSC Adv.*, 2015, **5**, 33146–33154.

198 J. Su, X.-L. Wu, J.-S. Lee, J. Kim and Y.-G. Guo, *J. Mater. Chem. A*, 2013, **1**, 2508–2514.

199 P. Xiong, L. Zeng, H. Li, C. Zheng and M. Wei, *RSC Adv.*, 2015, **5**, 57127–57132.

200 E. Peled, *J. Electrochem. Soc.*, 1979, **126**, 2047–2051.

201 Y. Gu, H. Wu, Z. Xiong, W. A. Abdulla and X. S. Zhao, *J. Mater. Chem. A*, 2014, **2**, 451–459.

202 L. Xia, L. Yu, D. Hu and G. Z. Chen, *Mater. Chem. Front.*, 2017, **1**, 584–618.

203 S.-W. Kim, H.-W. Lee, P. Muralidharan, D.-H. Seo, W.-S. Yoon, D. K. Kim and K. Kang, *Nano Res.*, 2011, **4**, 505–510.

204 B. E. Conway, W. G. Pell and T.-C. Liu, *J. Power Sources*, 1997, **65**, 53–59.

205 J. Wang, J. Polleux, J. Lim and B. Dunn, *J. Phys. Chem. C*, 2007, **111**, 14925–14931.

206 P. Sennu, H.-J. Choi, S.-G. Baek, V. Aravindan and Y.-S. Lee, *Carbon*, 2016, **98**, 58–66.

207 A. Du Pasquier, I. Plitz, J. Gural, F. Badway and G. G. Amatucci, *J. Power Sources*, 2004, **136**, 160–170.

208 S.-W. Kim, D.-H. Seo, X. Ma, G. Ceder and K. Kang, *Adv. Energy Mater.*, 2012, **2**, 710–721.

209 Z.-S. Wu, G. Zhou, L.-C. Yin, W. Ren, F. Li and H.-M. Cheng, *Nano Energy*, 2012, **1**, 107–131.

210 S. Yang, X. Feng, S. Ivanovici and K. Müllen, *Angew. Chem. Int. Ed.*, 2010, **49**, 8408–8411.

211 P. Nie, Z. Le, G. Chen, D. Liu, X. Liu, H. B. Wu, P. Xu, X. Li, F. Liu, L. Chang, X. Zhang and Y. Lu, *Small*, **0**, 1800635.

212 X. Li, Z. Le, X. Chen, Z. Li, W. Wang, X. Liu, A. Wu, P. Xu and D. Zhang, *Appl. Catal. B Environ.*, 2018, **236**, 501–508.

213 Z. Xiong, L. Li Zhang, J. Ma and X. S. Zhao, *Chem. Commun.*, 2010, **46**, 6099–6101.

214 B. Xu, J. Zhang, Y. Gu, Z. Zhang, W. Al Abdulla, N. A. Kumar and X. S. Zhao, *Electrochimica Acta*, 2016, **212**, 473–480.

215 Z. Lei, L. Lu and X. S. Zhao, *Energy Environ. Sci.*, 2012, **5**, 6391–6399.

216 Y. Fu, C. Peng, D. Zha, J. Zhu, L. Zhang and X. Wang, *Electrochimica Acta*, 2018, **271**, 137–145.

217 S. Al-Rubaye, R. Rajagopalan, S. Xue Dou and Z. Cheng, *J. Mater. Chem. A*, 2017, **5**, 18989–18997.

218 J. Shen, X. Li, N. Li and M. Ye, *Electrochimica Acta*, 2014, **141**, 126–133.

219 J. Xu, M. Wang, N. P. Wickramaratne, M. Jaroniec, S. Dou and L. Dai, *Adv. Mater.*, 2015, **27**, 2042–2048.

220 L. Li, S.-H. Chai, S. Dai and A. Manthiram, *Energy Environ. Sci.*, 2014, **7**, 2630–2636.

221 L. Li, T. A. Pascal, J. G. Connell, F. Y. Fan, S. M. Meckler, L. Ma, Y.-M. Chiang, D. Prendergast and B. A. Helms, *Nat. Commun.*, 2017, **8**, 2277.

222 V. Augustyn, J. Come, M. A. Lowe, J. W. Kim, P.-L. Taberna, S. H. Tolbert, H. D. Abruña, P. Simon and B. Dunn, *Nat. Mater.*, 2013, **12**, 518.

223 S. Dong, L. Wu, J. Wang, P. Nie, H. Dou and X. Zhang, *J. Mater. Chem. A*, 2017, **5**, 5806–5812.

224 M. Zhou, Y. Xu, C. Wang, Q. Li, J. Xiang, L. Liang, M. Wu, H. Zhao and Y. Lei, *Nano Energy*, 2017, **31**, 514–524.

225 G. Longoni, R. L. Pena Cabrera, S. Polizzi, M. D'Arienzo, C. M. Mari, Y. Cui and R. Ruffo, *Nano Lett.*, 2017, **17**, 992–1000.

226 L. Yang, Y.-E. Zhu, J. Sheng, F. Li, B. Tang, Y. Zhang and Z. Zhou, *Small*, 2017, **13**, 1702588.

227 F. Liu, X. Cheng, R. Xu, Y. Wu, Y. Jiang and Y. Yu, *Adv. Funct. Mater.*, 2018, 1800394.

228 H. Liu, M. Jia, Q. Zhu, B. Cao, R. Chen, Y. Wang, F. Wu and B. Xu, *ACS Appl. Mater. Interfaces*, 2016, **8**, 26878–26885.

229 X. Ding, X. Huang, J. Jin, H. Ming, L. Wang and J. Ming, *Electrochimica Acta*, 2018, **260**, 882–889.

230 S. Hariharan, K. Saravanan, V. Ramar and P. Balaya, *Phys. Chem. Chem. Phys.*, 2013, **15**, 2945–2953.

231 C. Yuan, H. B. Wu, Y. Xie and X. W. D. Lou, *Angew. Chem. Int. Ed.*, 2014, **53**, 1488–1504.

232 Y. Fu, Q. Wei, X. Wang, G. Zhang, H. Shu, X. Yang, A. C. Tavares and S. Sun, *Rsc Adv.*, 2016, **6**, 16624–16633.

233 W. Wei, S. Yang, H. Zhou, I. Lieberwirth, X. Feng and K. Müllen, *Adv. Mater.*, 2013, **25**, 2909–2914.

234 B. Gill Choi, S.-J. Chang, Y. Boo Lee, J. Seong Bae, H. Jin Kim and Y. Suk Huh, *Nanoscale*, 2012, **4**, 5924–5930.

235 Y. Xu, Z. Lin, X. Zhong, X. Huang, N. O. Weiss, Y. Huang and X. Duan, *Nat. Commun.*, 2014, **5**, 4554.

236 P. R. Kumar, Y. H. Jung, K. K. Bharathi, C. H. Lim and D. K. Kim, *Electrochimica Acta*, 2014, **146**, 503–510.

237 Y. Xu, C.-Y. Chen, Z. Zhao, Z. Lin, C. Lee, X. Xu, C. Wang, Y. Huang, M. I. Shakir and X. Duan, *Nano Lett.*, 2015, **15**, 4605–4610.

238 Q. Wang, L. Jiao, H. Du, Y. Wang and H. Yuan, *J. Power Sources*, 2014, **245**, 101–106.

239 D. Yang, Q. Zhao, L. Huang, B. Xu, A. Kumar Nanjundan and X. Song Zhao, *J. Mater. Chem. A*, 2018, **6**, 14146-14154.

240 W. Liu, C. Lu, K. Liang and B. K. Tay, *Part. Part. Syst. Charact.*, 2014, **31**, 1151–1157.

241 Y. Qin, Q. Li, J. Xu, X. Wang, G. Zhao, C. Liu, X. Yan, Y. Long, S. Yan and S. Li, *Electrochimica Acta*, 2017, **224**, 90–95.

242 S. Laruelle, S. Grugeon, P. Poizot, M. Dolle, L. Dupont and J. M. Tarascon, *J. Electrochem. Soc.*, 2002, **149**, A627–A634.

243 B. Xu, X. Guan, L. Ying Zhang, X. Liu, Z. Jiao, X. Liu, X. Hu and X. S. Zhao, *J. Mater. Chem. A*, 2018, **6**, 4048–4054.

244 S. Li, J. Qiu, C. Lai, M. Ling, H. Zhao and S. Zhang, *Nano Energy*, 2015, **12**, 224–230.

245 B. Chi, J. Li, Y. Han and Y. Chen, *Int. J. Hydrog. Energy*, 2004, **29**, 605–610.

246 S. Ayyappan, G. Gnanaprakash, G. Panneerselvam, M. P. Antony and J. Philip, *J. Phys. Chem. C*, 2008, **112**, 18376–18383.